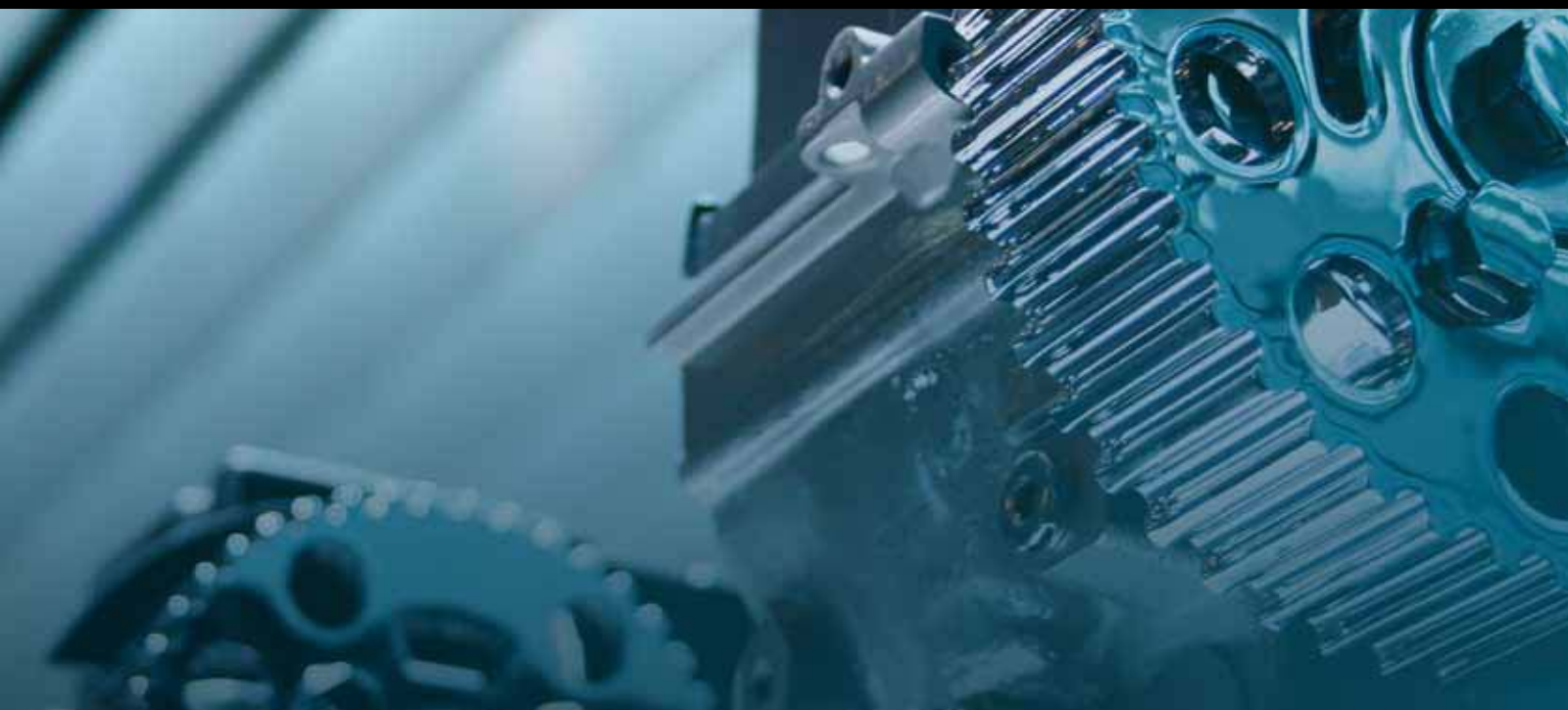# Wear-Related Phenomena in Advanced Materials

Guest Editors: Alexander Tsouknidas, Luca Settineri, Pedro Arrazola, and Nikolaos Michailidis

# Wear-Related Phenomena in Advanced Materials

# Wear-Related Phenomena in Advanced Materials

Guest Editors: Alexander Tsouknidas, Luca Settineri, Pedro Arrazola, and Nikolaos Michailidis

# Editorial Board

# Contents

*Editorial*

# Wear-Related Phenomena in Advanced Materials

## Alexander Tsouknidas,[1] Luca Settineri,[2] Pedro Arrazola,[3] and Nikolaos Michailidis[4]

[1] *Laboratory for Machine Tools and Manufacturing Engineering, Mechanical Engineering Department,*
   *Aristotle University of Thessaloniki, 54124 Thessaloniki, Greece*
[2] *Department of Production Systems and Business Economics, Polytechnic University of Turin, 10129 Torino, Italy*
[3] *Mechanical and Manufacturing Department, Mondragon University, 20500 Arrasate-Mondragón, Spain*
[4] *Physical Metallurgy Laboratory, Mechanical Engineering Department, Aristotle University of Thessaloniki, P.O. BOX 490,*
   *54124 Thessaloniki, Greece*

Correspondence should be addressed to Nikolaos Michailidis, nmichail@eng.auth.gr

Received 19 December 2011; Accepted 19 December 2011

## 1. Aims and Scope of the Issue

The title of this editorial reflects an effort in creating a unique research forum, to harbor fundamental as well as review articles, meeting the forefront of this scientific field. The Guest Editors sought to attract articles on friction, wear, surface properties, and the development of sufficient procedures, to arrest wear progression as well as to indicate mechanisms to prolong the effectiveness of the implicated materials.

In these terms it was exciting and rewarding to embrace related papers of scientists from around the world. The concept of wear-related phenomena in advanced materials, along with a short introduction on the subjects, addressed by the accepted papers, will be presented in the following paragraphs.

## 2. Introduction

Wear has, by its very nature, always dominated the interest of engineers and physicists, as it represents a material property of enormous practical importance. Even though it is a multidisciplinary phenomenon based on simultaneously occurring mechanical, physical, and chemical processes, recent advances in sophisticated material design and development and characterization techniques have sustained methodologies to comprehend and predict wear progression. The capacity to systematically and effectively describe wear development is a perspective of great importance to engineers who use materials and mechanical components or are directly involved with their manufacturing processes.

## 3. Wear in Advanced Materials

Milling is a characteristic manufacturing process in which wear exerts a dominating effect on both product quality and cost. There exists a consensus throughout the literature that high-performance cutting of difficult-to-machine materials strongly depends on the engagement parameters as well as on the tool and workpiece materials, and thus analytical-experimental optimization procedures may lead to drastic enhancement of the tool life, as discussed in the paper entitled "*Characterization of tool wear in high-speed milling of hardened powder metallurgical steels.*" This is particularly important when processing advanced materials like Ti- or Ni-based alloys. Over the past years, the related manufacturing procedures have arisen from their period of infancy and gained tremendous importance in several industrial sectors, that is, aerospace. It has been sustained that novel heuristic optimization procedures can be successfully applied during the integration of milling strategies, for such materials, providing high removal rates while maintaining acceptable production costs, as evidenced in the paper entitled "*Integrated approach for a knowledge-based process layout for simultaneous 5-axis milling of advanced materials.*"

Alternative methods, like additive manufacturing, have been recently introduced for the production of functionally-graded, high-end materials. Even though this eases the production of complex geometries, these technologies produce components prone to several degeneration scenarios and thus, it is pivotal to consider a variety of production and application-based parameters, as shown in the paper

entitled "*Friction induced wear of rapid prototyping generated materials: A review.*"

Antifriction-based materials and components are predominantly developed, based on application-specific requirements. Powder metallurgy is a key enabling technique in this direction, facilitating, among others, the production of self-lubricating components (i.e., bearings). Recent investigations on iron-based alloys indicated a strong enslavement of the mechanical and tribotechnical properties of the final product to the production parameters, which must therefore be carefully considered, as proven in the papers entitled "*Development of new PM iron base materials for self-lubricating bearings.*" and "*Model of fracture, friction, and wear phenomena of porous iron.*" Aluminum-based $TiB_2$-reinforced composites are widely considered as an alternative to ferrous antifriction components. Late studies revealed that the wear behavior of these composites is comparable to the one of gray cast iron parts, as exhibiled in the paper entitled "*Wear behavior and its correlation with mechanical properties of $TiB_2$ reinforced aluminium-based composites.*" The high cost of aluminum composites can be decreased through recovery procedures of dross, produced in large quantities "*A characterization method for Al recovery from dross based on compression at elevated temperatures.*" Related procedures have been optimized, and the purity of the recovered material is considered as acceptable for the production of high-added-value products.

## Epilogue

Our sincere hope and wish is that "Advances in Tribology" will continue to address the multidisciplinary phenomena reflected in the wear development of advanced materials, and we commit ourselves to support this effort in our best capacity.

<div align="right">

*Alexander Tsouknidas*
*Luca Settineri*
*Pedro Arrazola*
*Nikolaos Michailidis*

</div>

*Research Article*

# Development of New PM Iron-Based Materials for Self-Lubricating Bearings

## Cristina Teisanu and Stefan Gheorghe

*Faculty of Mechanics, University of Craiova, 107 Calea Bucuresti, 200512 Craiova, Romania*

Correspondence should be addressed to Cristina Teisanu, cteisanu@yahoo.com

Using PM technologies, new antifriction materials based on iron powder with different addition elements were developed in order to obtain self-lubricated bearings with improved tribological features. The elemental powder mixtures were blended for 2 hours in a 3D homogenization device, were compacted at a pressure of 500 MPa, and then sintered in dry hydrogen atmosphere at different temperatures for different maintaining times. The effect of technological parameters on physical properties (density and dimensional changes) was presented in this study. The mechanical and tribological properties (tensile strength, hardness, impact energy, friction coefficient, and wear rate) related to addition elements were evaluated. The tribological behaviour of the selected iron-based alloys was analysed by pin on disc tests without lubrication. Also, the wear surface scars and the microstructure of the wear surfaces were investigated.

## 1. Introduction

Self-lubricating bearings represent the oldest industrial application of the porous materials obtained by PM technique as metallic filters and sparking plugs cannot be produced by other technology. In the recent years iron-based sintered bearings production was considerably increased at the expense of the copper-based ones, due to the low cost and availability of the iron powders as well as their higher strength. The mechanical properties of the parts are strongly related to the composition of the material. For tribological applications, the properties of the surface are linked to the different metallic and intermetallic phases formed in the material.

Controlled inhomogeneity of the structure by powder metallurgy processes makes it possible to obtain materials with special properties, which cannot be manufactured by conventional technologies. Many sintered parts reach sufficiently high-strength properties, for example, similar to cast iron, already at a porosity of 20–15%. The great advantage of the porous materials over the compacted ones obtained by conventional technologies is their porosity, which acts like its own oil reservoir. Self-lubricating bearings accomplish superior performance when the porosity level is high, so sufficient oil is accumulated in the pores during inactivity periods and it leaks when the shaft begins rotating in it. Also, the material density plays an important role for self-lubricating bearings for exhibiting good load-bearing capacity. Therefore, it is essential to know the actual loading conditions of the part and modify the alloying and the treatment conditions of the material on the basis of these conditions.

Sintered iron-based antifriction materials were not developed until the last decades because of their poor corrosion resistance and antifriction properties. Considering the low cost and availability of iron, additions such as copper, graphite, manganese, lead, phosphorous, boron, and tin to iron have been attempted, but improvement in one property was offset by a decrease in other properties [1–4]. In order to enhance antifriction and mechanical properties, the present paper focuses on the development of Fe-Cu-Sn-Pb-MoS$_2$ antifriction alloys.

As the quality of the material powders and the manufacturing processes were improved, powder metallurgy parts had in many cases taken the place of cast and forged products. It is very important, in order to avoid subsequent operations such as sizing and machining, to improve the final dimensional tolerances obtained after sintering. There are

Table 1: Composition of the powder mixtures.

| Alloy | Iron wt% | Copper wt% | Tin wt% | Lead wt% | $MoS_2$ wt% |
|-------|----------|------------|---------|----------|-------------|
| 1 | Rest | 5 | 1 | 7.5 | 1 |
| 2 | Rest | 5 | 1.5 | 5 | 1 |
| 3 | Rest | 5 | 2.5 | 2.5 | 1 |

Table 2: Experimental conditions.

| Sintering conditions | Sintering temperature [°C] | 800–900 |
|----------------------|-----------------------------|---------|
| | Holding time [min.] | 20, 35, 50 |
| | Atmosphere | Dry hydrogen |
| Sintered density [g/cm³] | | 6.5–6.9 |

Table 3: Density values of the sintered mixtures.

| Sintering temperature | Dwell time | Density | | |
|-----------------------|------------|---------|---------|---------|
| | | Alloy 1 | Alloy 2 | Alloy 3 |
| 800 | 20 | 6.81 | 6.68 | 6.59 |
| | 35 | 6.87 | 6.72 | 6.54 |
| | 50 | 6.85 | 6.8 | 6.71 |
| 850 | 20 | 6.79 | 6.58 | 6.56 |
| | 35 | 6.84 | 6.61 | 6.55 |
| | 50 | 6.83 | 6.67 | 6.57 |
| 900 | 20 | 6.72 | 6.54 | 6.54 |
| | 35 | 6.76 | 6.53 | 6.52 |
| | 50 | 6.73 | 6.54 | 6.53 |

many factors that cause dimensional changes, and their combined effect makes it more difficult to forecast and control these changes. In the present paper, the experimental results of influence the different parameters on the dimensional changes of the sintered iron based alloys was reported.

Also, the density of the sintered parts was investigated and, thus, the effect of the sintering temperature and time on the density of the iron-based materials for self-lubricating bearings was studied.

These influences of the sintering parameters on the density and dimensional changes are presented as 3D surface plots using Statistica software.

## 2. Materials and Experimental Procedure

As experimental materials, iron powder produced by DUCTIL S.A. BUZAU (DP 200-HD), electrolytic copper powder, tin powder, lead powder, and molybdenum disulphide powder were used. Because of its lamellar structure, $MoS_2$ is one of the most popular and usable solid lubricants. $MoS_2$ is used to reduce the interparticle friction as well as friction between powder particles and die wall during conventional cold die compaction. Lead exhibits excellent self lubricating property and plays a role of solid lubricant to prevent seizure. In addition, since Pb forms a soft dispersion phase, it has conformability and allows solid matter to be embedded therein. Tin is a key player in antifriction alloys because it can influence both corrosion resistance and fatigue strength

and friction and wear properties of these materials can also be improved.

Elemental powders were weighed to the selected proportions and mixed for 2 hours in 3D homogenization device. Then, test pieces were cold compacted at 500 MPa into a rigid die by applying pressure in a single axial direction through a rigid punch or piston, and cylindrical specimens with 10 mm diameter and 7 mm height were obtained and used for metallographic examination and measurement of green and sintered density, porosity, and dimensional change after sintering.

Green samples were placed in a tubular furnace having a uniform heating zone and sintered at 800, 850, and 900°C for 20, 35, and 50 minutes. The sintering atmosphere was dry hydrogen with a flow rate of 1 L/min. Samples were then furnace-cooled by switching off the power and maintaining the same flow rate of the hydrogen gas.

Reference densities for the selected compositions were calculated by the rule of mixtures, and sintered densities were evaluated gravimetrically using the Archimedes principle. Volumetric dimensional change of the sintered compacts was calculated, and the total porosity of the specimens was evaluated from the difference between the reference density and the measured density.

Experimental conditions and the composition of the powder mixtures are presented in Tables 1 and 2, and densities of the sintered compacts are shown in Table 3.

Specially shaped specimens were produced by PM technology for testing the tensile strength of the PM parts in conformity with operating standardization.

Hardness test for PM materials was carried out using the Vickers method with an indentation load of 50 N.

Impact energy was determined by the Charpy test according to SR EN 10045-1-93 using $5 \times 10 \times 55$ mm specimens without notches.

Tribological behaviour of the sintered samples was analysed under dry friction conditions by pin-on-disc test using a testing device for friction coefficient and wear rate measurements (Figure 1) at a sliding speed of 0.75 m/s and a specific load of 3.72 MPa giving $p \times v$ value of 2.8 MPa m/s. Load-carrying ability is an important tribological behaviour of a dry sliding couple. The $pv$ factor or $p \times v$ value characterizes the mechanical input in a sliding bearing as severity of design or the maximum mechanical input that the tribomaterials can support [5]. Cylindrical specimens of 10.5 mm diameter and 7 mm height were used for wear tests. The mating part was made from 1C45 (SR EN 10083-1,2) with 235 HB.

The friction coefficient was calculated using relation (1), along the sliding distance of 1360 m:

$$\mu = \frac{F_f}{F}, \tag{1}$$

$F_f$ is the friction force and $F$ is the resulting force acting on the lever.

The wear rate was performed for materials sintered at 900°C for 50 minutes because of their better values of the mechanical and physical characteristics compared with those sintered at 850°C and 800°C. The wear rate was evaluated at $p \times v = 2.8$ MPa m/s and calculated in terms of the worn
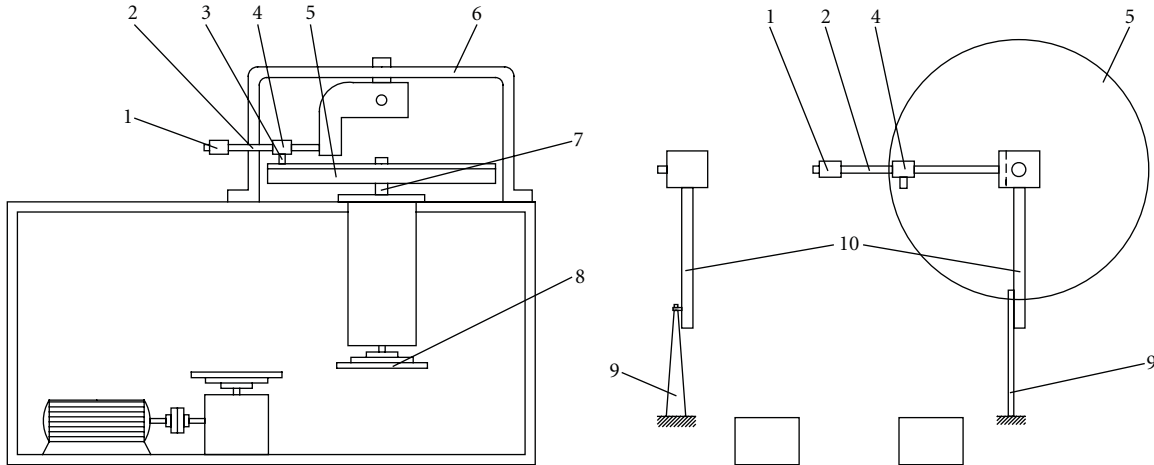
FIGURE 1: Testing device for friction coefficient and wear rate measurements: 1: weight; 2: ruler; 3: pin sample; 4: pin sample blocking part; 5: mating disc; 6: rigid frame; 7: driving shaft; 8: trapezoidal transmission; 9: elastic lamella; 10: lever.



(a)



(b)



(c)
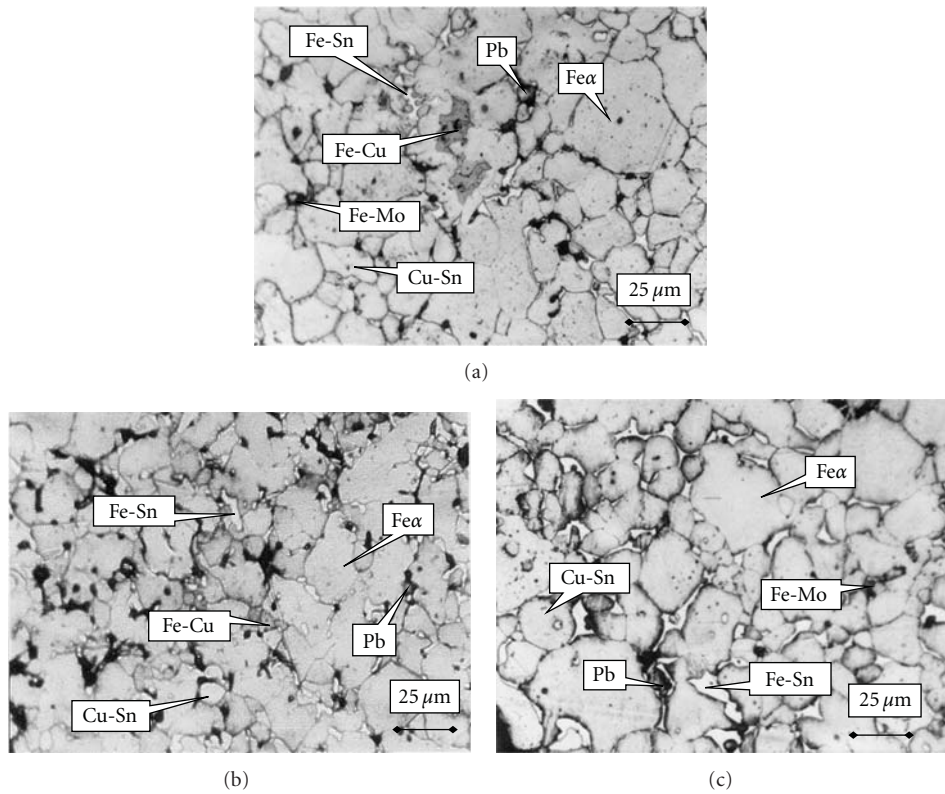
FIGURE 2: Microstructure of the alloys 1 (a), 2 (b), and 3 (c) sintered at 900°C for 50 minutes.

layer thickness of the sample per sliding distance and in terms of the worn volume of the tested sample per sliding distance using reference density of each compact. Linear wear rate and volumetric wear rate were determined as follows: (2) $\Delta h$ is the thickness of the worn layer (mm),

$$I_g = \frac{\Delta V}{L_{\text{sliding}}} \ [\text{mm}^3/\text{m}], \tag{2}$$

$\Delta V$ is the volume of the worn material (mm$^3$) and $L_{\text{sliding}}$ the sliding distance (m).

The wear surface characteristics were emphasized by SEM images.

## 3. Results and Discussions

*3.1. Microstructure and Physical Properties.* Representative microstructures of the selected alloys are shown in Figure 2, and microscopic investigations of the specimens porosity are presented in Figure 3.

(a)



(b)



(c)

FIGURE 3: Porosity of the alloys 1 (a), 2 (b), and 3 (c) sintered at 900°C for 50 minutes.

These microstructures emphasize a relatively uniform distribution of the phases in the ferrite matrix, with distinctive boundaries. Few globular Pb grains and Cu-Sn grains can be distinguished in all compositions, as well as elongated Fe-Sn intermetallic compounds scattered in the Fe$\alpha$ matrix around ferrite grains. This arrangement of the grains is typical to the final stage of the liquid-phase sintering when liquid occupies the space between the grains. Also, so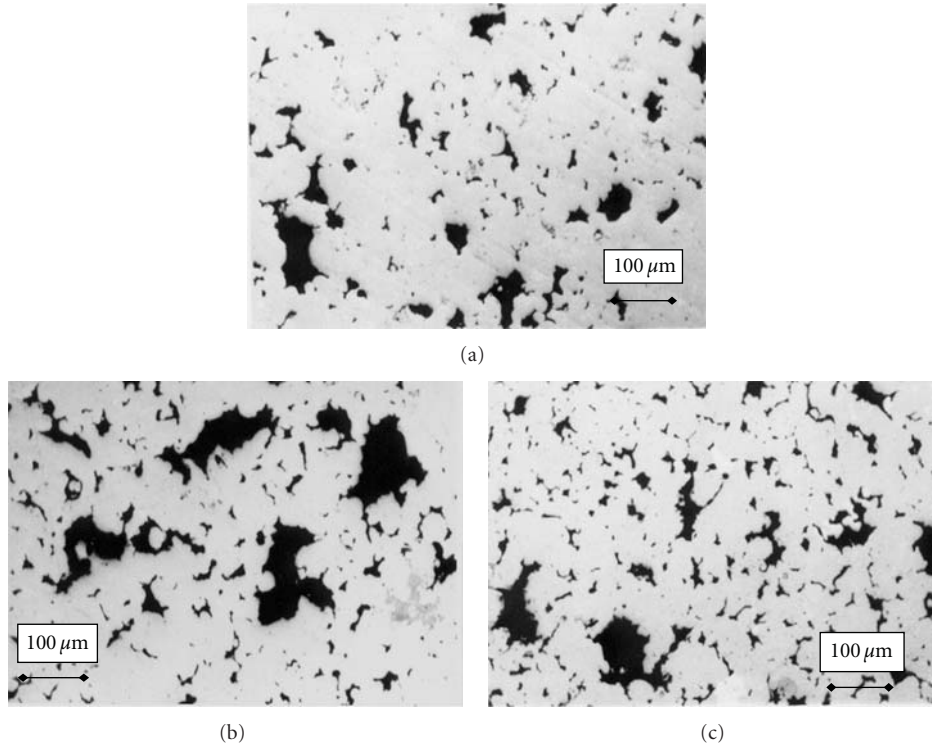me Fe-Mo grains can be seen in compositions with 1% Sn and 2.5% Sn and some Fe-Cu grains in alloys 1 and 2. There are few small pores in samples with 1% Sn and 2.5% Sn, but the sample containing 1.5% Sn exhibits a higher level of porosity with pores of irregular shape placed mainly at the grain boundaries.

Optical micrographs of the polished and unetched surfaces of the sintered compacts made from alloys 1, 2, and 3 show different levels of porosity. There are few large pores in each sample with irregular shapes and sharp edges, except for some with rounded shape (Figure 3(a)), and with a nonuniform distribution into the metallic matrix in all samples. Small pores can be observed in larger quantities with a relatively more homogeneous distribution as the tin content increases, with acicular and spot-like shapes.

Certain physical features of the sintered materials have a major importance because of their influence on some mechanical properties (tensile strength, compression strength, toughness, and hardness), antifriction, and self-lubricating properties.

The density of the sintered samples made from the selected alloys (1, 2, and 3) as a function of sintering time and temperature was characterized.

The 3D graphic dependences of the density versus sintering temperature for the selected materials compacted at 500 MPa and maintained in the heating zone for 20, 35, and 50 minutes are presented in Figures 4, 5, and 6.

From the analysis of the presented charts it can be observed a decrease of the sintered density as the temperature is getting higher for all three alloys. For samples containing 1% Sn and sintered at all temperatures the density shows an increase as the sintering time reaches 35 minutes and then it decreases as the sintering time continues up to 50 minutes. A dissimilar trend is observed for samples with 2.5% Sn at all sintering temperatures with respect to maintaining time. For the alloy with 1.5% Sn sintered density presents an ascending variation when heating at 800°C and 850°C for 20, 35, and 50 minutes and a descending variation when sintering at 900°C for all three maintaining times. The smallest values of the sintered density are recorded for 20 minute sintering time for alloy no. 1 and for 35 minutes for alloys no. 2 and 3.

This behaviour of the sintered density is attributed to the compact swelling during liquid-phase sintering. The formation of a copper-tin alloy at the neck of the iron-tin intermetallic compound generates the initial decrease of the densification by restricting diffusion of low melting phases into the network to fill the pores. Since the diffusion coefficient of copper in tin is higher than that of iron in tin at a temperature of about 850°C, the formation of iron-tin intermetallics contributes to the increase in intercommunicating porosity, and thus a less densification. Increasing of the density occurs when soft phases diffuse into the pores. Pore filling by liquid preferentially starts at a localized region in the compact and spreads during liquid-phase sintering. Small pores fill first
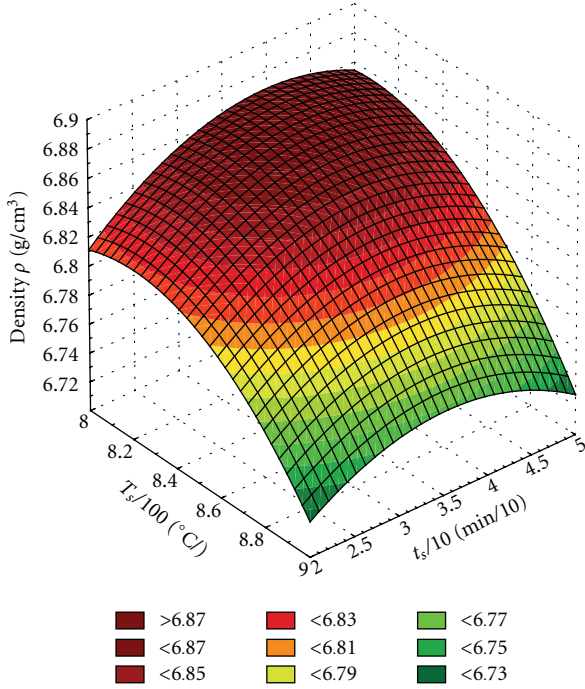
FIGURE 4: The dependence of the density: $\rho = f(T_s, t_s)$ is the alloy no. 1.
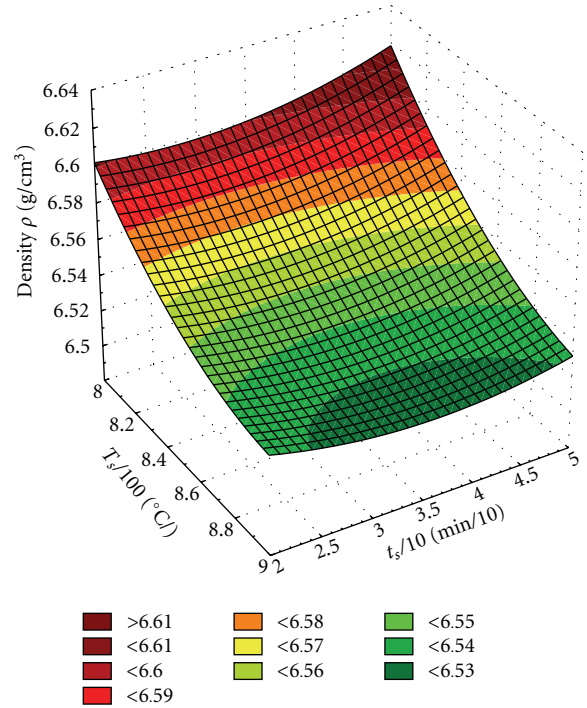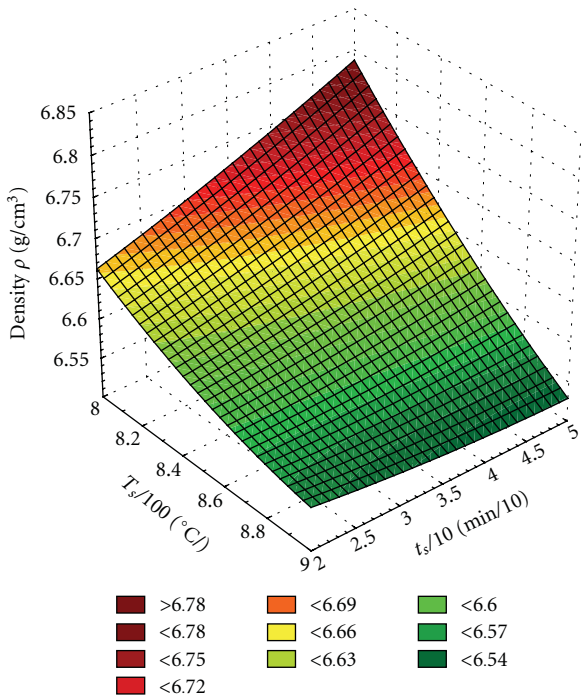


FIGURE 5: The dependence of the density: $\rho = f(T_s, t_s)$ is the alloy no. 2.

since they have the highest capillary attraction for the wetting liquid. High-green-density regions correspond to smaller pores, so pore filling naturally favours the high-green-density regions [6].



FIGURE 6: The dependence of the density: $\rho = f(T_s, t_s)$ is the alloy no. 3.

In Figures 7, 8, and 9 the dependence of the dimensional changes on sintering parameters (temperature and time) of the iron-based sintered samples is shown.

The large expansion of the dimensions observed for all alloys sintered at 900°C is possible due to liquid penetration of the grain boundaries which causes grain separation and swelling on liquid formation. This penetration action pushes more solid particles apart, increasing the distance between particle centres and consequently leading to the growth of the compacts [7]. This behaviour is attributed probably to the formation of Cu-Sn, Fe-Cu, and Fe-Sn compounds in larger amounts at higher temperatures as the tin content increases. Liquid tin has substantial solubility in the solid iron; thus compact swelling due to pore formation at prior particle sites occurs.

Decreasing the dimensional changes is attributed to the formation of the Fe-Sn phase at higher temperatures, which has a lower coefficient of thermal expansion than iron. Another cause of the dimensional growth might be attributed to the trapped hydrogen in the pores as the sintering process was performed in hydrogen atmosphere.

*3.2. Mechanical Properties.* Tensile strength for shaped specimens sintered in the specified conditions is presented in Figure 10 as a function of the tin content.

The tensile strength has the higher values for all compositions sintered at 900°C and decreases with the decrease of the Sn content. The same tendency is observed for all sintering temperatures. This behaviour may be due possibly to the formation at higher temperatures of some strengthening phases like Fe-Cu, Fe-Sn, Fe-Mo, and Cu-Sn and to the gradual
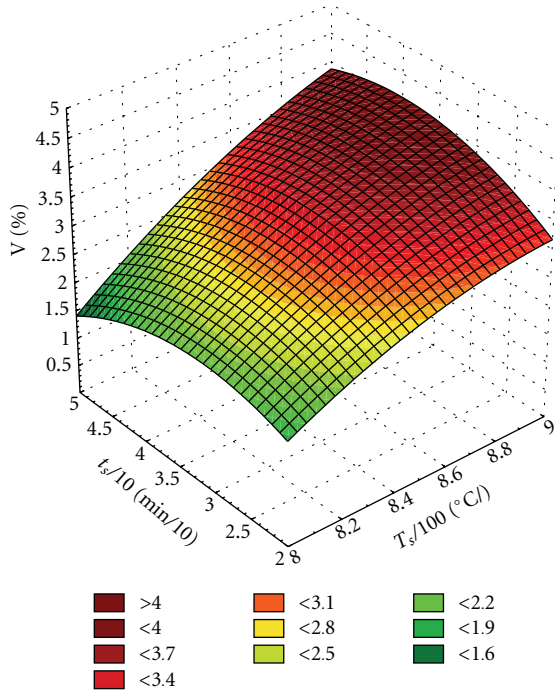
FIGURE 7: The effect of sintering parameters on dimensional changes for alloy no. 1.
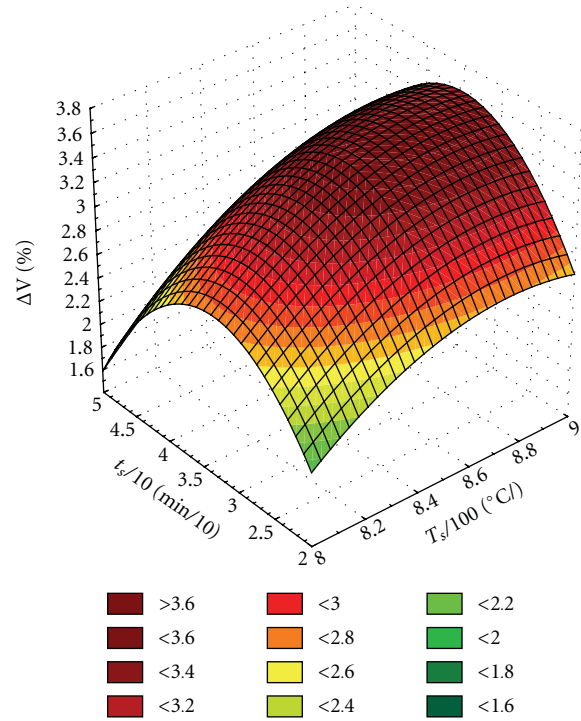


FIGURE 9: The effect of sintering parameters on dimensional changes for alloy no. 3.
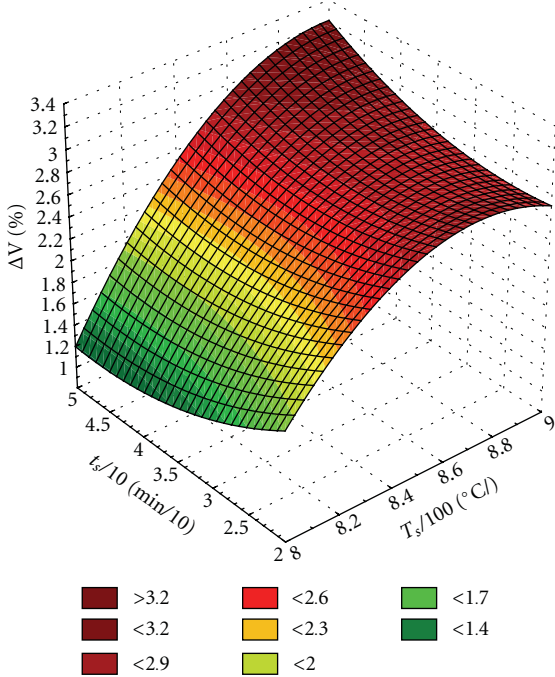


FIGURE 8: The effect of sintering parameters on dimensional changes for alloy no. 2.



FIGURE 10: Influence of the Sn content on tensile strength.

increase of the solid skeleton solubility in the transient liquid phase as the temperature is getting higher.

The influence of the chemical composition on the hardness and impact energy is depicted in Figures 11–13.

For all samples sintered at 900°C the highest values of the hardness were obtained. All the selected compositions have almost the same hardness behaviour at all three sintering temperatures, except for the one containing 1.5% Sn and sintered at 800°C which presents an increased value of the hardness. This can be explained by the presence of some strengthening phases such as Fe-Sn, Fe-Cu, and Cu-Sn which form due to longer time available for diffusion processes. The highest value of the hardness (139 VH$_5$) was exhibited for the sample with 2.5% Sn sintered at 900°C.

The aim of the Charpy test is to establish the notch toughness of the material, defined as the work (impact energy) used to fracture the specimen under test conditions. The Charpy impact tests on unnotched samples were conducted with an instrumented pendulum at room temperature
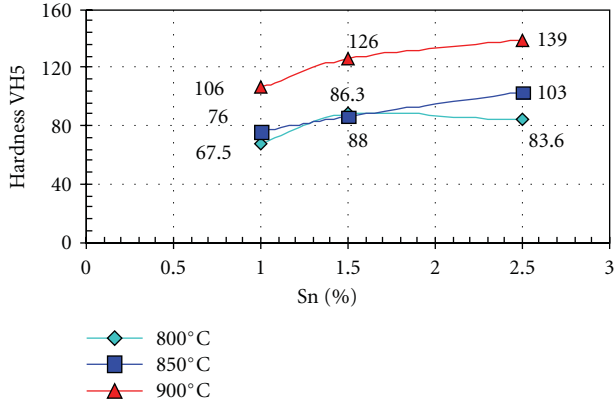
FIGURE 11: The effect of the Sn content on the Vickers hardness.
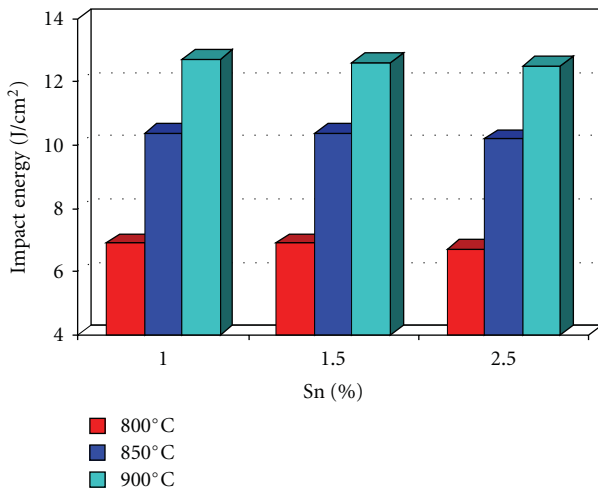


FIGURE 12: The effect of the Sn content on the impact energy.
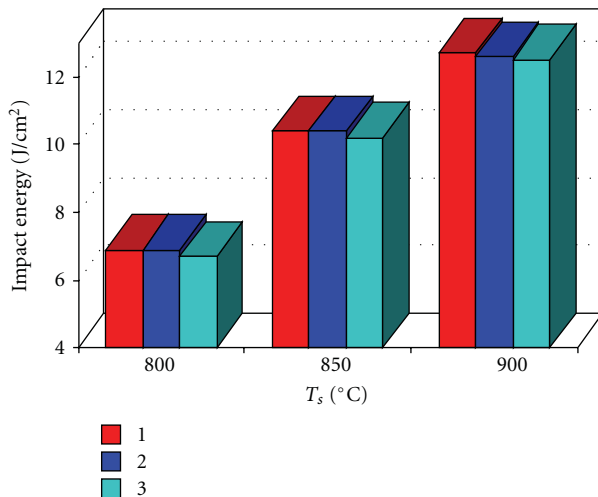


FIGURE 13: The effect of the sintering temperature on the impact energy.

TABLE 4: The Charpy test results.

| Alloy | Sintering temperature [°C] | | | | | |
| | 800 | | 850 | | 900 | |
| | $E$ [J] | KC [J/cm$^2$] | $E$ [J] | KC [J/cm$^2$] | $E$ [J] | KC [J/cm$^2$] |
|---|---|---|---|---|---|---|
| 1 | 4.6 | 6.9 | 6.9 | 10.4 | 8.4 | 12.7 |
| 2 | 4.6 | 6.9 | 7 | 10.4 | 8.6 | 12.6 |
| 3 | 4.6 | 6.7 | 7 | 10.2 | 8.7 | 12.5 |
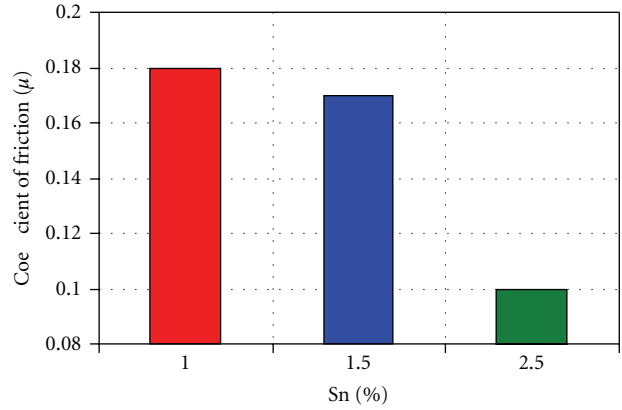


FIGURE 14: The influence of the tin content on the coefficient of friction at a $p \times v$ value of 2.8 MPa m/s.

having an available energy $E_0$ of 100 J and an impact hammer speed of 5 m/s.

Table 4 shows the impact energy ($E$) and toughness strength (KC) values for all alloys sintered at 800°C, 850°C, and 900°C for 50 minutes. The influence of the chemical composition on impact energy is presented in Figure 12, and the influence of the sintering temperature on the impact energy is observed in Figure 13.

The lowest values of the impact energy were observed for samples containing 2.5% Sn at all three temperatures, and the higher values were observed for samples with 1% Sn. Impact energy is about two times as high after sintering at 900°C compared to 800°C, which underlines the effect of microstructural homogeneity, although the change of pore shape and size and more uniform distribution of the pores may also contribute to this behaviour. Higher values of the impact energy may be attributed to the formation of soft phases such as Pb-Sn or sulphides of Cu-Sn and Fe-Sn in larger quantities, which diffuse into the closed pores, thus, resulting in a microstructure with more plastic regions. Consequently, the higher amount of energy required to fracture a specimen means a tough ductile material.

*3.3. Tribological Characteristics.* The effect of the tin content on the coefficient of friction for samples sintered 900°C for 50 minutes and tested at $p \times v$ value of 2.8 MPa m/s is shown in Figure 14 and its values are presented in Table 5.

Specimens containing 1% Sn exhibit higher values of the coefficient of friction, and smaller values are observed for the specimens with 2.5% Sn. This may be possibly due to the presence of some soft phases like Cu-Pb and Fe-Cu-S which have low share strength in the substrate and

TABLE 5: Friction coefficient values and linear and gravimetric wear rates of the selected materials.

| Alloy | $F$ [N] | $F_f$ [N] | $\mu$ | $L_{slide}$ [m] | $\Delta h$ [mm] | $I_h \times 10^{-5}$ [mm/m] | $\Delta V \times 10^3$ [mm³] | $I_g \times 10^{-2}$ [mm³/m] |
|---|---|---|---|---|---|---|---|---|
| 1 | 325 | 58.7 | 0.18 | 1360 | 0.55 | 40.4 | 0.154 | 11.3 |
| 2 | 325 | 58.1 | 0.17 | 1360 | 0.34 | 25 | 0.148 | 10.8 |
| 3 | 325 | 32.5 | 0.1 | 1360 | 0.24 | 17.6 | 0.135 | 9.8 |
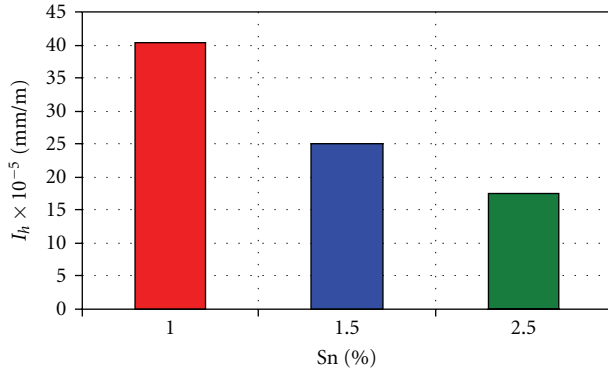


FIGURE 15: The influence of the tin content on the linear wear rate.
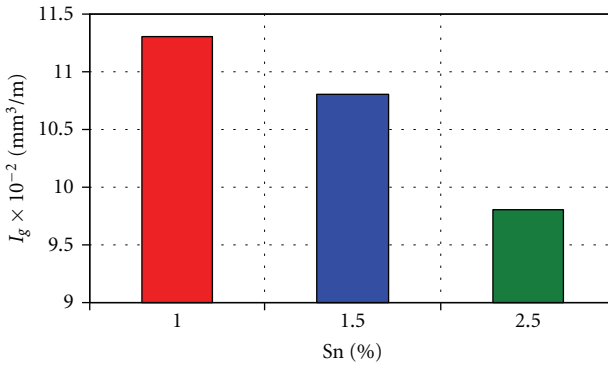


FIGURE 16: The influence of the tin content on the gravimetric wear rate.

are exposed to sliding due to high load [8]. Generally, the variation of the coefficient of friction can be explained on the basis of the hardness variation (Figure 11). The coefficient of friction increases with the decrease of the hardness and the increase of the share strength of the material, which means a direct proportionality with the hardness and an indirect proportionality with the share strength. Besides its great ability to reduce friction between powder particles and between powder particles and die wall during conventional cold die compaction, $MoS_2$ is used to reduce friction between metallic surfaces under certain conditions of application. Another suitable approach for the application of $MoS_2$ is its incorporation in a metallic matrix in order to produce self-lubricating material [9]. Therefore, the presence of the solid lubricant $MoS_2$ contributes to the reduction of the coefficient of friction. The solid lubricant particles get on the containing surface during the sliding process and reduce the friction [10].

The linear wear rate was determined by measuring the final height of the samples at the end of the test and extracting

it from the initial height, giving the thickness of the worn layer ($\Delta h$). Similarly, the gravimetric wear rate was found by weighing the specimens after performing the test and calculating their volume using reference densities. The final results represent the average values of three determinations.

Linear and gravimetric wear rates values are presented in Table 5. Figure 15 shows linear wear rate for samples with different Sn additions sintered in the specified conditions, and Figure 16 shows the gravimetric wear rate as a function of tin content.

From Figures 15 and 16 it can be observed that the wear rates (linear and gravimetric) of the material containing 2.5% Sn and tested at $p \times v = 2.8$ MPa m/s exhibited the lowest value of the wear rate. As for friction coefficient, wear rate exhibits an inverse relationship with hardness and a direct relationship with share strength. In spite of the greater amount of lead in samples with 1% Sn and 1.5% Sn, which diffuses to the surface and acts like a solid lubricant, higher mass loss was quantified during the wear test indicating a low wear resistance. This behaviour may be possible due to the higher normal load ($p = 3.2$ MPa) which increases the adhesive component when the substrate is exposed, and the transfer of the soft phases (Pb, Sn-Pb, or sulphides) from the sample surface to the disc is enhanced by increasing the share stress at the surface.

Figure 17 shows representative wear surfaces of the samples sintered at 900°C for 50 minutes and tested at $p \times v = 2.8$ MPa m/s. Also, the marginal zones of the samples highlighting the material behaviour during wear process can be observed in Figure 18. In order to study the surface damage worn specimens were examined using scanning electron microscopy (SEM).

The worn surfaces present smeared pores and deeper wear tracks indicating that wear occurred due to combined action of adhesive and abrasive mechanisms with transfer and microcutting of the tested material in all compositions.

The worn surface of the material containing 1% Sn presents deep scars, which are formed along the sliding direction due to the strong adhesion between roughs in contact (Figure 17(a)). The surface layers are modified and the oxide films are damaged by plastic deformation, subsequently new layers being in contact.

Also, during the wear process the rolling or flanging of the marginal zone as well as the exfoliation of the material can be observed (Figure 18(a)). This behaviour is typical to soft and ductile materials and may be explained by the great amount of lead in the material composition.

The wear surface of the sample with 1.5% Sn shows less deep scars, but the wear surface is rougher and the detached wear particles from the sample surface can be observed (Figure 17(b)).
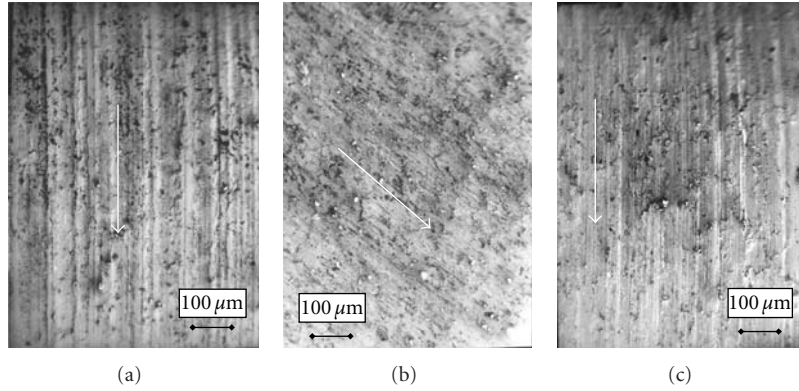
FIGURE 17: SEM micrographs of the wear scars of the tested materials sintered at 900°C for 50 minutes: (a) 1% Sn; (b) 1.5% Sn; (c) 2.5% Sn.
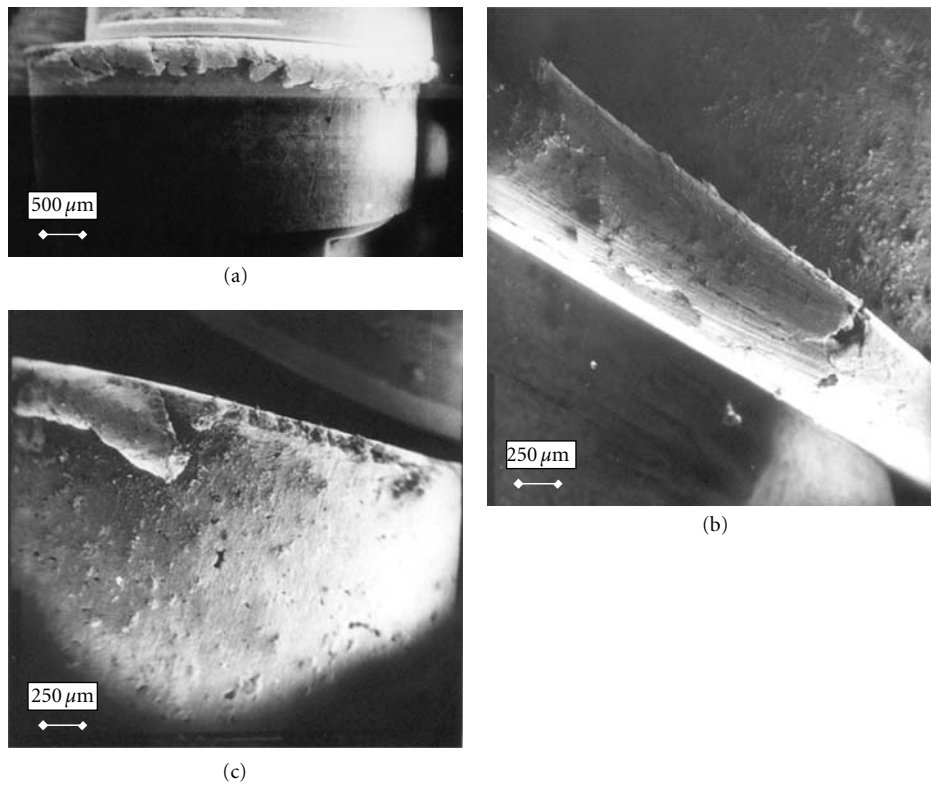


FIGURE 18: SEM micrographs of the marginal zone of the materials sintered at 900°C for 50 minutes: (a) 1% Sn; (b) 1.5% Sn; (c) 2.5% Sn.

Similarly, the rolling and the exfoliation of the marginal material of the sample occurred, but in a smaller rate due to a lesser amount of lead (Figure 18(b)).

The ductile character of the sintered material observed on microscopic scale by "cone-cup" configuration of the inter-particle bridges can be also highlighted on macroscopic scale by plastic deformation processes which are slowly developed during the wear process.

The alloy containing 2.5% Sn has the higher value of the hardness and the friction coefficient and wear rates have acceptable values. The wear surface of this material is less coarse with finer scars and a smaller number of particles detached from the sample surface due to the failure of the welding bridges between the microcontact zones (Figure 17(c)). A lesser amount of marginal material is rolled and exfoliated (Figure 18(c)).

Surface roughness measurements were carried out on the worn surfaces using a surface profilometer.

Figure 19 shows the 2D surface profile of the samples with compositions 1, 2, and 3 after the wear test. $P_t$ is the maximum peak-to-valley height of the 2D surface profile; $R_a$ is the arithmetic mean surface roughness and is the most commonly used parameter to monitor a production process; $R_z$ is the surface roughness depth and, as a rule, is used for all types of surfaces; $R_p$ is the maximum profile peak height and is useful in predicting bearing characteristics of a surface.

Length = 4 mm, $P_t$ = 24 $\mu$m, scale = 40 $\mu$m

(a) $R_p$ = 6.58 $\mu$m; $R_a$ = 2.09 $\mu$m; $R_z$ = 12.1 $\mu$m

Length = 4 mm, $P_t$ = 21.9 $\mu$m, scale = 40 $\mu$m

(b) $R_p$ = 5.44 $\mu$m; $R_a$ = 1.89 $\mu$m; $R_z$ = 11.6 $\mu$m

Length = 4 mm, $P_t$ = 15.8 $\mu$m, scale = 30 $\mu$m

(c) $R_p$ = 3.62 $\mu$m; $R_a$ = 1.09 $\mu$m; $R_z$ = 7.09 $\mu$m
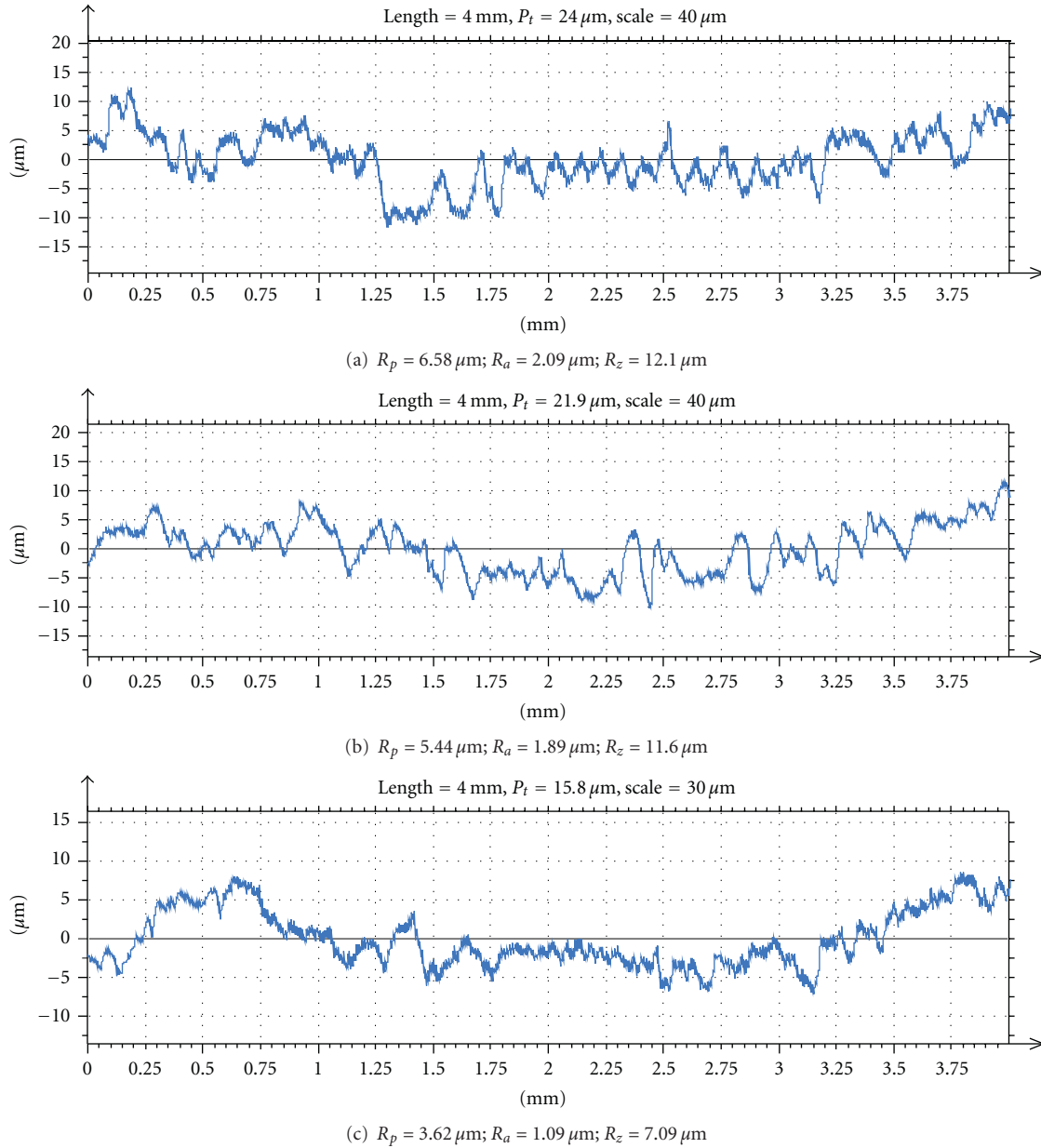
FIGURE 19: Surface roughness of the sample with 1% Sn (a), 1.5% Sn (b), and 2.5% Sn (c) across the sliding direction.

From the analysis of the surface roughness after the process of wearing it can be observed that the lower values of the roughness parameters are obtained for the samples with 2.5% Sn, which confirms the results regarding the coefficient of friction and wear rate for this material.

## 4. Conclusions

Considering the physical, mechanical, and tribological behaviour of the selected materials the following conclusions can be drawn.

(i) Alloy no. 3 exhibits optimum properties when sintered at 900°C for 50 minutes.

(ii) Generally, as the sintering temperature increases the smaller values of the density are obtained due to volumetric dimensional growth during liquid-phase sintering at higher temperatures.

(iii) A relatively homogenous microstructure is achieved when sintering at 900°C for 50 minutes with soft and strengthening phases distributed in the ferrite matrix and small pores in larger quantities with a relatively uniform distribution.

(iv) Tensile strength, hardness, and toughness are comparable to those of the existing iron-based materials [11–14].

(v) Tensile strength of 205 MPa, hardness of 139 $VH_5$, and toughness of 12.5 J/cm$^2$ were obtained for alloys sintered at 900°C for 50 minutes and containing 2.5% Sn due to the presence of strengthening phases which form at higher temperatures and longer sintering times.

(vi) At the $p \times v = 2.8$ MPa m/s the friction coefficient is about 0.1, the linear wear rate has the lowest value of $17.6 \times 10^{-5}$ mm/m, and also the gravimetric wear rate has the lowest value of $9.8 \times 10^{-2}$ mm$^3$/m. These results are explained on the basis of the presence of soft phases in the structure, which have low share strength in the substrate and during the high load tests are exposed to sliding. Also, $MoS_2$ solid lubricant additions contribute in the reduction of the coefficient of friction. On the other hand, wear rates exhibit lower values due to increasing the adhesive component at higher normal loads and exposure and transfer of the soft phases from the sample surface to the mating disc. As a consequence, the share stress at the sample surface increases.

(vii) Studying the tribological behaviour of the samples made from the selected materials and tested in dry friction condition (without lubricant) it was observed the dropping off of the friction coefficient as the tin content increases. The linear wear rate and the gravimetric wear rate are smaller as the amount of tin is greater.

(viii) Electronic microscopy analysis of the wear surfaces of the samples sintered at 900°C for 50 minutes and tested at $p \times v = 2.8$ MPa m/s shows deep wear tracks indicating that wear occurred due to combined action of adhesive and abrasive mechanisms with transfer and microcutting of the tested material. Also, the marginal regions of the samples with rolled and exfoliated layers highlight the material behaviour during wear process. Deeper scars along the sliding direction due to the strong adhesion between roughs in contact exhibit sample with 1% Sn and their aspect can be observed on the 2D surface profile. The wear surface of the sample with 2.5% Sn is less coarse with finer scars and a smaller number of particles detached from the sample surface. The difference between the scar aspects of the worn surfaces and also the difference between wear depths is emphasized on 2D surface profiles by pick-to-valley height, $P_t$, and roughness parameters, $R_a$ and $R_z$, which have the lowest values for the sample with 2.5% Sn.

## References

[1] A. G. Kostornov and O. I. Fushchich, "Sintered antifriction materials," *Powder Metallurgy and Metal Ceramics*, vol. 46, no. 9-10, pp. 503–512, 2007.

[2] A. G. Kostornov, O. I. Fushchich, and T. M. Chevichelova, "Structurization in sintering of antifriction powder materials based on iron-copper alloys," *Powder Metallurgy and Metal Ceramics*, vol. 46, no. 11-12, pp. 589–594, 2007.

[3] Verghese and K. Gopinath, "Influence of antimony additions on sintered iron-copper bearing materials," *Key Engineering Materials*, vol. 29-31, pp. 457–464, 1989.

[4] Y. M. Vasil'ev, G. A. Shvetsova, V. Y. Berent, and N. A. Bushe, "Antifriction properties of an iron-base material containing a manganese ultraphosphate," *Powder Metallurgy and Metal Ceramics*, vol. 21, no. 7, pp. 592–594, 1982.

[5] L. M. Berger, C. C. Stahr, S. Saaro, S. Thiele, M. Woydt, and N. Kelling, "Dry sliding up to 7.5 m/s and 800°C of thermally sprayed coatings of the $TiO_2$-$Cr_2O_3$ system and (Ti,Mo)(C,N)-Ni(Co)," *Wear*, vol. 267, no. 5-8, pp. 954–964, 2009.

[6] R. M. German, P. Suri, and S. J. Park, "Review: liquid phase sintering," *Journal of Materials Science*, vol. 44, no. 1, pp. 1–39, 2009.

[7] W.-F. Wang, "Effect of tin addition on the microstructure development and corrosion resistance of sintered 304L stainless steels," *Journal of Materials Engineering and Performance*, vol. 8, no. 6, pp. 649–652, 1999.

[8] M. Chandrasekaran and P. Singh, "Effect of PB additions on the friction and wear of sintered FE-Cu-SN-$MoS_2$," *International Journal of Powder Metallurgy*, vol. 32, no. 1, pp. 51–58, 1996.

[9] B. Sustarsic and L. Kosec, "Engineering properties of Fe-$MoS_2$ powder mixtures," in *Proceedings of the Powder Metallurgy World Congress & Exhibition*, pp. 316–321, Granada, Spain, 1998.

[10] S. Dhanasekaran and R. Gnanamoorthy, "Development of self lubricating sintered steels for tribological applications," in *Proceedings of the International Symposium of Research Students on Materials Science and Engineering*, Chennai, India, 2004, http://mme.iitm.ac.in/isrs/isrs04/cd/content/Papers/AIS/OR-AIS-1.pdf.

[11] A. Domsa, *Tehnologia Fabricarii Pieselor din Pulberi Metalice*, Bucuresti, Romania, 1966.

[12] A. Salak, *Ferrous Powder Metallurgy*, Cambridge International Science, Cambridge, UK, 1995.

[13] K. Tüfekci, C. Kurbanoğlu, E. Durak, and R. F. Tunay, "Friction and wear properties of Cu and Fe-based P/M bearing materials," *Journal of Mechanical Science and Technology*, vol. 20, no. 4, pp. 513–521, 2006.

[14] M. Morakotjinda, R. Krataitong, P. Wila et al., "Sintered Fe-Cu-C materials," *Chiang Mai Journal of Science*, vol. 35, no. 2, pp. 258–265, 2008.

*Research Article*

# A Characterization Method for Al Recovery from Dross Based on Compression at Elevated Temperatures

## S. Maropoulos, D. Kountouras, X. Voulgaraki, S. Papanikolaou, and I. Sanaidis

*Mechanical Engineering Department, Technical University of Western Macedonia, Koila, 50100 Kozani, Greece*

Correspondence should be addressed to S. Maropoulos, maropou@teikoz.gr

When aluminum or its alloys are melted, considerable amounts of dross are produced. The alloy type and the method used in the production of aluminum products play an important role in the amount of dross that will result as a byproduct. The current needs of the Al industry as well as economic and environmental factors demand the recovery of the pure material that is lost during dross removal by simple and efficient methods that can be applied within the foundry. Most cases of Al recovery employ methods of dross compression at high temperatures. This investigation attempts to develop a mathematical model to characterize the efficiency of the recovery process that can be implemented for any dross collection method or even compression device, facilitating the direct comparison of recovery methods.

## 1. Introduction

The continuous film formed on the surface of liquid Al, commonly referred to as dross, is a mixture of gasses, nitrides, carbides, and other substances, thus, partially partitioning to oxides [1, 2]. Due to the high temperatures that are present, the development of the above compounds is favored. As a result, a percentage of approximately 1.5–2.5% [3] of the total amount of molten material is characterized as dross and removed from the liquid prior to casting. However, during the removal of dross, a certain amount of pure metal is trapped within its mass and is consequently wasted. Depending on the way dross is collected and removed from the foundry, it may contain up to 30–90% fully recyclable or recoverable aluminum [4, 5] while remaining Al oxides can be utilized in a series of other applications [6, 7].

The methods of dross removal in foundries are mainly empirical, hardly reproducible, and are carried out either manually or by automated mechanical methods. The criteria for implementing a dross collection method vary depending on economic and technical factors and the means available. Bearing in mind that the collected material is further processed in a number of ways, it is not an easy task to compare methods adapted by different foundries.

Recently there has been a continuously growing demand to recycle novel materials such as Al, not only because of the depleting Al-ore reserves but also due to the increasing effort to minimize the environmental footprint of industrial byproducts and waste.

The present investigation seeks to introduce a simple systematic way to compare Al recovery methods from dross based on compression at elevated temperatures regardless to the retrieval method or the employed device parameters. A mathematical model is developed, facilitating the characterization of the recovery process in terms of productivity.

## 2. Experimental Procedure

During dross collection, each lot of material taken may differ depending on a number of parameters such as removal speed, collection depth, and so forth. Most foundries employ automated [8] or manual collection by means of a mechanical ladle mounted on a clark or direct handling of the collection device by personnel [9]. In these cases the material removal process is not reproducible with regard to its composition since the aforementioned parameters cannot be kept constant as the surface shear of this procedure is described by rather complex phenomena [10].
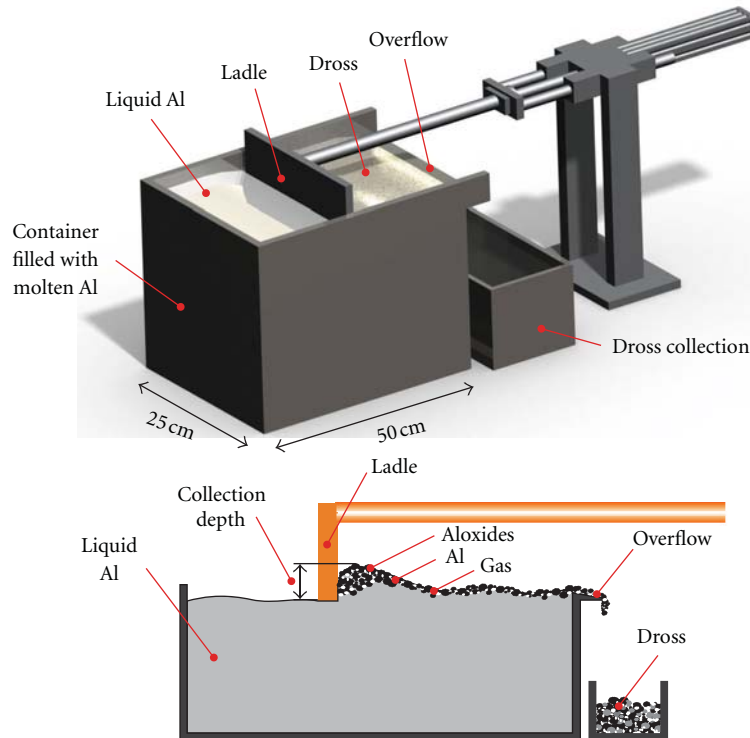
Figure 1: Automated dross collection.

Although the model which will be presented further on can characterize fluctuation processes, a laboratory scale setup, schematically presented in Figure 1, was developed to evaluate the effect of both collection depth and speed on the recovered material.

Two types of dross collection were considered in the present investigation, manual and automated (by means of the device shown in Figure 1). The collection speed of the automated procedure was kept constant, throughout each process, while two different ladle velocities were considered, 0.1 and 0.15 m/s. During the manual operation of the ladle, attention was given to maintain the collection speed within this range. This velocity range was selected to maintain the integrity of the oxide film, as higher collection speeds lead to tearing of this membrane. The dross was collected in a container receiving 180 gr of material, and each experiment was terminated upon collecting this amount. This facilitated the direct comparison between all scenarios, varying in removal speed and ladle depth.

In order to ensure the proper formation of the oxide film on top of the molten aluminium after each removal process, consecutive experiments were conducted at 20-minute time intervals.

Every batch of dross taken was crashed and sieved prior to processing. Grains less than 1 mm in diameter were removed, while grains from 1 mm to 2 cm were used resulting in the final ground dross.

The ground dross was then placed in the heated cylindrical container, illustrated in Figure 2. The container design introduced represents an optimized geometry deriving from
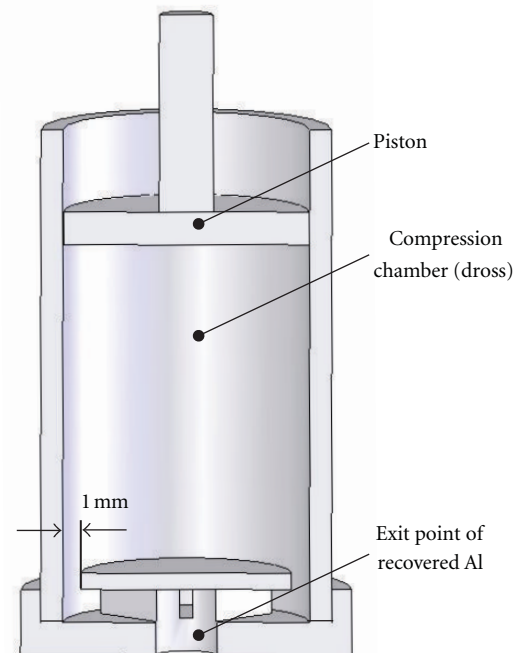


Figure 2: Cylinder used during Al recovery.

consecutive experiments with various piston bottoms (conical, multiple perforations and differing hole geometries, etc.).

The final geometry consists of a 380 mm high cylinder with a 55 mm diameter and a 1 mm peripheral exit gap elevated by 3 mm from the cylinder bottom. The extrusion hole was 43 mm in diameter and 5 mm high.

The aforementioned cylinder was heated to 800°C, prior to the experimental procedure, and the containing aluminium was compressed by a piston while the temperature was kept constant. The aluminum released from the dross flows through the small 1 mm peripheral gap in the bottom part of the device and is collected in a container placed below the apparatus. This recovery procedure was chosen since compression of dross is a common practice during Al retrieval [11–13].

During the experiments, the maximum pressure was predefined based on calculations considering the friction of a semisolid material within an extrusion container [14]. The pressure was applied by the hydraulic parts of the experimental setup, thus forcing the piston to move. The experiment was stopped when there was no change in the piston movement for the maximum applied pressure. During the whole process, the control unit of the device registered the piston displacement versus the resulting forces.

## 3. Mathematical Model of the Recovery Process

There are a number of methods for the processing of dross which have been developed since 1980 [15]. Nevertheless the collection of dross is based on the same principle, either through levity overflow or by skimming. Dross is composed of oxides, salts, pores and pure metal, thus, its volume $V_{total}$ can be described by

$$V_{total} = V_{oxide} + V_{salt} + V_{pore} + V_{metal}, \tag{1}$$

where $V_{oxide}$ is the volume of the oxides contained, $V_{salt}$ the volume taken up by salt, $V_{pore}$ the volume of the pores contained in the material which is usually air or foundry gases and finally, and $V_{metal}$ the volume of trapped metal.

The mechanical characteristic presenting the highest impact on the recovery process is the pressure at which the metal will drain from the oxides-salts. The morphology of the dross containing pores, ceramics (oxides), and Al resembles that of metal matrix composite materials.

As this is compressed, Al is removed and its measure of elasticity is constantly altered. The pores within the dross decrease, finally resulting in a mixture of oxides and salt which constitute the final measure of elasticity. It is worth mentioning that the relationship of the elasticity modulus of the composite material depends on the composition in metal pores and conglomerated oxides-salts.

Applying the rule of mixing (ROM) to (1) provides the elasticity modulus of this composite material ($E$) given by

$$E_{total} = a \times E_{oxide} + b \times E_{salt} + c \times E_{metal}, \tag{2}$$

where $a$, $b$, and $c$ are the volume percentage of oxides, salt and Al, respectively, and $E_{oxide}$, $E_{salt}$, and $E_{metal}$ the elasticity modulus of oxides, salt and Al. The volume percentage taken up by pores and gases is not taken into account in (2) since it does not modulate the materials elasticity modulus.
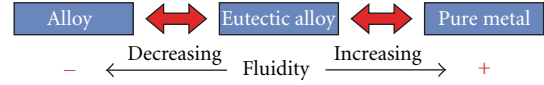


FIGURE 3: Fluidity dependency of metals based on composition.
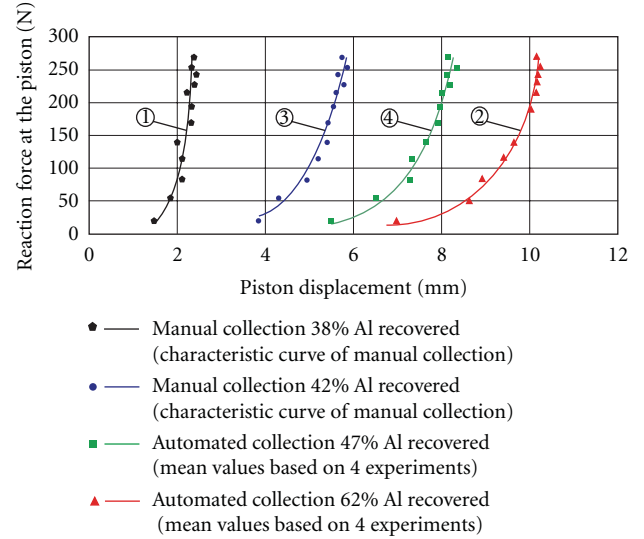


FIGURE 4: Experimentally determined values for 4 varying cases with the first method of a single collecting process per sample.

The fluidity of the collected material is a parameter strongly affecting the recovery process. Increased fluidity eases the procedure and improves the efficiency. The alloy components play a particular role in determining the fluidity, as does the temperature. The fluidity dependency of metals based on composition can be described by Figure 3 [16]. Based on this, the collected dross is additionally heated over the metal melting point during the recovery process to further increase the fluidity of the material.

During the compression of the recovered Al, the reaction force of the piston versus its displacement can be graphically presented as shown in Figure 4. Curves 1 and 3 represent characteristic manual dross collections selected from 40 experiments in total. They show the typical behavior exhibited by the experimental procedure. On the other hand, curves 2 and 4 relate to the automated collection and are the mean values of 4 experiments for each of the selected process parameters (collection speed, depth, etc.).

The experiments were repeated as there was no reproducibility in either collection method, due to the hydrodynamic effect of the subsurface liquid interacting in various ways with the oxide film collected.

The curves presented in Figure 4 show the tendency of the elasticity modulus of composite materials [17, 18].

The depths of cleaning in each sample are shown in Table 1.

Figure 5 shows the relationship between the percentage of recovered material and the depth of collection. By considering point A as the ideal process and B as the sloppy cleaning process, then AB is considered as the distance

Table 1: Cleaning depths of the experiments.

| Experiment | 1 | 2 | 3 | 4 |
|---|---|---|---|---|
| Depth (mm) | 4 | 12 | 6 | 8 |
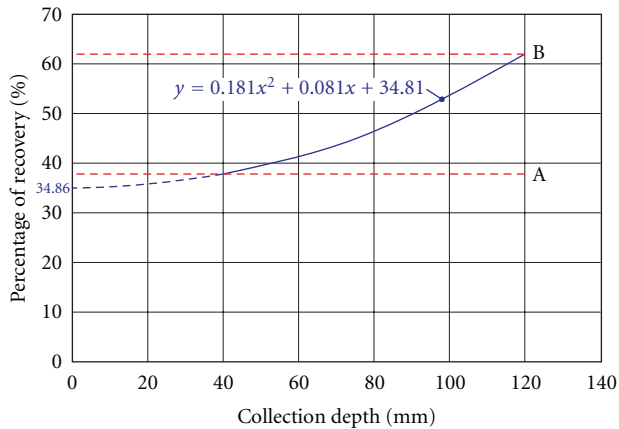


Figure 5: Percentage of recovery in relation to the depth of collection.
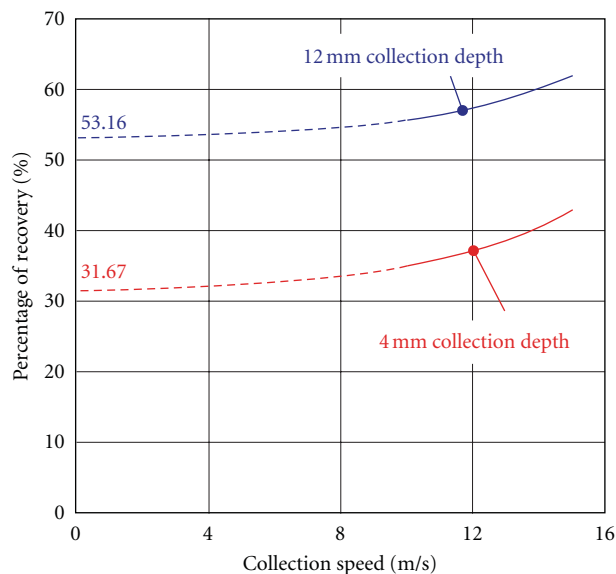


Figure 6: The dependence of percentage of recovery on collection speed.

between perfection and sloppiness of collection in the specific experiment.

A double derivative of the equation shown in **Figure 5** gives the minimum value of the curve which defines the minimum thickness of oxides that could be collected with the above procedure at 0.36 mm. Submerging the ladle at this depth during the automated processes results in a 32.1% percentage of Al recovery, which agrees well with the 34.86% corresponding to the theoretical optimum shown by the curve in **Figure 5**.

The dependence of percentage of recovery on collection speed is shown in **Figure 6**. As can be seen, the effect of the collection speed remains constant regardless of the collection depth selected.

## 4. Results and Discussion

A significant increase of collection speed would lead to tearing of the continuous film formed on the surface of liquid Al while forcing pure Al to drift along, thus, collecting more pure material rather than dross decreasing the efficiency and increasing the percentage of Al recovered. Increasing the collection depth follows the same principle; the deeper the ladle enters into the molten Al, the more pure Al is collected thus rendering the process less productive.

## 5. Conclusions

The presented approach to Al recovery proves that the percentage of recovered material is not indicative of the process quality since it may be attributed to overcollecting of pure Al. In order to compare a variety of reclaiming processes, the productivity of the process has to be considered.

## References

[1] Q. Han, W. Simpson, J. Zeh, E. Hatfield, and V. K. Sikka, "Dross formation during remelting of aluminum 5182 remelt secondary ingot (RSI)," *Materials Science and Engineering A*, vol. 363, no. 1-2, pp. 9–14, 2003.

[2] O. Manfredi, W. Wuth, and I. Bohlinger, "Characterizing the physical and chemical properties of aluminum dross," *Journal of Material*, vol. 49, no. 11, pp. 48–51, 1997.

[3] J. Mukhopadhyay, Y. V. Ramana, and U. Singh, "Extraction of value added products from Aluminium dross material to achieve zero waste," *Light Metals*, pp. 1209–1212, 2005.

[4] V. Kevorkijan, "Evaluating the aluminum content of pressed dross," *Journal of Material*, vol. 54, no. 2, pp. 34–36, 2002.

[5] S. Wang, H. Hu, Y. l. Chu, and P. Cheng, "Dross recovery of Aluminum alloy 380," in *Proceedings of the CastExpo*, Atlanta, Ga, USA, May 2008.

[6] K.-D. Bouzakis, E. Bouzakis, G. Skordaris et al., "Effect of PVD films wet micro-blasting by various Al2O3 grain sizes on the wear behaviour of coated tools," *Surface and Coatings Technology*, vol. 205, supplement 2, pp. S128–S132, 2011.

[7] K. -D. Bouzakis, G. Skordaris, E. Bouzakis et al., "Optimization of wet micro-blasting on PVD films with various grain materials for improving the coated tools' cutting performance," *CIRP Annals*, vol. 60, no. 1, pp. 587–590, 2011.

[8] "Robotic dross removal melts away labor pain," *Manufacturing Engineering*, vol. 124, no. 6, 2000.

[9] M. Ueda, S. Tsukamoto, S. Konda, and T. Ohtsuka, "Recovery of aluminum from oxide particles in aluminum dross using AlF$_3$-NaF-BaCl$_2$ molten salt," *Journal of Applied Electrochemistry*, vol. 35, no. 9, pp. 925–930, 2005.

[10] K. D. Bouzakis, A. Tsouknidas, and G. Maliaris, "A wire cutting test to check the temperature distribution in inductively heated cylindrical aluminium billets at semi-solid material state," *Journal of Materials Processing Technology*, vol. 210, no. 1, pp. 166–173, 2010.

[11] J. Julliard, L. Tirilly, and P. Vigier, "Apparatus for the recovery of liquid Aluminium by compression of hot dross," US Patent 4575056, 1986.

[12] J. Shen, S. S. Xie, and J. H. Tang, "Dynamic recovery and dynamic recrystallization of 7005 aluminium alloy during hot compression," *Acta Metallurgica Sinica*, vol. 13, no. 1, pp. 379–386, 2000.

[13] H. Yamagata, "Dynamic recrystallization and dynamic recovery in pure aluminum at 583K," *Acta Metallurgica Et Materialia*, vol. 43, no. 2, pp. 723–729, 1995.

[14] K. D. Bouzakis, K. Efstathiou, G. Paradisiadis, and A. Tsouknidas, "Experimental and FEM-supported investigation of wet ceramic clay extrusion for the determination of stress distributions on the applied tools' surfaces," *Journal of the European Ceramic Society*, vol. 28, no. 11, pp. 2117–2127, 2008.

[15] J. A. Taylor, J. F. Grandfield, and A. Prasad, "Dross processing technology," *Materials Science Forum*, vol. 630, pp. 53–60, 2009.

[16] K. R. Ravi, R. M. Pillai, K. R. Amaranathan, B. C. Pai, and M. Chakraborty, "Fluidity of aluminum alloys and composites: a review," *Journal of Alloys and Compounds*, vol. 456, no. 1-2, pp. 201–210, 2008.

[17] N. Michailidis, F. Stergioudi, A. Tsouknidas, and E. Pavlidou, "Compressive response of Al-foams produced via a powder sintering process based on a leachable space-holder material," *Materials Science and Engineering A*, vol. 528, no. 3, pp. 1662–1667, 2011.

[18] N. Michailidis, F. Stergioudi, and A. Tsouknidas, "Deformation and energy absorption properties of powder-metallurgy produced Al foams," *Materials Science and Engineering A*, vol. 528, no. 24, pp. 7222–7227, 2011.

*Review Article*

# Model of Fracture, Friction, and Wear Phenomena of Porous Iron

## A. A. Shatsov, I. V. Ryaposov, and D. M. Larinin

*Mechanical Technological Faculty, State National Research Politechnical University of Perm,*
*29 Komsomolskii Avenue, Perm 614990, Russia*

Correspondence should be addressed to A. A. Shatsov, shatsov@pstu.ru

Mechanical and tribotechnical features of powdered materials are strongly influenced by pore volume, fracture character, impurities, alloying, concentration inhomogeneity, friction conditions, and other factors. Pores also have influence on acceleration of diffusion processes and reduce undercooled austenite resistance. Annealed in hydrogen, ultra pure iron powder was used to study porous iron features. Toughness fracture and tribotechnical features had nonmonotonic dependence from porosity different from all known dependences got from technical iron powders. Researches brought out the fact that in process of porosity reduction by pressing and annealing cycles, the average dimension of porous is changed. According to the analysis of porous structure were created models of friction, wear, and fracture of pure porous iron.

## 1. Introduction

The last few decades studies conducted in highly technologically developed countries showed that proper choice of friction pairs from the position of tribology could save approximately 1.5% of national income [1]. The usage of powdered materials best of all suits to the conditions of economic feasibility, because it allows to replace expensive and scarce alloys, increase productivity, and vacate production space. For example, the presence of residual pores in the structure of the bearing material can increase details' durability from 1.5 to 10 times [2].

There are three groups of the main factors influencing the friction: technological (structure, mechanical, and physical properties), constructive (contact scheme, the macro- and microgeometry, surface friction), and operational (specific friction work, sliding velocity, specific load, temperature, presence of grease, medium).

The friction process causes the formation of surface and subsurface layers which are conditioned by one or another friction and wear mechanism.

The last years researches were aimed at mechanical characteristics determination, including fracture strength and its connection with tribotechnical and physical features [3–22].

The aim of this work is to investigate and to model the friction, wear, and fracture processes of ultrapure iron.

## 2. Fracture Toughness of Ultrapure Porous Iron

Dependence of fracture toughness $K_{IC}$ and strength on porosity $P$ is not always strictly monotonic function [3, 4]. Defining this dependence is necessary for both theoretical concepts of crack interaction with defects and for specific practical problems solution, for example, the choice of the porosity of construction products, which can provide the highest fracture toughness. The main condition for determining reliability of $K_{IC}$ is the proof of the crack propagation in plane strain. This requirement imposes limitations on sample size and crack length. Crack length should be at least 2 mm and together with a groove to be 0.45–0.55 height of the specimen (GOST 25.506-85). The height of the sample is usually taken 12 mm. According to the regulations, the most exacting requirements are imposed on the thickness, which should not be less than $\beta(K_{IC}/\sigma_{0.2})^2$, where $\beta = 2.5$. However, other factors like the flat fracture and absence of thinning edges and lips cut, even if the porosity of iron have a few percent, indicate the reliability of the results. Thus, for the iron of high purity factor of proportionality $\beta$ and the ratio between the thickness to $(K_{IC}/\sigma_{0.2})^2$ was 0.3-0.4 [23] for powder Ni-Mo-Cu steel $\beta = 1.6$ [24]; for high-ductility stainless steel at $P = 5\%$, $\beta = 0.04$ [25]; for nickel steels $\beta = 1.4$ [26].

TABLE 1: The dependence of powder materials fracture toughness on porosity and sample thickness.

| Number of the composition | Composition | Atmosphere and sintering mode | Porosity, % | The sample thickness, mm | Fracture toughness, MN/m$^{3/2}$ |
|---|---|---|---|---|---|
| 1 | | | 15 | 2.80 | 9.5 |
| | | | | 4.60 | 10.0 |
| 2 | | | 13 | Sample sizes: $40 \times 18.4 \times 90$ mm | 10.0 |
| 3 | PZh4M2 | Vacuum, 1200°C, 2 h | 10 | 5.50 | 10.5 |
| 4 | | | 9 | 6.45 | 10.0 |
| 5 | | | 10 | 9.75 | 9.5 |
| 6 | | | 3.6 | 4.30 | 23.9 |
| 7 | OSCh 6-2 | Hydrogen, 1200°C, 2 h | 4.0 | 7.55 | 23.8 |
| 8 | | | 7.3 | 4.80 | 19.1 |
| 9 | | | 7.5 | 9.10 | 18.9 |

Note: The iron grade OSCh 6-2—the average particle size is 5 $\mu$m, the carbon content is less than 0.02% in mass, the total concentration of other impurities is less than 0.001%.

The correctness of the definition of $K_{IC}$ was examined by varying the thickness of the samples (Table 1). For sample thickness ranging from 4.3 to 9.1 mm, $\beta$ varies from 0.2 to 5.5. The obtained values are within the limits of the measurement inaccuracy confidence interval, which gives grounds to take $K_Q$ for $K_{IC}$. In all cases the sample thickness of 3 mm provided a satisfactory convergence of the results.

The data (Table 1) prove the invariance of fracture strength to a sample thickness. However, this does not mean that $K_{IC}$ is invariant to the sample size for all porous steels and alloys, therefore, the influence of size ratios on the $K_Q$ should be determined experimentally for different materials.

The choice of ultrapure iron is connected to a necessity to minimize the unanswered effect of impurities. Other important factors determining the fracture toughness are fracture mode, porosity, composition, and heterogeneity of alloying elements. Most of these factors which influence the $K_{IC}(P)$ dependence could be eliminated by the selection of the material and the sample fabrication method. The effect of porosity on fracture toughness data cited in the literature is contradictory. For example, a nonmonotonic dependence of $K_{IC}$ on $P$ at room temperature and at $-180°C$ was determined [27]. A monotonic dependence $K_{IC}(P)$ has been noticed by other authors [23, 25, 26, 28–32].

The authors of [21] do not exclude that the appearance of nonmonotonic $K_{IC}(P)$ dependence is associated with redistribution of impurities, because the situation of high porosity it is energetically favorable for the impurities to locate at the free surface of the pores, as well as the seals they move into the matrix, concentrating at grain boundaries, thus reduce the level of fracture toughness.

Studies have shown [33] that comparing with the porosity, the more significant factor affecting the fracture toughness is the proportion of interparticle destruction; also a linear correlation between $K_{IC}$ and the proportion of transgranular cleavage (test temperature minus 196°C) was established.

Carbonyl iron OSCh 6-2 was annealed 1 hour in hydrogen at 450°C before pressing to minimize the influence of impurity atoms. The oxygen content weight in sintered samples of the iron did not exceed 0.01%.

For stochastically inhomogeneous bodies fracture toughness could be accurately estimated using the effective stress intensity factor $K_{IC}$ [34]. The structure of the sintered iron powder is a single-phase material containing pores of various sizes.

Fracture toughness of iron samples (PZh4M2) with porosity 10–16% practically coincides with that one given in [33]. The porosity reduction is accompanied by a change from interparticle to transgranular ductile fracture mode (Figure 1). Therefore, a monotonic $K_{IC}$ increase is associated with a reduction of the proportion of intercrystallite fracture due to increased interparticle metallic bonds. For the iron samples, a correlation between $K_{IC}$ and mechanical properties was established (Figure 2).

The relationship between intercrystallite and intragranular fracture components depends on the sintering atmosphere. Thus, after sintering at 1200°C, 4 h in vacuum the fracture toughness of the 10% porosity samples was 10-11 MN/m$^{3/2}$ and fracture mode was intercrystallite. After the same sintering in hydrogen, the fracture toughness of the same porosity iron samples (PZh4M2) was 20-21 MN/m$^{3/2}$, and fracture mode was transgranular. Other mechanical properties increased less significantly: $\sigma_B$ from 180 to 320 MPa, $\sigma_{0.2}$ from 100 to 140 MPa, and $\delta$ from 10 to 16%.

$K_{IC}$ values for samples of iron OSCh 2-6 were higher and the dependence of $K_{IC}$ on $P$ (from 3 to 7%) was nonmonotonic. Fracture mode was intragranular regardless of porosity (Figures 3, 4, 5, and 6). The detailed fractographs study revealed that the highest proportion of cleavage on the fracture surface was in the samples with 3.5–4% porosity. It corresponds to the inflection point of the fracture toughness on porosity dependence. The porosity changes leads to an increase of the ductile component of the fracture surface, and $P = 6\%$ of the sites of cleavage fracture were not observed. With increasing porosity, pits were less deep and surface resembled a honeycomb fracture [35].

(a)　　　　　　(b)　　　　　　(c)
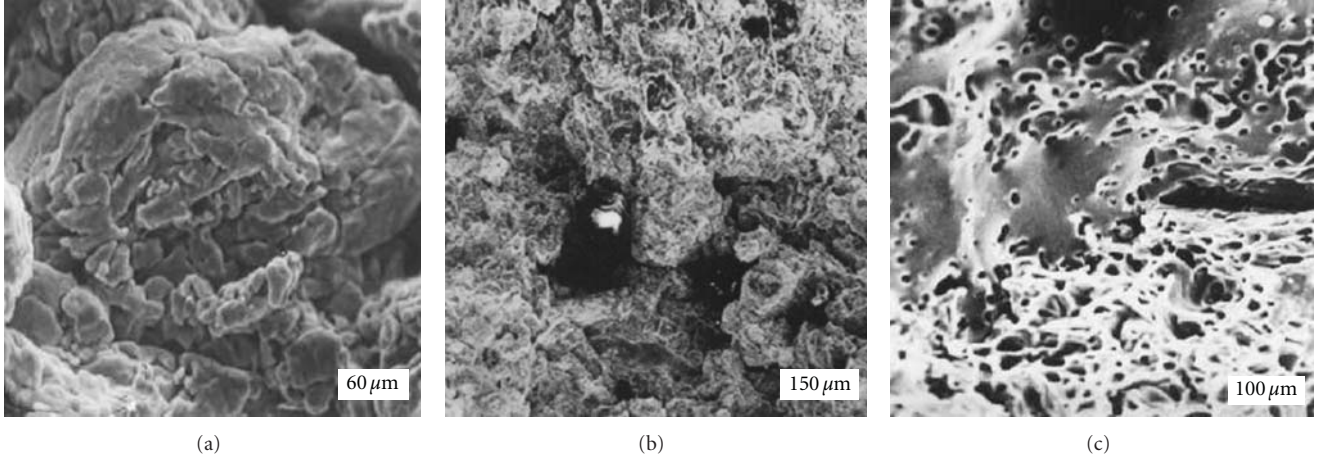
FIGURE 1: Fractography of the iron grade PZh4M2 specimens: (a) after pressing, ×500; (b) $P = 18\%$, ×200; (c) $P = 10\%$, ×700.



(a)　　　　　　(b)　　　　　　(c)
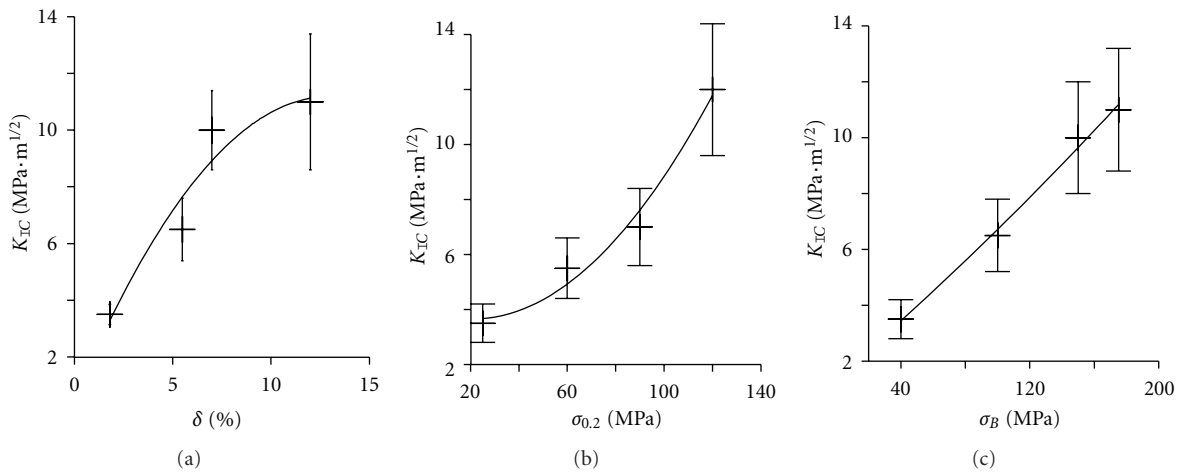
FIGURE 2: Mechanical properties and fracture toughness correlation of vacuum sintered samples from technical iron PZh4M2 grade.

Thus, the change in the ratio of ductile and cleavage component is a mechanism for implementing nonmonotonic $K_{IC}(P)$ dependence. But to understand the process of destruction of the porous body it is necessary to develop the model representations that connect fracture toughness to the characteristics of the porous structure.

Reduction of impurities concentration in the iron powder does not change $K_{IC}(P)$ dependence type, so one can assume that nonmonotonic decrease of $K_{IC}$ is the result of the interaction of cracks with the pores. This result is consistent with theoretical studies [22, 36, 37], proving the possibility of a nonmonotonic change of $K_{IC}$ by varying the structural defects.

Attention is drawn to the increased size of pores at $P = 3.5\%$, which corresponds to a singular point of $K_{IC}(P)$ dependence (Table 2). This fact gives a reason to suggest a relationship between fracture toughness and pore size distribution and, hence, the distance between the pores. Apparently, the influence of pores on the fracture toughness is not only due to the average porosity.

To describe the interaction of crack with pores its movement can be represented as the movement of a dislocation front. Reasons to study the propagation of the crack front by analogy with the dislocation front directly for pure iron are given in [38].

We assume that the pores are spherical, uniformly distributed and separated by a distance $2R$. Crack bending leads to a change in its distribution energy [39–41]:

$$g' = g + \frac{T}{R}, \tag{1}$$

$$K_{IC} = \sqrt{\frac{E \cdot g'}{1 - \mu^2}} = \sqrt{\frac{E}{1 - \mu^2}\left(g + \frac{T}{R}\right)}, \tag{2}$$

where $g$ is the crack distribution energy; $T$—linear crack front tension; $E$—elastic modulus; $\mu$—Poisson's ratio.

Expanding (1) in a series, since $g \gg T$, we find

$$K_{IC} = K_{IC}^0(P) + \frac{1}{2}\frac{E \cdot T}{(1 - \mu^2) \cdot K_{IC}(P) \cdot R}. \tag{3}$$
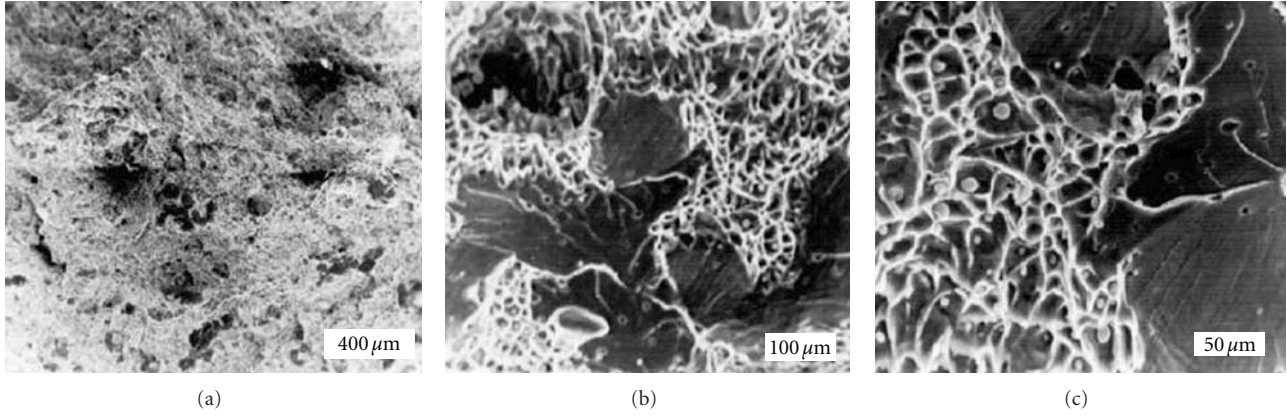
FIGURE 3: Fractography of the iron grade OSCh 6-2 with 2% porosity specimens: (a) ×75; (b) ×400; (c) ×750.
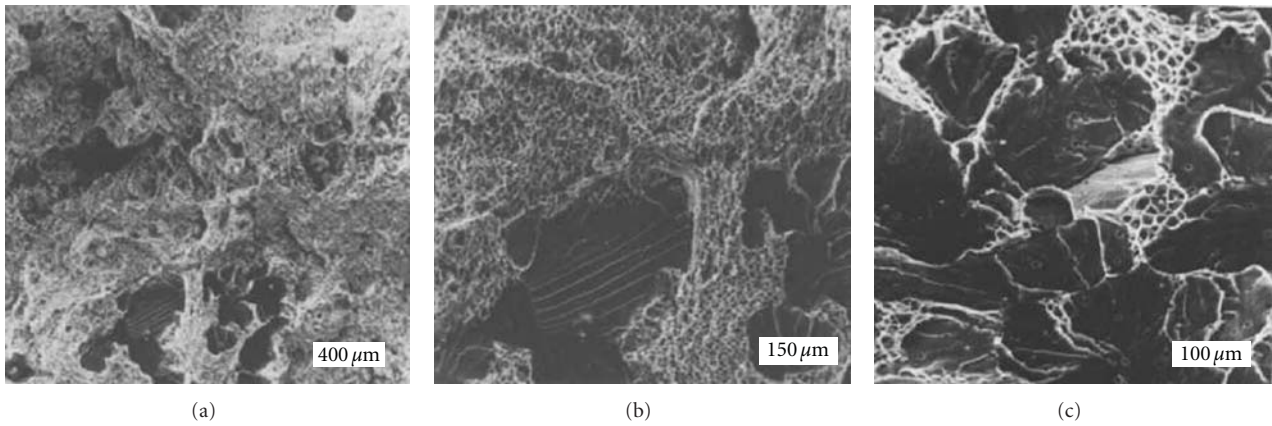


FIGURE 4: Fractography of the iron grade OSCh 6-2 with 3.6% porosity specimens: (a) ×75; (b) ×200; (c) ×400.

Equation (4) is got in correlation assumption of specific energy of uniform deformation ($A$) and effective surface energy ($\gamma_{eff}$) of the Griffiths-Orowan theory [42]:

$$K_{IC}^0 = \sqrt{\frac{0.8 \cdot l_d \cdot A \cdot E}{1 - \mu^2}}, \qquad (4)$$

$$A = \frac{(\delta_e - \sigma_{0.2}/E) \cdot (\sigma_{0.2} + 2\sigma_B)}{3} + \frac{\sigma_{0.2}^2}{2E}, \qquad (5)$$

where $l_d$—length dimension constant; $\delta_e$—uniform deformation; $\sigma_{0.2}$ and $\sigma_B$ yield strength and tensile strength, respectively.

$l_d$ is a constant in the limit $P \rightarrow 0$. Extrapolation of experimental data to zero porosity gives $K_{IC} = 35$ MN/m$^{3/2}$, $\sigma_{0.2} = 250$ MPa, $\sigma_B = 350$ MPa, $\delta = 49\%$, and $\delta_e = 26\%$. Similar values of mechanical properties obtained in [43–45].

Then we calculate $K_{IC}^0$ for all porosity values:

$$K_{IC}^0$$
$$= \sqrt{\frac{0.4 \cdot 10^{-3}[2(\delta_e(P) \cdot E(P) - \sigma_{0.2}(P)) \cdot (\sigma_{0.2}(P) + 2\sigma_B(P) + 3\sigma_{0.2}(P))]}{3\left[1 - \mu^2(P)\right]}}. \qquad (6)$$

Dependence $\mu = \mu(P)$ was established in [46]:

$$\mu(P) = \frac{(1 - P)\mu}{1 - P\mu}. \qquad (7)$$

For the iron powder [47]:

$$E(P) = E(1 - P)^{3/4}. \qquad (8)$$

As a result of fitting the experimental data by (3) we determined the value of $T = 3 \cdot 10^{-4}$ N. Average approximation accuracy (4%) indicates a good convergence of calculated and experimental results. The crack front tension can be determined directly from the expression:

$$T = \tau \cdot R, \qquad (9)$$

where $\tau$—crack movement stress.

The general idea is that the crack movement through the area with obstacles in it can be described on the assumption of the same principles as in dislocation movement which is described in details in [48] and later in [49]. The possibility of the crack movement is proved experimentally in [50]. In this case porous were studied as inhomogeneities (second phase). The equation was got in assumption of minimal front

(a)



(b)
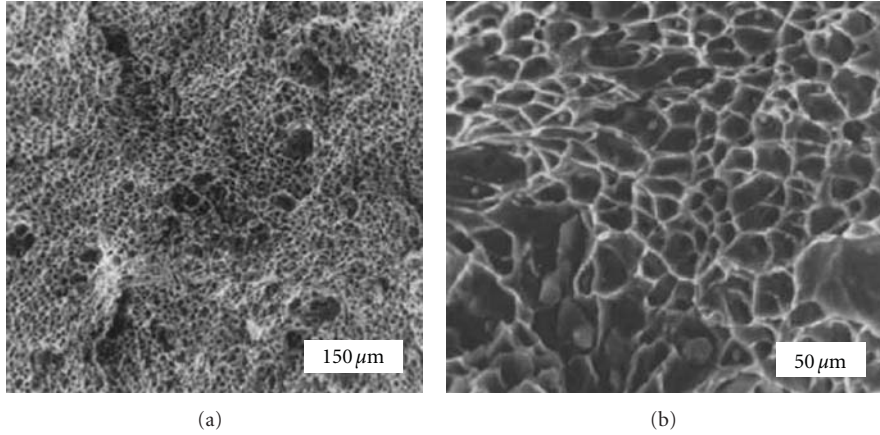
Figure 5: Fractography of the iron grade OSCh 6-2 with 5.9% porosity specimens: (a) ×200; (b) ×750.



(a)



(b)



(c)
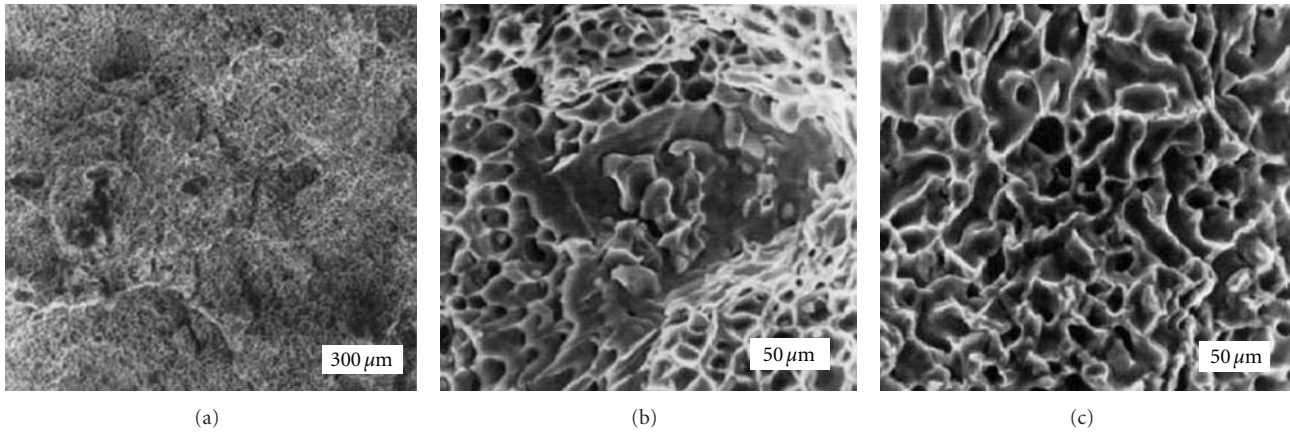
Figure 6: Fractography of the iron grade OSCh 6-2 with 7.3% porosity (a, b) and with 20% porosity (c) specimens: (a) ×100; (b) ×750; (c) ×750.

bend of the crack in condition of relatively large porous and long distance between them,

$$\tau = \frac{r^2 \cdot \pi \cdot}{2b_0 \cdot},$$ (10)

where $r$—pore radius; —interface energy; $= 1000$ ergs/cm$^2$ [51]; $b_0$—interatomic distance; $b_0 = 0.246 \cdot 10^{-9}$ m; —distance between the inhomogeneities (pores).

Then, as the porosity, for example $P = 7.5\%$, $T$ is equal to $2.5 - 25 \cdot 10^{-4}$ N, which is higher than, but has the same order with, a value of $T$, determined experimentally. The coincidence of the front crack tension value found experimentally and calculated from published data confirms the validity of expression (3).

As seen from (3), for effective crack interaction with the defects it is necessary that the distance between the defects was several times shorter than the size of the crack, the same view expressed in [51].

Thus, the nonmonotonic dependence of fracture toughness on porosity was established and when the effect of impurities is minimal. It was shown that the type of $K_{IC}(P)$ dependence is the result of crack interaction with pore

system, the maximum percentage of cleavage on the fracture surface coincides with a singular point of $K_{IC}(P)$ dependence.

A model explaining the deviation from a strictly monotonic decrease of fracture toughness with increasing porosity by crack front tension and allowing to predict fracture toughness of powder materials is given.

Note that the characteristics of plasticity may also have nonmonotonic dependence on porosity [51, 52].

## 3. Influence of Pores on the Friction and Wear of Iron

Mechanics of contact fracture offers a solution to the problem of wear for a half-space of moving on its surface Hertz plateau in the presence of horizontal and vertical cracks [53]. However, the features of porous materials allow to use a simple functional relation to the conservation of acceptable accuracy in many cases. First of all, if we proceed from the principle of superposition, for small friction ratio the contribution of the tangential component $\tau_z = -f q(x)$ is small. For example, increasing of the contour pressure on the order during sliding friction without lubrication of

TABLE 2: The dependence of porosity on the mechanical properties of OSCh 6-2 iron.

| Porosity, % | Average pore diameter, microns | $\sigma_{0.2}$ | $\sigma_B$ | $\delta$ | $\delta_e$ |
|---|---|---|---|---|---|
| | | MPa | | % | |
| 2.7 | 1.2 | 215 | 328 | 41 | 18 |
| 3.5 | 2.0 | 170 | 301 | 30 | 12 |
| 6.0 | 1.4 | 162 | 293 | 29 | 12 |
| 7.5 | 1.7 | 130 | 240 | 26 | 10 |
| 12.7 | — | 125 | 235 | 25 | 9.2 |
| 20 | 1.8 | 71 | 151 | 12 | 4.5 |

oil-impregnated steel PA-ZhGr1 with 20% porosity results in $f$ changes only by 17% and the wear rate—on the order. Secondly, the problem is solved for certain contact surfaces. At the same contact type, changes of $f$ are relatively small (compared to the differences between the friction ratios for different interactions types), and porous materials have the same trend. Relationship between wear rate and the variable parameters (especially pressure) within the proposed solutions were selected empirically using the coefficients that indirectly takes into account the contribution of the friction ratio.

Physico-mechanical and antifrictional properties of heterogeneous powder materials depend on several factors which are the chemical composition, heat treatment, variations in the density and distribution of alloying elements, content and distribution of related impurities, and so forth.

Some factors mentioned could be eliminated as a result of using pure iron [21, 54, 55]. But high content of impurities in industrial iron powder, insufficient porous structure description, and narrow ranges of the test pressure variation are the reasons of determination impossibility of the contribution of each measured parameters with high reliability.

The dependence of friction ratio $f$ and wear rate on the porosity $P$ and the pressure $P_n$ were studied in wide ranges ($P$ = 2–20%, $P_n$ = 0.25–4.2 MPa) for samples of pure iron (OSCh 6-2). Porosity was decreased by cycles of repressing and annealing. The size distribution of wear particles (Figure 7) were studied by microscope "Neophot-21". Distribution shows that wear fractions are considerably smaller then porous (Table 2) and can influence on friction conditions, the forming surface geometry, and it can influence especially strongly on oil layers appearance during boundary friction of infiltrated with oil samples.

Friction surface was studied by scanning microscope SEM-200 (Figure 8). Tribological properties were determined by SMC-2, with hardened steel 45 (GOST 26614-85) as a friction pair. X-ray diffraction analysis was made on a DRON-2 in the $\lambda$-Co radiation.

On the friction surfaces, inclusions (presumably oxides) and microcutting traces were found, Figure 8. Such surfaces are typical for powder compacts, working at hard conditions. The friction ratio has a pronounced nonmonotonic dependence on the porosity with a maximum about $P$ = 4%, which coincides with the minimum of $K_{IC}(P)$ dependence.
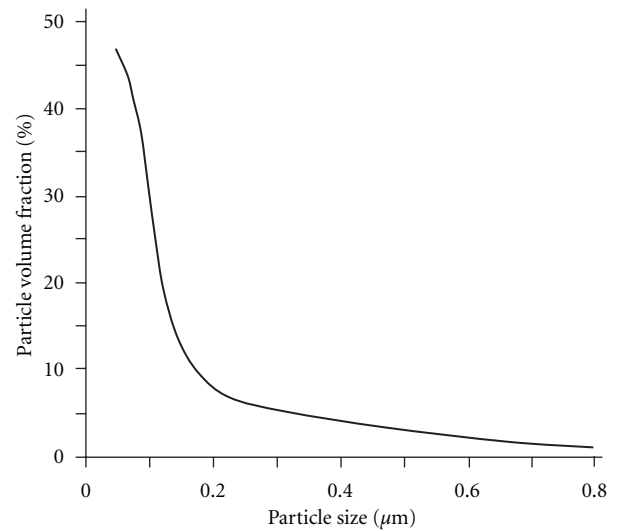


FIGURE 7: The size distribution of wear particles.

Since there is a correlation between friction ratio and wear characteristics, and wear resistance is related to pore size [56], it can be assumed that the local extremum of $f(P)$ is also associated with the peculiarities of the porous structure.

Narrow ranges of friction ratio variation allow to suggest prorated relationship between contour ($P_c$) and nominal pressure ($P_n$) [57, 58].

The experimental data was treated as follows. For each value of porosity, friction ratio deformation component $f_d$ [59] was calculated (11), suggesting that the conditions of the unsaturated plastic contact would be met. The equation was got in assumption of an additive contribution of molecular and deformative component of friction force. Deformative component is caused by the deformation of a less hard body by a harder one:

$$f_d = 0.5 \; {}^{1/2}\left(\frac{P_c}{HB}\right)^{0.25} \approx \left(C \cdot \frac{P_n}{HB}\right)^{0.25}, \qquad (11)$$

where —microroughnesses characteristic of a rigid material of the friction pair, $P_c$—contour pressure, and HB—hardness, $C$—constant. The value of was in the range $10^{-1}$–$10^{-3}$ [59].

(a)                                          (b)
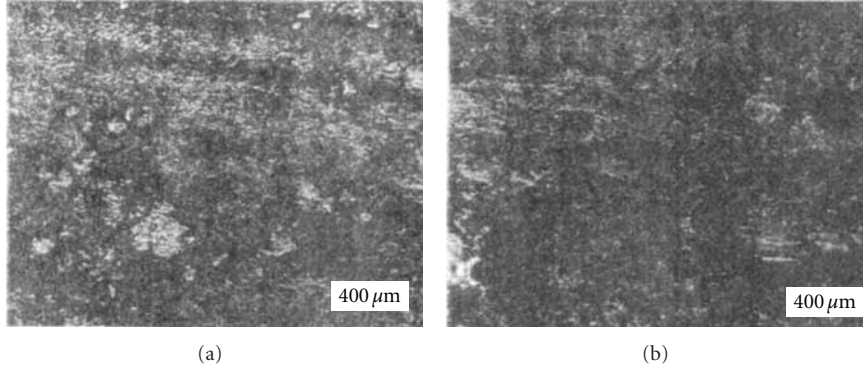
FIGURE 8: Friction surface of porous iron OSCh 6-2 specimen, ×50: (a) 2% porosity, (b) 20% porosity.

Type of mechanical treatment determines the value of the microroughnesses characteristic. The pressure $P$ and the hardness values are shown in Table 3.

In the first approximation, the molecular component of friction ratio $f_m$ decreases proportional to $(1 - P)$, since $f_m$ is proportional to the area $A$, where shear stresses $\tau$ appear. This is due to the fact that the pore size (several microns) in 1-2 orders of magnitude higher than the arithmetic mean deviation of profile Ra = 0.09 micron, hence, the contact between the surfaces in the area of the pores is unlikely. For a porous material [59], assuming $f_m$ decreasing in $(1 - P)$ times and the proportionality of $P_n$ and $P_c$ and subsequent calculating the $\beta$ and $\tau$, we can write

$$f_m = (1 - P)\left(\beta + \frac{\tau_0}{P_n}\right), \tag{12}$$

where $\beta$ and $\tau_0$ are friction characteristics depending on the friction conditions.

Friction characteristics $\beta$ and $\tau_0$ were calculated for each value of porosity, varying only the $P_n$, and then by the least squares method we found expressions for $\beta$ and $\tau_0$ from $P$:

$$\beta(P) = 0.00677 + 0.0103 \cdot P - 0.000394 \cdot P^2, \tag{13}$$

$$\tau_0(P) = 0.05(5) + 0.000532 \cdot P^2 - 0.0000267 \cdot P^3. \tag{14}$$

The number of regression equations members and their significance was determined by minimizing the residual variance $S_{ost}$ [60], the model adequacy was tested by the Fisher criterion $F$.

For the significance level 0.25, that is, the probability that the hypothesis can be rejected, the tabulated value of $F$ is 2.0. The values of $F$, equal to 2.3 and 7.7, calculated from expressions (13) and (14), respectively, exceeded tabular values, therefore, the equations are adequate.

Behavior of stressed porous materials has some special features [61]. Firstly, the pores reduce the range of physical and mechanical properties of the material, and secondly, pores are obstacles for dislocation motion and crack growth.

Assuming that the separation of the wear particles is due to crack formation and its subsequent growth, and as the pore was examined as an obstacle for the crack movement

which is similar to the dislocation movement, so stress can be calculated by the formula [48]:

$$\tau_m = \frac{a \cdot G \cdot B}{R}, \tag{15}$$

where $\tau_m$—crack movement stress in porous material; $a \approx 1$—coefficient; $G$—shear modulus; $B$—Burgers vector; $R$—the distance between the pores. $\tau_m$ does not act on the entire area, but only in places of contact. The bearing surface curve is usually given with $t_p$-$\varepsilon$ coordinates. On the basis of theoretical researches, Kragelskii and Demkin proved that the Kragelskii-Demkin equation can be used for the top of the bearing surface curve [59]:

$$t_p = b \cdot \varepsilon^\nu, \tag{16}$$

where $t_p$—relative contact area; $b$ and $\nu$ are bearing surface curve parameters; $\varepsilon$—relative approach.

The bearing surface curve parameters $b = 3.5$ and $\nu = 1.8$ were taken from [59]. Kragelskii and Mihin established during theoretical and empirical studies that real field of contact is proportional to applied load and doesn't depend on roughness of the surface (during a plastic contact). It terms of it relative approach can be determined with the formula [59]:

$$\varepsilon = \left(\frac{\alpha_1 \cdot C1 \cdot P_n}{b \cdot \text{HB}}\right)^{1/\nu}, \tag{17}$$

where $\alpha_1$—the coefficient depending on the type of contact (it varies from 0.5 to 1) $\alpha_1 \approx 0.75$; $C1$—the constant that relates the contour and nominal pressure.

Since the relation of tensions acting on contour area ($\tau_m \cdot t_p$) to contour pressure $P_c$ is analogous to a corresponded forces relation [62], so dependence of inhibition of the crack in the pores on the friction ratio can be determined from the expression:

$$f = \frac{\tau_m}{C1 \cdot P_c} \cdot t_p, \tag{18}$$

where $\tau_m$—stress; $f$—friction ratio change. Therefore, the approximation value of $f_m$ was carried out further in view of $f$. Accounting of the possibility of crack inhibition by

TABLE 3: Iron powder wear characteristics.

| $P$, % | $f$ | $f$-$f_d$ | $f$ | $P^{-1}$, MPa$^{-1}$ | $f_m$ Experimental | $f_m$ Calculated (12) | HB |
|---|---|---|---|---|---|---|---|
| 2 | 0.22 | 0.145 | 0.036 | 2.80 | 0.148 | 0.172 | 101 |
| | 0.19 | 0.096 | 0.024 | 1.10 | 0.098 | 0.083 | |
| | 0.15 | 0.023 | 0.026 | 0.34 | 0.023 | 0.044 | |
| | 0.33 | 0.261 | 0.023 | 4.20 | 0.272 | 0.283 | |
| | 0.26 | 0.173 | 0.022 | 1.70 | 0.180 | 0.120 | |
| 4 | 0.21 | 0.112 | 0.020 | 1.00 | 0.117 | 0.087 | 95 |
| | 0.17 | 0.053 | 0.013 | 0.50 | 0.055 | 0.063 | |
| | 0.16 | 0.030 | 0.017 | 0.33 | 0.031 | 0.050 | |
| | 0.22 | 0.141 | 0.058 | 3.00 | 0.154 | 0.150 | |
| 8.6 | 0.17 | 0.105 | 0.052 | 1.20 | 0.096 | 0.100 | 76 |
| | 0.18 | 0.067 | 0.047 | 0.71 | 0.073 | 0.082 | |
| | 0.17 | 0.072 | 0.043 | 0.36 | 0.070 | 0.071 | |
| | 0.22 | 0.146 | 0.065 | 4.0 | 0.169 | 0.148 | |
| 13.6 | 0.17 | 0.117 | 0.056 | 1.6 | 0.116 | 0.097 | 75 |
| | 0.20 | 0.074 | 0.056 | 0.94 | 0.086 | 0.090 | |
| | 0.22 | 0.13 | 0.10 | 2.80 | 0.163 | 0.170 | |
| 20 | 0.17 | 0.056 | 0.089 | 1.10 | 0.07 | 0.093 | 48 |
| | 0.17 | 0.04 | 0.083 | 0.65 | 0.05 | 0.073 | |

Note: $= 3.5 \cdot 10^{-2}$.

pores does not improve the approximation [62], as such mechanism can operate only when the crack path to fracture, significantly longer than the distance between the pores.

In the experiment discussed, the composition of wear particles corresponded to $Fe_2O_3$. Their size (see Figure 7) was much smaller than the distance between the pores, so a necessary condition for crack inhibition by pores (crack blunting) was not satisfied.

However, the increased size of pores at $P \approx 4\%$ corresponds to the largest value of $f$, which indicates a relationship between the inhibition of dislocation motion and crack growth. Regardless of the mechanism by which the dislocation overcomes obstacle, stress is always inversely proportional to $R$ [48].

The growth of pore size and the elongation of the distance between pores relieve the deformation in the active area, and it leads to growth of the plastically deformed contacts portion and the friction ratio. According to [63] the transition from elastic to plastic contact leads to a greater dependence of $f_d$ on $P_c$ and (in the case of elastic contact $f_d \sim p_c^{0.2} \cdot {}^{0.4}$, and plastic contact $f \sim p_c^{0.25} \cdot {}^{0.25}$, as to an increasing of $f_m$ (in the case of elastic contact $(f_m - \beta) \sim p_c^{-0.2} \cdot {}^{-0.4}$, and plastic contact $(f_m - \beta) \sim HB^{-1}$. Therefore, the most probable cause of the local extremum of the friction ratio dependence on the porosity is increased size of pores at $P \approx 4\%$. An indirect confirmation of this assumption is the reduction of the difference between the maximum and average values of $f$ with contour pressure increasing (i.e., an increasing of the proportion of plastic contact).

Features of porous materials [55, 64, 65] allow us to relate the friction surface characteristics and the material structure with wear resistance, Table 4, Figure 9.
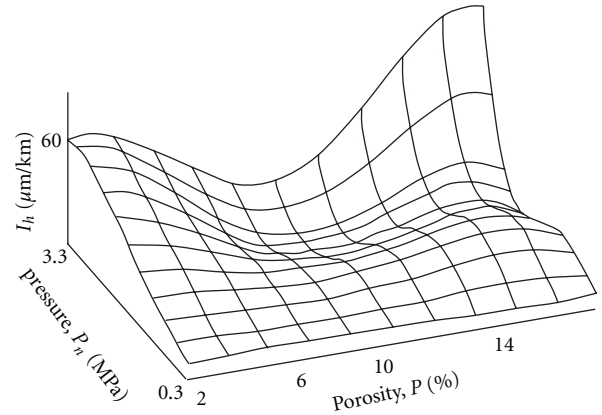


FIGURE 9: Response surface of $I(P, P_n)$.

Iron wear during dry friction on steel is a fatigue wear [66, 67].

At a certain stage of the interaction surface reaches steady state characterized by a constant dislocation cluster density in the slip bands; lattice parameters deflection and of dislocation density at a depth of 10–15 mm remains constant [64, 67].

Thus, there are the necessary prerequisites for interpreting experimental results involving the major tenets of the theory of fatigue wear. Specific linear wear rate $(i_h)$ was got in assumption of fatigue character of the wear. This assumption was based on material volume worn for one action, which is proportional to deformed volume and is inversely proportional to a number of acts leading to metal

TABLE 4: Iron powder characteristics.

| P, % | $I_h$, microns/km | | P, MPa | $K_{IC}$, MPa · m$^{1/2}$ | $\mu$ | $d \cdot 10^6$, m | HB |
|---|---|---|---|---|---|---|---|
| | Experimental | Calculated (27) | | | | | |
| 2 | 6.2 | 3.8 | 0.35 | 32.0 | 0.28 | 1.14 | 101 |
| | 9.3 | 12.2 | 0.89 | | | | |
| | 24.0 | 23.7 | 1.49 | | | | |
| | 66.8 | 57.6 | 2.95 | | | | |
| 4 | 3.7 | 2.5 | 0.24 | 24.6 | 0.28 | 2.02 | 95 |
| | 7.0 | 8.1 | 0.60 | | | | |
| | 18.6 | 15.6 | 1.00 | | | | |
| | 40.9 | 38.0 | — | | | | |
| | 60.4 | 63.9 | 2.00 | | | | |
| 8.6 | 4.6 | 3.5 | 0.33 | 18 | 0.27 | 1.78 | 76 |
| | 10.6 | 11.4 | 0.83 | | | | |
| | 20.0 | — | 1.40 | | | | |
| | 23.3 | 22.2 | 2.80 | | | | |
| | 69.8 | 90.8 | 4.20 | | | | |
| 13.6 | 4.3 | 3.7 | 0.25 | 17 | 0.26 | 1.79 | 75 |
| | 11.2 | 9.0 | 0.64 | | | | |
| | 23.2 | 17.1 | 1.06 | | | | |
| | 4.6 | 3.7 | 0.36 | | | | |
| 20 | 16.3 | 11.9 | 0.90 | 8 | 0.25 | 1.83 | 48 |
| | 21.1 | 22.9 | 1.50 | | | | |
| | 62.6 | 57.8 | 3.10 | | | | |

fracture [63]:

$$i_h = \frac{\sqrt{\nu/4}}{2(\nu + 1)n_{kr}} \cdot \sqrt{h/R_{cv}}, \quad (19)$$

where $h$—the rapprochement between the friction surfaces; $R_{cv} = 77$ microns [68]—the radius of curvature; $n_{kr}$—the number of cycles, leading to the fracture.

Integral linear wear rate $I_h$, and specific $i_h$ wear rate are related by [69]:

$$I_h \approx i_h \cdot t_p \approx \frac{\sqrt{\nu/4}}{2(\nu + 1)n_{kr}} \cdot \sqrt{h/R_{cv}} \cdot t_p. \quad (20)$$

Rapprochement between the two surfaces when the unsaturated plastic contact takes place [59]:

$$h = \varepsilon \cdot R_{\max} = \left( \frac{\alpha \cdot P_c}{b \cdot \text{HB}} \right)^{1/\nu} \cdot R_{\max}, \quad (21)$$

where $R_{\max}$—the greatest distance between the bumps and hollows within the gauge length.

Solving (19)–(21), we obtain the basic equation of wear

$$I_h = \frac{0.0156}{n_{kr}} \cdot \left( \frac{P_c}{\text{HB}} \right)^{1.28}. \quad (22)$$

Fatigue wear theory assumes localized damage in a small volume. As follows from the fracture mechanics, the separation of particles occurs when the stress concentration reaches the critical value $K_{IC}$.

This magnitude of stress concentration corresponds to a critical crack length $l_c$. Dependence of stress intensity

factor $K$ with the crack propagation rate $dl/dN$ in case of endurance fracture determined by Paris formula:

$$\frac{dl}{dN} = A(K)^n, \quad (23)$$

where $N$—number of cycles; $A$ and $n$—coefficients. Fatigue crack growth studies have shown that the coefficient $A$ depending on the strain hardening varies from $1.16 \cdot 10^{-5}$ to $6.77 \cdot 10^{-7}$; $n$ exponent reduces from 4.0 (for the degree of cold deformation of 50%) to 2.88 (at baseline) [70].

The stress intensity on the crack top determines stress intensity factor $K$ which is a tension and crack length $l$ function. For short cracks ($l/a_r < 0.03$, $a_r$—contact pad radius) it is written in the paper [53] like

$$K = 2\sigma_y\sqrt{l}, \quad (24)$$

where $\sigma_y$—fracture stress; $l$—crack length. In the case of Hertz contact at the contact area interface [53]:

$$\sigma_y = \frac{1 - 2\mu}{2} \cdot P_c. \quad (25)$$

The contact between the friction surfaces is carried out only in the microroughnesses contact plane. In this case, a critical crack length which is corresponded to a critical volume of stress intensity factor $K_{IC}$, the real contact area is counted by introducing $t_p$ taking into account (16), (17), (24), and (25) can be written like

$$l = \left[ \frac{K_{IC} \cdot t_p}{(1 - 2\mu) \cdot P_c} \right]^2 = \left[ \frac{0.75 \cdot K_{IC}}{\text{HB}(1 - 2\mu)} \right]^2. \quad (26)$$

For the initial size of the defect, by analogy with [56] a half the diameter of the pores ($l_0 = d/2$) was taken. The values of $d$, $K_{IC}$, and $\mu$ were taken from [70].

The deformed volume fracture occurs when $K$ reaches a value $K_{IC}$, which corresponds to the critical defect size $l$ and the value of $N = n_{kr}$. Solving expressions (22), (23), (26), and assuming a linear relationship between $P_n$ and $P_c$, we have a formula to determine the wear rate.

Fracture of the deformable volume happens when $K$ reaches $K_{IC}$ value that is corresponded to a critical defect size $l$ and $N = n_{kp}$ value. Substituting (23), (26) in (22) and ignoring the equation got on conditions that half of the pore diameter was taken as an initial defect size ($l_0 = d/2$), on the analogy of paper [56] implying linear connection between $P_n$ and $P_c$, a formula for wear intensity was gotten

$$
I_h
$$

$$
= \frac{0.156 \cdot (P_n/\mathrm{HB})^{0.128} \cdot (n/2 - 1) \cdot A\big[(1-2\mu)\,\mathrm{HB}/0.75\big]^n}{(d/2)^{(1-n/2)} - (0.75 K_{IC}/(1-2\mu)\,\mathrm{HB})^{(2-n)}},
\tag{27}
$$

where $d$—the average pore diameter.

$K_{IC}$, $d$, and $\mu$ values were taken from paper [70]. Thus linear intensity of wear is determined by load, hardness, crack growth resistance, structure characteristic element size-pore size, Poisson ratio, and fatigue fracture parameters.

Fitting the experimental data by expression (27), the values of $A = 1.38 \cdot 10^{-7}$ and $n = 2.11$ were determined. As seen from Figure 9, the function $I_h(P)$ is nonmonotonic over the entire range of variation of $P_n$. A similar result for the constant values of pressure and a wide range of $P$ was experimentally obtained in [55]. Good agreement between the values of the coefficients $A$ and $n$ with the published data [71] and a satisfactory approximation of the experimental results confirm the correctness of the approach adopted for the study of porous iron.

## 4. Lubricated Friction and Wear Processes

Boundary friction conditions of powder materials are typical for most parts functioning. This mode is performed during startup and shutdown, even if the products are designed for operation in a hydrodynamic lubrication [72]. The tests differed only in that the oil in the friction zone was fed through a rotating counterbody dipping into the bowl with the lubricant, Table 5.

Tables 4 and 5 show that for identical values of porosity and pressure the friction ratio value decreases several times with lubrication. It changes the dependence of $f$ on the pressure. Under dry friction an increase in pressure leads to a decrease in the $f$ value, but under lubricated friction pressure increasing results in $f$ increase. This form of the function $f(P)$ can be explained as follows. During elastic unsaturated contact friction ratio dependence on major friction unit characteristics $\tau_0$ and $\beta$, mechanical features of less hard material of friction pair ($\mu$, $E$), contour pressure and

roughness of harder element of friction pair ( ) according to [63] looks like

$$
f = \frac{2.4\tau_0\big(1 - \mu^2/E\big)^{4/5}}{P_c^{1/5} \cdot \quad^{2/5}} + \beta + 0.23\alpha_g P_c^{1/5} \quad^{2/5}\left(\frac{(1-\mu^2)}{E}\right)^{1/5},
\tag{28}
$$

where $\alpha_g$—coefficient of hysteresis losses under friction.

Equation for elastic unsaturated contact has the same structure and is different only in indexes $P_c$ and , $\mu$, $E$ and constants values.

The presence of lubricating film dramatically reduces the frictional bond shear strength $\tau_0$, and hence the contribution of the first term of (28). Deformation component of the friction ratio is proportional to the contour pressure with a small exponent, as it observed experimentally. Features were observed only when $P = 8.6\%$ (a transition from open to closed porosity occurs), and when $P = 4\%$ (a local extremum of the pore size detected) [70]. The porous structure affects the surface deformation in the active area [56], so that the greatest value of the friction ratio is connected with the extreme size of the pores [62]. Low friction ratio values for high porosity samples can be explained, apparently, by the fact that in this experiment with $P > 10\%$ all porosity is open, and it facilitates the circulation of oil and heat removal from the friction surfaces. The relatively low surface temperature makes it difficult to deform and promote $f$ decreasing.

Expression (28), Table 5, correctly reflects the trends of $f(P)$. Numerical processing of experimental data have not performed as well as the ranges of the friction ratio for most porosity values are small and the accuracy of $f$ at low pressures, comparable with the difference between the test results.

The thickness of oil layer was estimated according to the equation [72] which is applied in case of cylinders contact:

$$
\frac{h}{R_{cv}} = 1.65\left(\frac{(V_1 + V_2) \cdot \alpha_p \cdot V}{2R_n}\right)^{0,73} \cdot \left(\frac{P_n}{E/(1-\mu^2)}\right)^{-0.18},
\tag{29}
$$

where $V_1$ и $V2$—counterbodies' velocities; $V = 8.7 \cdot 10^{-8}$ m²/kg—oil dynamic viscosity; $\alpha_p = 4.1 \cdot 10^{-3}$ kg·s/m²—oil piezocoefficient; $R_n$—reduced radius of curvature.

Calculations showed that the porosity has a little influence on the oil layer thickness (Figure 10), which probably explains the weak dependence of the friction ratio on $P$ at low pressures.

The expression (29) tested with the pressure transducer DD-10 as follows. The sample was set and lap it dry. The sensor readings were calibrated, depending on the bias. Under dry friction the sensor readings were recorded and then counterbody was dipped into the oil. At a pressure of 0.25 MPa the rapprochement $h$ changed to 1.0–1.5 microns; this agrees well with Figure 10. At higher pressures (about 1 MPa) the accuracy of determining the change in approach is close to the calculated value of the oil film, at a pressure below 0.25 MPa tests were not carried out due to specific means for setting the sample.

The microhardness of the structural components of the friction surface was from 120 to 450 HV$_{0.05}$ (areas with

TABLE 5: Antifriction properties of iron under limited lubrication.

| P, % | Hardness, MPa | P, MPa | f | $I_h$, microns/km | | $d \cdot 10^6$, m |
|---|---|---|---|---|---|---|
| | | | | Experimental | Calculated (39) | |
| 2 | 1010 | 0.35 | 0.05 | 0.6 | 1.3 | 1.14 |
| | | 0.89 | 0.05 | 0.9 | 1.6 | |
| | | 1.5 | 0.07 | 1.6 | 2.1 | |
| | | 3.0 | 0.07 | 2.9 | 2.8 | |
| | | 4.5 | 0.07 | 3.3 | 3.4 | |
| 4 | 950 | 0.24 | 0.05 | 1.7 | 1.4 | 2.02 |
| | | 0.60 | 0.05 | 2.3 | 1.7 | |
| | | 1.0 | 0.09 | 2.9 | 1.9 | |
| | | 2.0 | 0.12 | 3.5 | 2.5 | |
| | | 3.0 | 0.12 | 3.7 | 3.0 | |
| 5.9 | 860 | 0.33 | 0.05 | 0.9 | 1.3 | 1.36 |
| | | 0.83 | 0.05 | 1.4 | 1.7 | |
| | | 1.4 | 0.06 | 2.0 | 2.0 | |
| | | 2.8 | 0.06 | 2.3 | 2.7 | |
| | | 4.2 | 0.06 | 4.0 | 3.3 | |
| 8.6 | 760 | 0.33 | 0.05 | 1.3 | 1.5/0.76 | 1.78 |
| | | 0.83 | 0.05 | 1.6 | 1.7/1.2 | |
| | | 1.4 | 0.09 | 1.8 | 2.0/1.5 | |
| | | 2.8 | 0.09 | 2.3 | 2.7/2.1 | |
| | | 4.2 | 0.12 | 3.1 | 3.5/2.5 | |
| 13.6 | 750 | 0.25 | 0.04 | 0.84 | 0.88 | 1.79 |
| | | 0.64 | 0.04 | 1.0 | 1.0 | |
| | | 1.06 | 0.06 | 1.6 | 1.3 | |
| | | 2.12 | 0.06 | 1.7 | 1.3 | |
| | | 3.18 | 0.07 | 3.5 | 2.2 | |
| 20 | 480 | 0.36 | 0.05 | 0.87 | 1.0 | 1.83 |
| | | 0.90 | 0.05 | 1.7 | 1.6 | |
| | | 1.5 | 0.06 | 2.9 | 2.0 | |
| | | 3.0 | 0.06 | 3.1 | 2.9 | |
| | | 4.5 | 0.06 | 3.3 | 3.4 | |

high hardness (1000 HV$_{0.05}$) was not enough). According to the microhardness studies regardless of porosity, the basic structural components were sorbite and troostite.

X-ray analysis showed an increase in lattice parameter with respect to the standard on 0.03–0.06% for all samples. This confirmed the assumption about the carbon saturation of the thin surface layers under friction of iron with limited lubrication.

Thus, boundary friction could result in contact surfaces heating above the temperatures of phase transformations and the carburizing of iron. Similar results for the steels are presented in [73].

As the friction ratio, wear rate is strongly related to pore size. The greatest wear ($P = 4\%$) corresponded to the minimum value of $K_{IC}$. This indicates a relationship between pore size (pore size is greatest when $P = 4\%$), fracture toughness, and wear resistance.

Since the active layer thickness significantly exceeds the thickness of the oxide products of wear and the size and the depth of diffusion penetration of interstitial elements,

physical and mechanical properties of the material have an effect on wear resistance. Currently accepted methodology for assessing the wear rate based on the determination of physical and mechanical properties [63, 74], but have a low accuracy of prediction under lubricated friction [74], are sufficient for engineering calculations.

Linear wear rate can be determined from the expression [59]:

$$I_h = \frac{\sqrt{\nu/4}}{2(\nu + 1)n_{kr}} \cdot \sqrt{h/R_{cv}} \cdot b \cdot \varepsilon^\nu. \tag{30}$$

Regardless of the contact type:

$$\varepsilon = \frac{h}{R_{max}}. \tag{31}$$

The film thickness, Figure 10, under the boundary friction was comparable to the rapprochement between the two surfaces, and therefore elastic contact took place.
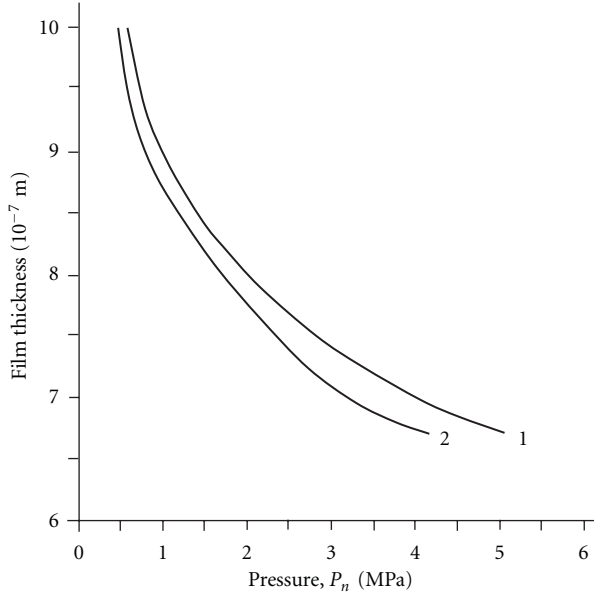
FIGURE 10: Dependence of the thickness $h$ of the oil film on the pressure: $1 - P = 2\%$, $2 - P = 20\%$.

Within the contour area under elastic unsaturated contact, the rapprochement was calculated as [59]:

$$h = \left( \frac{5P_c R^{1/2}(1 - \mu^2)R_{\max}^\nu}{b\nu(\nu - 1)K_1 E} \right)^{2/(2\nu+1)}. \tag{32}$$

The coefficient $K_1 = 0.5$ was determined from nomograms [59]. The relative rapprochement under saturated contact was assessed according to the expression [59]:

$$\varepsilon = \frac{1}{(b\nu)^{1/(\nu-1)}}. \tag{33}$$

In case of elastic unsaturated contact (34) for linear wear rate $I_h$ is got after substitution of (31), (32), (33) in (30).

$$I_h = \frac{\sqrt{\nu/4}}{2(\nu + 1)n_{kr}} \cdot \sqrt{\frac{R_{\max}}{(b\nu)^{1/(\nu-1)} \cdot R_{cv}}} \cdot b \cdot \left( \frac{1}{(b\nu)^{1/(\nu-1)}} \right)^\nu. \tag{34}$$

In case of elastic unsaturated contact, the linear wear rate $I_h$ can be determined on the basis of the formula (35):

$$I_h = \frac{\sqrt{\nu/4}}{2(\nu + 1)n_{kr}} \sqrt{\left[ \frac{5P_c R_{cv}^{1/2}(1 - \mu^2)R_{\max}^\nu}{b\nu(\nu - 1)k_1 E} \right]^{2/2n+1} \frac{1}{R_{cv}}}$$
$$\times b \left( \left[ \frac{5P_c R_{cv}^{1/2}(1 - \mu^2)R_{\max}^\nu}{b\nu(\nu - 1)K_1 E} \right]^{2/2n+1} \frac{1}{R_{\max}} \right)^\nu. \tag{35}$$

The bond between $K_{IC}$, $P_c$, and $l$ was found according to (36):

$$K_{IC} = \frac{(1 - 2\mu)P_c \sqrt{l}}{t_p}. \tag{36}$$

In the case of the elastic unsaturated contact, (35) and (23) were solved simultaneously, and according to (36), (37) was got. In the case of the elastic saturated contact, (34) and (23) were solved simultaneously and according to (36), (38) was got.

The values of $R_{cv}$, $R_{\max}$, $b$, $\nu$ for the porous materials were taken from [59].

In the case of unsaturated elastic contact:

$$I_h = \frac{[P_n(1 - \mu^2)/E]^{0.98} \cdot ((n/2 - 1) \cdot A \cdot (30P_n^{0.565}))^n}{(d/2)^{(1-n/2)} - (0.03K_{IC}/P_n^{0.565})^{(2-n)}}. \tag{37}$$

In the case of saturated elastic contact:

$$I_h = \frac{0.0056(n/2 - 1) \cdot A \cdot (10P_n)^n}{(d/2)^{(1-n/2)} - (0.1K_{IC}/P_n)^{(2-n)}}. \tag{38}$$

The solution was found like (39) because formulas (37) and (38) are different only in exponents $P_c$ and in constant coefficients values, minor changes of $E$ and $\mu$ and $P_c$ and $P_n$ proportionality were also taken into account:

$$I_h = \frac{a_1 \cdot P_n^{n_1}(n/2 - 1)}{(d/2)^{(1-n/2)} - (C3 \cdot K_{IC}/P_n^{n_2})^{(2-n)}}. \tag{39}$$

In the area of $P = 8$–10%, the transition from closed to open porosity occurred, so the experimental data (see Table 5) was approximated separately for $P$ from 2 to 8.6% (numerator) and from 20 to 8.6% (denominator). In the first case, $a_1 = 76.2$, $C3 = 0.03$, $n_1 = 0.66$, $n_2 = 3.77$, and $n = 2.32$; in the second $a_1 = 36.3$, $C3 = 6.5$, $n_1 = 0.086$, $n_2 = 1.37$, and $n = 1.67$.

Note that $n$ varies from 2 to 8 under fatigue fracture, prestrain and impurity content increase caused $n$ increase. Among other factors, the value of $n$ depends on the pressure and cycle asymmetry.

In [73, 75] similar values of $n$ for cold-plastic steel at high cycle asymmetry are represented. Apparently, $m$ changing from 2.32 to 1.67 caused by pores changes. Closed porosity makes it difficult to circulate the oil, and therefore the main influence has reduced the concentration of stress. In case of open porosity, pores provide constant oil circulation and heat dissipation from the friction surfaces, so the value of $n < 2$.

In general, dependence (39) describes the experiment with sufficient accuracy for engineering calculations; the number of undetermined coefficients is much smaller than in techniques used nowadays [63, 74].

The iron powder tribological characteristics study revealed the following patterns of relationship. Under dry friction the friction ratio $f$ and wear rate $I_h$ were changed nonmonotonic with increasing porosity. The reason for the nonmonotonic dependence of $f(P)$ is in pore size and distance between them changes, that determine the deformation in the active area. Depending on the elastic and plastic deformed contacts portion, the type of contact is established, and it determines the friction ratio value, along with the physical and mechanical characteristics of the material. The surface fracture of iron powder at few MPa

pressure is the nature of fatigue. The symbasis of $I_h(P)$ and $K_{IC}(P)$ dependences is determined by the contact surface fracture localization in a small volume, and the material separation occurs only when the critical value of stress concentration is reached.

Limited lubricated friction under the same pressures provides elastic contact and very little shear strength of frictional bond. The surface of the porous iron is saturated with carbon. The porosity of 8–10% (carbonyl iron) provides a transition from the closed to open porosity, which naturally affects the value of the friction ratio and wear rate.

As in the case of dry friction in boundary friction, $f(P)$ and $I_h(P)$ functions are nonmonotonic. With sufficient accuracy for engineering calculations the wear rate under boundary friction can be calculated on the assumption of elastic contact.

The developed model predicted the values of fracture toughness, friction ratio, and integral linear wear rate of porous steel and bronze [74–84].

## 5. Conclusion

Pores' structure changes during the consolidation process, that provides blunting and bend of the crack while moving between pores, is the reason for non-monotonic dependence $K_{IC}(P)$. During the dry sliding and during the boundary friction $f(P)$ и $I_h(P)$ functions are nonmonotonic. Local $f(P)$ and $I_h(P)$ extremum appearance is caused by different reasons (pore sizes and structure penetrability), but is mainly the consequence of pore structure transformation.

## List of Symbols

$K_{IC}$: Fracture toughness, MN/m$^{3/2}$
$K_Q$: Estimated fracture toughness, MN/m$^{3/2}$
$P$: Porosity, %
$\sigma_{0.2}$: Yield strength, MPa
$g$: Crack distribution energy
$T$: Linear crack front tension, N
$E$: Elastic modulus, MPa
$\mu$: Poisson's ratio
$A$: Specific energy of uniform deformation
$\gamma_{eff}$: Effective surface energy of the Griffiths-Orowan theory
$l_d$: Length dimension constant
$\delta_e$: Uniform Deformation, %
$\sigma_B$: Tensile Strength, MPa
$\tau$: Crack movement stress, MPa
$r$: Pore radius, m
   : Interface energy, J/m$^2$
$b_0$: Interatomic distance, m
   : Distance between the inhomogeneities (pores), m
$f$: Friction ratio
$P_n$: Nominal pressure, MPa
$P_c$: Contour pressure, MPa
$f_d$: Friction ratio deformation component

   : Microroughnesses characteristic of a rigid material of the friction pair
HB: Hardness
$f_m$: Molecular component of friction ratio
Ra: Arithmetic mean deviation of profile, m
$\beta$ and $\tau_0$: Friction characteristics
$S_{ost}$: Residual variance
$F$: Fisher criterion
$\tau_m$: Crack movement stress in porous material, MPa
$a$: Coefficient
$G$: Shear modulus, MPa
$B$: Burgers vector, m
$R$: Distance between the pores, m
$b$ and $v$: Bearing surface curve parameters
$\varepsilon$: Relative approach
$t_p$: Relative contact area
$\alpha_1$: The coefficient depending on the type of contact
$C1$: The constant that relates the contour and nominal pressure
$f$: Friction ratio change
$i_h$: Specific linear wear rate
$h$: Rapprochement between the friction surfaces, m
$R_{cv}$: Radius of curvature
$n_{kr}$: Number of cycles, leading to the fracture
$I_h$: Integral linear wear rate
$R_{max}$: The greatest distance between the bumps and hollows within the gauge length
$K$: Stress intensity factor change (Paris formula), MN/m$^{3/2}$
$N$: Number of cycles (Paris formula)
$A$ and $n$: Coefficients (Paris formula)
$K$: Stress intensity factor, MN/m$^{3/2}$
$l$: Crack length, m
$a_r$: Radius of contact area, m
$\sigma_y$: Fracture stress, MPa
$d$: Average pore diameter, m
$\alpha_g$: Coefficient of hysteresis losses under friction
$V_1$ и $V_2$: Counterbodies' velocities, m/s
$V$: Oil dynamic viscosity, m$^2$/kg
$\alpha_p$: Oil piezocoefficient, kg·s/m$^2$
$R_n$: Reduced radius of curvature, m
$K_1$: Coefficient
$C3$: Coefficient.

## References

[1] H. P. Dzhoy, "The past and the future of tribology," *Journal of Friction and Wear*, vol. 11, no. 1, pp. 149–159, 1990 (Russian).

[2] A. A. Kuklin, E. S. Michkova, and V. Y. Bulanov, *Technology and Economics of Powder Metallurgy*, Nauka, Moscow, Russia, 1989.

[3] H. Danninger, C. Gierl, G. Mühlbauer, M. S. Gonzalez, J. Schmidt, and E. Specht, "Thermophysical properties of sintered steels: effect of porosity," *International Journal of Powder Metallurgy*, vol. 47, no. 3, pp. 31–41, 2011.

[4] C. Sohar, A. Betzwar-Kotas, C. Gierl, H. Danninger, and B. Weiss, "Gigacycle fatigue response of tool steels produced by powder metallurgy compared to ingot metallurgy tool steels," *International Journal of Materials Research*, vol. 101, no. 9, pp. 1140–1150, 2010.

[5] M. Dlapka, H. Danninger, C. Gierl, and B. Lindqvist, "Defining the pores in PM components," *Metal Powder Report*, vol. 65, no. 2, pp. 30–33, 2010.

[6] H. Winkelmann, M. Varga, E. Badisch, and H. Danninger, "Wear mechanisms at high temperatures. Part 2: temperature effect on wear mechanisms in the erosion test," *Tribology Letters*, vol. 34, no. 3, pp. 167–175, 2009.

[7] H. Winkelmann, E. Badisch, M. Kirchgaßner, and H. Danninger, "Wear mechanisms at high temperatures. Part 1: wear mechanisms of different Fe-based aAlloys at elevated temperatures," *Tribology Letters*, vol. 34, no. 3, pp. 155–166, 2009.

[8] P. Beiss and S. Lindlohr, "Porosity statistics and fayigue strength," *International Journal of Powder Metallurgy*, vol. 45, no. 2, pp. 39–48, 2009.

[9] P. Beiss and S. Lindlohr, "Correlation between extreme value porosity rating and fatigue strength of sintered steel," *Materialpruefung/Materials Testing*, vol. 50, no. 3, pp. 126–132, 2008.

[10] P. Ganesan, Ş Domşa, and P. Beiss, "Fracture toughness of PM alloy steels," *Powder Metallurgy*, vol. 48, no. 4, pp. 323–328, 2005.

[11] M. Campos, J. Sicre-Artalejo, J. J. Munoz, and J. M. Torralba, "Effect of austempering conditions on the microstructure and tensile properties of low alloyed sintered steel," *Metallurgical and Materials Transactions A*, vol. 41, no. 7, pp. 1847–1854, 2010.

[12] M. Campos, J. M. Torralba, C. Menapace, and A. Molinari, "Effect of copper infiltration on fracture mode in sintered steels," *Powder Metallurgy*, vol. 51, no. 2, pp. 176–181, 2008.

[13] R. Bidulský, M. A. Grande, and J. Bidulská, "Microstructures and fracture investigations of low alloyed vacuum treated sintered steel," *Chemicke Listy*, vol. 105, no. 16, pp. 506–509, 2011.

[14] R. Bidulský, M. A. Grande, and M. Kabátová, "Improved fatigue resistance of sintered steels via local hardening," *Chemicke Listy*, vol. 105, no. 14, pp. 159–162, 2011.

[15] M. Rosso, E. Dudrova, M. Actis Grande, and R. Bidulský, "Wear characteristics of vacuum sintered steels," *Materials Science Forum*, vol. 672, pp. 17–22, 2011.

[16] R. Bidulský, M. A. Grande, J. Bidulská, M. Vlado, and T. Kvačkaj, "Wear mechanism of Chromium Pre-alloyed sintered steel," *High Temperature Materials and Processes*, vol. 28, no. 3, pp. 175–180, 2009.

[17] R. Bidulský, M. A. Grande, J. Bidulská, and T. Kvačkaj, "Wear resistance of chromium pre-alloyed sintered steels," *Materiali in Tehnologije*, vol. 43, no. 6, pp. 303–308, 2009.

[18] E. Dudrova, M. Kabatova, R. Bures, R. Bidulsky, and A. S. Wronski, "Processing, microstructure and properties of 2–4 % Mn and 0.3/0.7 % C sintered steels," *Kovove Materialy*, vol. 43, no. 6, pp. 404–421, 2005.

[19] S. E. Aleksandrov, A. R. Pirumov, and O. V. Chesnikova, "Plastic flow of porous materials in friction contact area," *Powder Metallurgy and Metal Ceramics*, vol. 47, no. 9-10, pp. 512–517, 2008.

[20] A. V. Vdovichenko, Y. N. Podrezov, and V. V. Skorokhod, "Mechanical resonance spectroscopy of interparticle boundaries in high-density iron powder compacts," *Powder Metallurgy and Metal Ceramics*, vol. 47, no. 5-6, pp. 366–372, 2008.

[21] A. S. Drachinskii, A. E. Kushchevskii, A. V. Perepelkin et al., "Effect of porosity on the resistance of P/M iron to cracking," *Soviet Powder Metallurgy and Metal Ceramics*, vol. 21, no. 12, pp. 973–977, 1982.

[22] A. G. Evans and T. G. Langdon, *Structural Ceramics*, Metallurgiya, Moscow, Russia, 1980.

[23] S. N. Platov, V. G. Kudryashov, M. L. Bernstein et al., "On the estimation of parameters of porous materials fracture toughness," *Physicochemical Mechanics of Materials*, no. 5, pp. 20–24, 1974 (Russian).

[24] L. W. Crane and R. J. Farrow, "Effect of sintering conditions on fracture toughness of a commercial alloy steel," *Powder Metallurgy*, vol. 23, no. 5, pp. 198–202, 1980.

[25] G. A. Klarke and R. A. Queeney, "Fracture toughness and density in sintered 316L stainless steel," *The International Journal of Powder Metallurgy*, vol. 8, no. 2, pp. 81–202, 1972.

[26] F. J. Esper, G. Leuze, and C. M. Sonsino, "Characteristic properties of powder metallurgical materials relevant to fatigue design," *Powder Metallurgy International*, vol. 13, no. 4, pp. 203–208, 1981.

[27] A. G. Zherdin, S. A. Firstov, and L. G. Bayonet, "Fracture and ductile-brittle transition in powder materials," *Technological and Structural Plasticity of the Powder Materials*, vol. S, pp. 89–92, 1988 (Russian).

[28] J. T. Barnby, D. C. Ghosh, and K. Dinsdale, "The fracture—resistance of a range of sintered steels," *Powder Metallurgy*, vol. 16, no. 31, pp. 55–71, 1973 (Russian).

[29] N. Ingelstrom and V. Ustimenko, "Influence of porosity and carbon content on the fracture toughness of some sintered steels," *Powder Metallurgy*, vol. 18, no. 36, pp. 303–322, 1975.

[30] N. Ingelstrom and H. Nordberg, "The fracture toughness of flighstrength and highductility sintereel steels," *Scandina an Journal of Metallurgy*, no. 4, pp. 189–192, 1975.

[31] M. Shlesar, A. Parilak, K. Pelikan et al., "Influence of porosity on the mechanical properties of sintered materials," in *Proceedings of the Workshop on the Development and Use of Powder Metallurgy in Engineering*, p. 17, Minsk, Belarus, 1985, Report from the Institute of Experimental Metallurgy.

[32] L. A. Zheltonoga and I. P. Gabrielov, "Characteristics of crack growth in sintered materials," *Soviet Powder Metallurgy and Metal Ceramics*, vol. 18, no. 10, pp. 744–748, 1979.

[33] A. S. Drachinsky, A. V. Krainov, and A. E. Kuschevsky, "The relationship with portion of intergranular fracture of iron powder," *Powder Metallurgy*, no. 1, pp. 43–45, 1985 (Russian).

[34] N. B. Romalis, "Calculation of effective stress intensity factors of structurally inhomogeneous bodies with cracks," *Mechanics of Composite Materials*, vol. 23, no. 3, pp. 287–290, 1987.

[35] G. Prefferborn, "Grundznge der fraktographie von eisenwerkstoffen," *Radex Rundschan*, no. 3, pp. 591–673, 1978.

[36] V. Z. Parton and E. M. Morozov, *The Mechanics of Elastoplastic Fracture*, Nauka, Moscow, Russia, 1974.

[37] Y. L. Krasulin, S. M. Barinov, and V. S. Ivanov, *Structure and Fracture of Materials from Powders of Refractory Compounds*, Nauka, Moscow, Russia, 1985.

[38] A. S. Drachinsky, Y. N. Petrov, and V. I. Trefilov, "The dislocation structure and properties of the propagation of a ductile crack in armco iron," *Ukraine National Magazine*, no. 13, pp. 1538–1542, 1968 (Russian).

[39] V. M. Finkel, *Physical Basis of Fracture Inhibition*, Metallurgiya, Moscow, Russia, 1977.

[40] D. R. Biswas, "Crack-void interaction in polycrystalline alumina," *Journal of Materials Science*, vol. 16, no. 9, pp. 2434–2438, 1981.

[41] F. F. Lang, "The interaction of a crack front with second-phcese dispersion," *Philosophical Magazine*, vol. 23, no. 179, pp. 983–992, 1970.

[42] Y. I. Ragozin and Y. Y. Antonov, "Method of accelerated fracture toughness KIc testing of metallic materials," *Strength of Materials*, vol. 16, no. 2, pp. 179–184, 1984.

[43] V. S. Ivanova, L. R. Batvina, and L. I. Malov, "Prediction of fracture toughness and other mechanical properties, using the similarity criteria," in *Fatigue and Fracture of Metals*, pp. 3–35, Nauka, Moscow, Russia, 1974.

[44] W. Dhal and W. Anton, *Werkstoffkunde Eisen und Stahl*, Verlag Stahleisen mbH, Dusseldorf, Germany, 1983.

[45] S. V. Belov, *Porous Metals in Mechanical Engineering*, Mashinostroenie, Moscow, Russia, 1981.

[46] M. Balshin and S. G. Fedosov, "Contact and the elastic characteristics of copper powder ," *Metals*, no. 1, pp. 166–172, 1965 (Russian).

[47] K. Kreider, Ed., *Composite Materials*, Composites with Metal Matrix, Mashinostroenie, Moscow, Russia, 1978.

[48] R. W. Cahn, *Physical Metallurgy*, North-Holland, Amsterdam, The Netherlands, 1978.

[49] F. F. Lange, "The interaction of a crack front with a second-phase dispersion," *The Philosophical Magazine*, vol. 22, no. 179, pp. 983–992, 1970.

[50] P. S. Theocaris and J. Milios, "Crack arrest modes of a transverse crack going through a longitudinal crack or a hole," *Journal of Engineering Materials and Technology, Transactions of the ASME*, vol. 103, no. 2, pp. 177–182, 1981.

[51] V. N. Antsiferov, "Features of powder material deformation with cyclic loading," *Powder Metallurgy and Metal Ceramics*, vol. 40, no. 11-12, pp. 569–572, 2001.

[52] A. A. Shatsov, "Mechanical properties of porous materials," *Metal Science and Heat Treatment*, vol. 45, no. 11-12, pp. 441–444, 2003.

[53] Y. V. Kolesnikov and E. M. Morozov, *Mechanics of Contact Fracture*, Nauka, Moscow, Russia, 1989.

[54] I. M. Fedorchenko, A. E. Kushchevskii, V. V. Pushkarev, A. S. Drachinskii, A. V. Perepelkin, and Y. N. Podrezov, "Influence of porosity on the tribological properties of iron-base powder metallurgy materials," *Soviet Powder Metallurgy and Metal Ceramics*, vol. 23, no. 5, pp. 394–396, 1984.

[55] A. E. Kushchevskii, V. T. Bondar', N. A. Krylova, T. F. Mozol, and O. M. Romanenko, "An investigation of the structure of powder metallurgy iron with different porosities by scanning electron microscopy," *Soviet Powder Metallurgy and Metal Ceramics*, vol. 29, no. 9, pp. 745–748, 1990.

[56] V. N. Antsiferov, N. N. Maslennikov, A. A. Shatsov, and I. A. Polovnikov, "Determining the carrying capacity of powdered materials under boundary lubrication," *Journal of Friction and Wear*, vol. 12, no. 4, pp. 683–686, 1991 (Russian).

[57] I. I. Berkowitz and D. G. Gromakovsky, *Tribology*, Samara State University, Samara, Russia, 2000.

[58] GOST 23.225-99, "Ensuring durability of products. Methods of durability confirmation. General requirements" (Russian).

[59] I. V. Kragelskii and N. M. Mihin, *Friction Units of Machines*, Mashinostroenie, Moscow, Russia, 1984.

[60] B. A. Drozdovskii and Y. B. Friedman, *The Influence of Cracks on the Mechanical Properties of Structural Steel*, Metallurgizdat, Moscow, Russia, 1960.

[61] V. N. Antsiferov, N. N. Maslennikov, and A. A. Shatsov, "Strength and fracture toughness of powder steels," in *Proceedings of the Universities. Iron and steel industry*, no. 2, pp. 20–22, 1989.

[62] V. N. Antsiferov, N. N. Maslennikov, and A. A. Shatsov, "Effect of porosity on coefficient of friction of iron," *Journal of Friction and Wear*, vol. 13, no. 4, pp. 702–706, 1992 (Russian).

[63] G. Poltser and F. Meisner, *Foundations of Friction and Wear*, Mashinostroenie, Moscow, Russia, 1984.

[64] V. D. Zozulya, V. V. Polotay, I. A. Panfilova, and L. E. Lukin, "Effect of porosity on the plastic deformation of the surface layer at frictionsintered iron," *Journal of Friction and Wear*, vol. 10, no. 2, pp. 289–294, 1989 (Russian).

[65] N. G. Baranov, L. V. Zabolotny, Y. V. Ivashchenko, I. A. Koseko, and G. A. Avtonomov, "Investigation of physico-chemical phenomena that occur when iron powderfriction on ceramic," *Journal of Friction and Wear*, vol. 11, no. 1, pp. 143–148, 1990 (Russian).

[66] A. Vutke, E. A. Marchenko, A. Shiling, H. Reinhold, and D. Stemler, "On the quantitative criteria for structural failure of metals in friction," *Journal of Friction and Wear*, vol. 10, no. 3, pp. 434–441, 1989 (Russian).

[67] Z. G. Pinchuk and E. G. Shiolovskaya, "Relationship microstructural changes with the kinetics of wear of the surface layer of metal in friction," *Journal of Friction and Wear*, vol. 10, no. 6, pp. 965–972, 1989 (Russian).

[68] I. Z. Kragelskii, *Friction and Wear*, Mashinostroenie, Moscow, Russia, 1968.

[69] Y. Y. Meshkov, *Physical Basis of Fracture of Steel Structures*, Naukova Dumka, Kiev, Ukraine, 1981.

[70] V. N. Antsiferov, S. N. Peshcherenko, A. A. Shatsov, and N. N. Maslennikov, "Effect of pores on fracture of iron," *Strength of Materials*, vol. 21, no. 2, pp. 161–164, 1989.

[71] O. N. Romaniv, E. A. Shur, A. N. Tkach, V. N. Simin'kovich, and T. N. Kiseleva, "kinetics and mechanism of fatigue crack growth in iron," *Physico-Chemical Mechanics of Materials*, vol. 17, no. 2, pp. 57–66, 1981 (Russian).

[72] I. V. Kragelskii and V. V. Alisin, Eds., *Friction, Wear and Lubrication*, vol. 2, Mashinostroenie, Moscow, Russia, 1979.

[73] K. M. Fedorchenko and L. I. Pugina, *Composite Sintered Antifriction Materials*, Naukova Dumka, Kiev, Ukraine, 1980.

[74] A. M. Ryakhovskii, "Calculation of wear intensity of construction materials under elastoplastic friction-contact interaction," *Journal of Friction and Wear*, vol. 11, no. 1, pp. 42–48, 1990 (Russian).

[75] L. S. Moroz, *Mechanics and Physics of Deformation and Fracture of Materials*, Mashinostroenie, Moscow, Russia, 1984.

[76] V. N. Antsiferov, N. N. Maslennikov, and A. A. Shatsov, "Strength and fracture toughness of powder steels," in *Proceedings of the Universities. Iron and Steel*, no. 3, pp. 124–129, 1989.

[77] V. N. Antsiferov, N. N. Maslennikov, A. A. Shatsov, and V. B. Platonova, "Effect of heat treatment on the crack resistance of powder steel SP50Kh3NM," *Metal Science and Heat Treatment*, vol. 33, no. 8, pp. 617–620, 1991.

[78] V. N. Antsiferov, N. N. Maslennikov, and A. A. Shatsov, "Now to determine friction coefficients of sintered steels?" *Journal of Friction and Wear*, vol. 14, no. 6, pp. 1082–1086, 1993 (Russian).

[79] V. N. Antsiferov, N. N. Maslennikov, and A. A. Shatsov, "Friction wearing powder steels without additional feeding lubricant," *Journal of Friction and Wear*, vol. 15, no. 6, pp. 1022–1027, 1994 (Russian).

[80] V. N. Antsiferov and A. A. Shatsov, "Friction and wear of powder steels under lubricant limited supply conditions," *Journal of Friction and Wear*, vol. 16, no. 2, pp. 315–322, 1995 (Russian).

[81] V. N. Antsiferov and A. A. Shatsov, "Friction and wear of powder aluminum bronze of optimal composition," *Journal of Friction and Wear*, vol. 17, no. 2, pp. 56–60, 1996.

[82] V. N. Antsiferov, T. V. Smyshlyaeva, and A. A. Shatsov, "Self-lubricating copper-based pseudoalloy for antifriction and constructional products," *Journal of Friction and Wear*, vol. 17, no. 4, pp. 497–502, 1996 (Russian).

[83] A. A. Shatsov, "Tribological characteristics of powder steels under boundary friction," *Advanced Materials*, no. 2, pp. 69–73, 2001 (Russian).

[84] A. A. Shatsov, "Prediction of tribological characteristics of powder steels under dry friction," *Advanced Materials*, no. 5, pp. 71–77, 2000.

*Research Article*

# Characterization of Tool Wear in High-Speed Milling of Hardened Powder Metallurgical Steels

**Fritz Klocke, Kristian Arntz, Gustavo Francisco Cabral, Martin Stolorz, and Marc Busch**

*Fraunhofer Institute for Production Technology IPT, Steinbachstraße 17, 52074 Aachen, Germany*

Correspondence should be addressed to Marc Busch, marc.busch@ipt.fraunhofer.de

In this experimental study, the cutting performance of ball-end mills in high-speed dry-hard milling of powder metallurgical steels was investigated. The cutting performance of the milling tools was mainly evaluated in terms of cutting length, tool wear, and cutting forces. Two different types of hardened steels were machined, the cold working steel HS 4-2-4 PM (K490 Microclean/66 HRC) and the high speed steel HS 6-5-3 PM (S790 Microclean/64 HRC). The milling tests were performed at effective cutting speeds of 225, 300, and 400 m/min with a four fluted solid carbide ball-end mill ($D_0 = 6$, TiAlN coating). It was observed that by means of analytically optimised chipping parameters and increased cutting speed, the tool life can be drastically enhanced. Further, in machining the harder material HS 4-2-4 PM, the tool life is up to three times in regard to the less harder material HS 6-5-3 PM. Thus, it can be assumed that not only the hardness of the material to be machined plays a vital role for the high-speed dry-hard cutting performance, but also the microstructure and thermal characteristics of the investigated powder metallurgical steels in their hardened state.

## 1. Introduction and Motivation

*1.1. Applications.* In the economically efficient large batch production of complex functional and structural components, the moulding and forming technologies are of crucial importance. The performance of these technologies is significantly defined by the material, the surface conditions, and the subsurface integrity of the manufactured tools, dies, and moulds. Conventional tool steels are increasingly reaching their limits and, therefore, restrain a further development in the large-scale production techniques, considering higher economic efficiency and process stability. Alternatively, high-performance materials like powder metallurgically produced steels [1] can be applied. Compared to conventionally produced tool steels, they verifiably reach a multiplicatively enhanced life of the manufactured tools, dies, and moulds. However, the machining of these superhard steels by multiaxis milling represents a major challenge and is, therefore, an issue of highest interest, both for the scientific research and the industrial production [2–5]. Due to their sophisticated material properties, such as their high hardness, ductility, and pressure strength [4], they can be loaded up to high

mechanical stresses. This represents a central requirement for high-value parts and components, as they occur in different areas of application in the tool and die making; see Figure 1.

Due to its efficiency, flexibility, and precision, the complete machining by means of hard milling is one of the key technologies in the tool, die, and mould-making industry. For instance, 5-axis milling enables the manufacture of high-value parts of highest complexity in one clamping, providing parts and components of excellent surface quality and hence increasing the potential of substituting grinding processes which are often downstreamed to milling. The downside to the geometric flexibility of multiaxis hard milling are the continuously changing chipping conditions, resulting in favourable and unfavourable engagement conditions between the workpiece and the milling tool. In general, second lead to increased loads on the milling tool and hence to reduced tool life time accompanied by a surface damage as well as by a formation of microcracks and structural changes to the subsurface area of the manufactured parts.

However, even along with the highest material requirements and most complex geometries, the simultaneous 5-axis hard milling enables optimal process conditions in
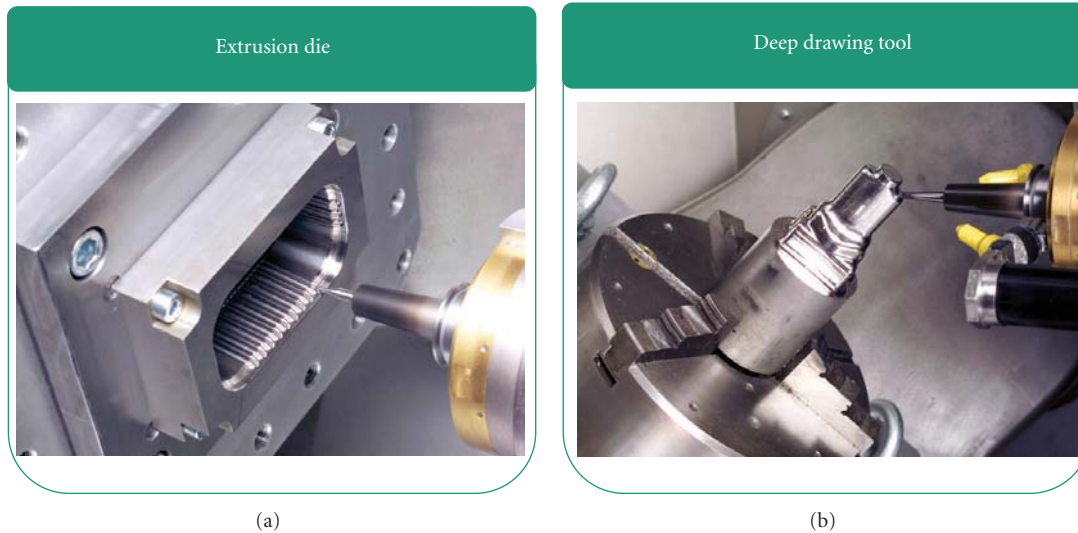
(a)

(b)

FIGURE 1: Tool and die making as a representative area of application for 5-axis-milling of superhard steels; (a) Heading tool; (b) Deep drawing tool.

a narrow process tolerance field by a suitable parameter selection and innovative machining strategies. Currently, the state of knowledge on the suitable selection of optimal component- and production-orientated process parameters for the simultaneous 5-axis hard milling of the addressed materials is limited. Therefore, a reliable and efficient production of highly stressed tools, dies, and moulds is not granted, and the potential of high-performance materials is rarely exploited [6].

*1.2. Metallurgical Fundamentals.* Powder metallurgical (PM) compounded steels, mainly applied in the tool and die making, allow the generation of a homogeneous and isotropic material microstructure. They are characterized by a high hardness, ductility, and pressure strength and possess a good dimensional stability during their heat treatment. Depending on the specific alloy composition and the heat treatment, the hardness can be varied between 50 and 70 HRC. The high hardness of these materials can be reached by carbide precipitation and martensitic transformation [4]. Precipitation hardening, for instance, leads to an improvement of the stability of the workpieces under static and especially pulsatory loads. This leads to a considerably enhanced property profile compared to conventional die materials. Hence, the lifetime of forming tools can be improved drastically.

Furthermore, powder metallurgical steels can be customized referring to the specific area of application with regard to their hardness, heat, and wear resistance or ductility. For instance, the method of spray-compacting permits the adjustment of an extreme wear resistant microstructure due to the high amount of embedded carbides [7–9].

*1.3. High-Speed Milling of Superhard Materials.* A recently conducted survey of the Fraunhofer IPT exhibits that high-speed milling of superhard steels will probably develop from

a core-technology to the most important technology in the area of tool and die making. The reason for this is the combination of highest productivity and flexibility compared to other competing production techniques. However, regarding to small diameters of milling tools as well as superhard materials, there still exists a great demand for further process optimization in order to realize long tool endurances, short lead times and short time-to-markets.

Inter alia, in milling of superhard steels, the occurring forces in the chipping zone are substantially influenced by three circumstances:

(i) the hardness and microstructure of the material to be machined [4, 10],

(ii) the geometry of the uncut chip [11],

(iii) the process parameter [12, 13].

The microstructure leads to the fact that during milling, the rake and the clearance face of the tools are loaded with high abrasive wear due to the fine-particle distributed carbides. Furthermore, hard milling of PM steels tends to the formation of build up edges (BUE). BUE develop if parts of the machined material are cemented at the tools' cutting edge. Here, they form a superhard layer due to the material characteristics and take over the function of the cutting edge. According to the cutting conditions, small particles of the BUE are separated and slide away between the clearance and cutting area. As a consequence, the flank wear increases dramatically, and the surface properties of the machined parts are deteriorated significantly [14].

Furthermore, Kochy et al. and Okada et al. assume that along with an increasing material hardness, the wear of the milling tool increases significantly and that the microstructure of the component material also has a great impact on the progressive wear behaviour of the milling tool [15, 16].

The geometry of the uncut chip is mainly represented by the local thickness of the chip to be removed $h_{sp}$ and the related cross-section of the chip $A_{sp}$. The cross-section represents the amount of material in front of the cutting edge.

Hence, a vital issue for process design is to adapt the uncut chip geometry according to the material properties and the specific machining task. For exemplification, according to the microstructure of the material to be machined, different process parameters resulting in different uncut chip geometries offer optimized process performance. In case of the dimension and distribution of the embedded carbides, higher cutting depths may result in lower tool wear due to the fact that the carbides are unhinged out of the metal matrix in one part and do not have to be cut within several tool engagements.

Salomon already postulated a first hypothesis, stating that an increasing cutting speed reduces the cutting forces and the wear of the milling tool as well as explicitly enhances the flow behaviour and deformation rate of the material to be processed [13]. In order to prove these chipping mechanisms, the complex interactions between the deformation rate, the elevated process temperature, the strength properties and the microscopic flow behaviour and the structural integrity of the material in the local contact zone between the work piece and the milling tool have to be taken into consideration [17, 18]. In a milling process of different machine materials, the progressive wear of the milling tool [16, 19, 20], the elevated process temperature [20, 21] and the roughness of the generated surface increase proportionally with an increasing cutting speed [19]. According to [12], the wear of the milling tool spreads with the highest effective cutting speed, starting at the engagement point of the cutting edge, and can be reduced by an adequate increase of the feed per tooth. If the feed per tooth and the cutting speed in the hard milling process fall below a critical value, the tool vibrations increase, and the tool wear grows significantly [12].

Because of the clearly increased mechanical and especially thermal load in the contact area between the work piece and the milling tool, the continuum mechanical processes on the components surface and subsurface area, that are induced by the HSC-hard milling process, need to be systematically examined and made uniquely describable. This includes in particular the associated softening of the structure [22] and the rehardening [23] as well as the controlled introduction of compressive and tensile residual stress and the avoidance of thermal damages in the form of so-called "white layers" [23].

*1.4. Objectives and Challenges for Process Layout.* As shown above, presently, the procedures and interdependencies of work piece material and process parameter during the chip formation process of powder metallurgical compounded tool materials is only known partially. In this connection, a major issue beside the material analysis is the detailed investigation of the influence of the resulting chip geometry regarding different process parameters, as they are of vital importance for the process performance of high-performing
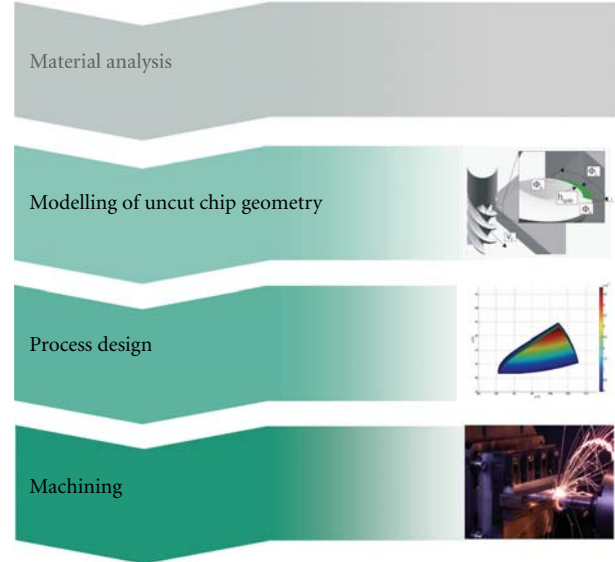


FIGURE 2: Approach for optimizing milling process design on base of modelling the uncut chip geometry.

milling processes like 5-axis-high-speed cutting. On this base, milling process design can be optimized without time- and cost-consuming trial-and-error tests before machining; see Figure 2.

Referring to this, the paper in hand focuses on the issues modelling, process design, and machining. An approach will be presented, enabling an optimization of process design on basis of a theoretical analysis of the uncut chip geometry. In machining tests, the wear mechanisms in milling superhard powder metallurgical alloys will be investigated and linked to the uncut chip geometry.

## 2. Experimental Method

*2.1. Experimental Conditions and Work Piece Materials.* In this experimental study, the applied milling tool was a commercial solid carbide ball-end mill (Table 1). The tool had a nominal diameter of 6 mm and four flutes. Two flutes coincided in the centre tool tip point (axial immersion angle $\kappa = 0°$), and the other two flutes had notches between $\kappa = 0° - 30°$. The helix angle was 30° and the angle of rake $\gamma$ was $-10°$. The concentricity tolerance of the tool was less than $\pm 7\,\mu m$. The tool was coated with TiAlN. The milling tests were carried out at a variation of the effective cutting speed $v_{c,eff} = 225$, 300, and 400 m/min. The tool was constantly tilted by a fixed tilt angle $\beta_{fn} = 75°$, value chosen after performing an analytical simulation of the chip geometry. This tool orientation provides a high effective cutting speed in the surface generating area and a moderate distribution of the chip cross-sectional surface along the cutting edge. At the same time, it avoids cutting with the centre tool tip and provides a moderate chip length distribution, resulting in less tool wear. The feed per tooth was set to $f_z = 0.05$ mm, the radial depth of cut $a_{en}$ was set to 0.05 mm, and the axial depth $a_{pn}$ of cut was set to 0.04 mm. For investigating the influence of the feed per tooth $f_z$ in terms of tool

TABLE 1: Experimental conditions.

| Cutting tool | |
|---|---|
| Design of cutting tool | Solid carbide ball-end mill |
| Tool diameter $d$ (mm) | 6 mm |
| Flute (s) | 4 |
| Helix angle $\lambda$ (°) | 30 |
| Angle of rake $\gamma$ (°) | −10 |
| Coating | TiAlN |
| Cutting parameters | |
| Effective cutting speed $v_{c,\text{eff}}$ (m/min) | 225, 300 and 400 |
| Effective tool diameter $d_{\text{eff}}$ (mm) | 5.796 |
| Feed per tooth $f_z$ (mm/touth) | 0.05 |
| Radial depth of cut $R_d$ (mm) | 0.05 |
| Axial depth of cut $A_d$ (mm) | 0.04 |
| Tilt angle $\beta_{\text{fn}}$ (°) | 75 |
| Overhang of the tool (mm) | 25 |
| Cutting style | down-cutting |
| Lubricant | dry |
| Machine tool | Mikromat 8 V HSC |
| Maximum spindle speed $N$ (min$^{-1}$) | 24000 |
| Spindle power $P$ (kW) | 27 |
| Speed of axis $v_{f\,x,y,z}$ (m/min) | 24 |
| Acceleration of axis $a_{x,y,z}$ (m/s2) | 4 |
| Positioning accuracy $P_a/2$ (mm) | 0.001 |
| Control system | Andronic 400 |
| Drive | Ball screw spindles |

life and progressive tool wear on a random basis, $f_z$ was varied additionally in 0.025 mm/tooth and 0.075 mm/tooth for milling tests at $v_{c,\text{eff}}$ = 300 m/min and for both addressed work piece materials. The overhang of the tool was 25 mm, while shrinking fit chucks were applied. All milling tests were performed in downmilling without any lubricants at dry conditions using a Mikromat 8 V HSC hard milling machine tool. To achieve a representative value for the measurand at each operating point, the root sum square was calculated.

Two kinds of powder metallurgical produced steels were used as typical work piece materials for the tool and die making from Böhler, a high-speed steel HS 6-5-3 PM, which was hardened up to 64 HRC, and a cold working steel HS 4-2-4 PM with a hardness of 66 HRC.

*2.2. Measurement of Machining Forces and Tool Life Time.* The tool wear was measured as the width of the tool flank wear land VB ($\mu$m) with a toolmaker's microscope from Heidenhain (type LS 3003). In case of the high-speed steel HS 6-5-3 PM, respectively, the cold working steel HS 4-2-4 PM, the width of tool wear land was measured iteratively after completing 15 m/20 m in length of cut. The maximum tool life in terms of total length of cut $L_{c,\text{max}}$ was measured after an abort criterion of 75 $\mu$m of tool flank wear land. The morphology of the functional surface on each tooth of the worn milling tools was characterized using a scanning electron microscope (SEM) (Table 2).

The cutting forces were recorded by a Kistler dynamometer (type 9255 A). For characterising the roughness of the generated surface on a random basis, $R_a$ was measured after performing of milling tests with a fresh tool at $v_{c,\text{eff}}$ = 400 m/min and $f_z$ = 0.05 m on both work piece materials with a Tailor-Hobson surface detector.

## 3. Theoretical Analysis of the Chip Geometry

*3.1. Fundamentals of Modelling 5-Axis Ball-End Milling Operations.* Knowing the engagement conditions and the chip geometry is the basis for understanding the milling process. It allows the prediction of the process forces and temperature, tool wear, surface quality, form error, and other phenomena related to the milling process.

The main challenge in modelling ball-end milling operations is building a model that is sufficiently accurate and flexible enough to allow the simulation of different tool geometries and engagement conditions, especially in the machining of parts with sculptured surfaces, whereby the contact conditions and the tool orientation often vary widely.

Previous researches [24–31] indicate analytical models as an adequate compromise solution. In this paper, it was thus used an analytical model for describing the chip geometry and the tool engagement condition.

The main purpose of the presented method is to describe the actual chip geometry and to derive characteristic values for identifying favourable cutting conditions. Therefore, the presented model serves as a support tool for selecting optimized cutting parameters.

*3.1.1. Ball-End Mill Geometry.* The geometry of a ball-end mill is shown in Figure 3. The current cutter angle $\tau_i$, $\kappa_l$ off the cutter $i$ in the axial immersion $\kappa$ and in the rotation angle $\Phi$ is given by

$$\tau_{i,\kappa_l} = \Phi + \Delta\tau \cdot (i-1) - \int_0^{\kappa_l} \frac{R_0 \cdot \tan(\lambda_l)}{2\pi \cdot R_0 \cdot \sin(\kappa)} d\kappa,$$

$$\text{with} : i \in [0,n], \tag{1}$$

where $\Delta\tau$ is the angle between two consecutive cutting edges

$$\Delta\tau = \frac{2\pi}{n}. \tag{2}$$

The local helix angle $\lambda_l$ can be calculated according to Lazoglu and Liang [28] and Zhu et al. [29], who modelled a variable helix angle along the cutting flute. Figure 4 shows the variation of $\lambda_l$ with the axial immersion angle $\kappa$ for the milling tool used in the experiments, which has a helix angle of 30° in the shaft part of the tool.

The contact area for finishing processes is very small, resulting in a small variation of the local helix angle. For the simulated contact conditions, the helix angle varies from 18.5° to 23.5°. For practical purposes, it was considered constant $\lambda_l = 21°$.

*3.1.2. Contact Conditions.* Figure 6 shows the contact conditions for ball-end milling. The reference system FCN is

TABLE 2: Work piece materials.

| Powder metallurgical steels | | |
|---|---|---|
| Term | Cold work steel HS 4-2-4 PM | High-speed steel 6-5-3 PM |
| Hardness (HRC) | 66 | 64 |
| Binder | C Cr Mo V W | C Si Mn Cr Mo V W |
| Modulus of elasticity $E$ (GPa) | 223 | 230 |
| Density $\rho$ (kg/dm³) | 7.79 | 8.0 |
| Thermal conductivity $k$ (W/mk) | 19.6 | 24.0 |
| Thermal expansion coefficient $\alpha$ ($10^{-6}$/K) (at 100/200/300/600°C) | 10.6/11.1/11.6/12.6 | 11.5/11.7/12.2/13.0 |
| Specific heat capacity $c$ (W/mK) | 450 | 420 |
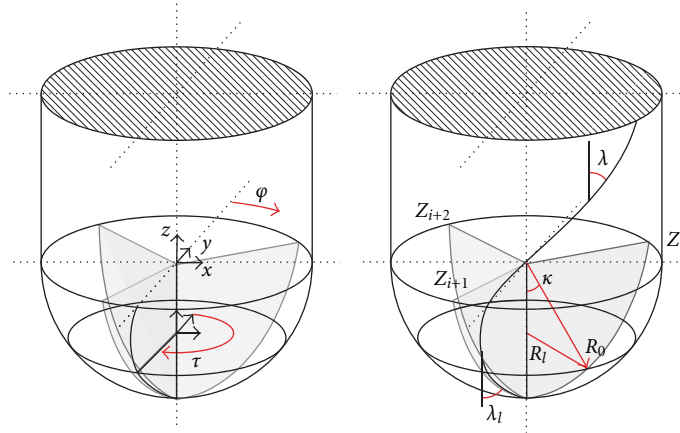


FIGURE 3: Geometry of a ball-end mill.
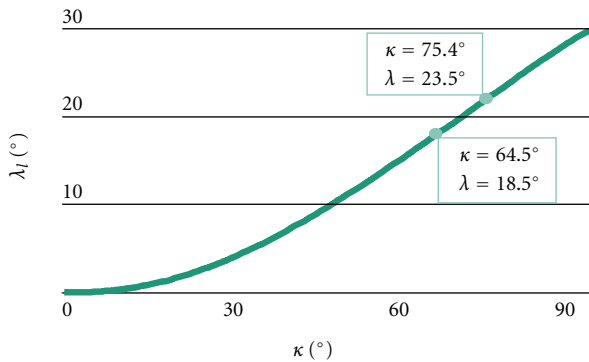


FIGURE 4: Variation of the local helix angle $\lambda_l$ with the axial immersion angle $\kappa$.

defined according to Ozturk and Budak [30]. $F$ is the feed axis, $N$ the surface normal axis, and $C$ the cross-feed axis. $a_{en}$ is the row width, and $a_{pn}$ is the cutting depth. C+ indicates that the next row is towards the positive side of the $C$-axis, and C− is the opposite case; that is, the next row is in the negative direction of the $C$-axis. $f_z$ is the feed per tooth.

*3.1.3. Simulation Approach.* The simulation workflow is shown in Figure 5. First, it is necessary to specify the simulation input, which are the process parameters $a_{pn}, a_{en}, f_z$, C+/C−, the tool orientation and the cutting speed $v_c$. It was used a discrete model for the simulation, so the discretization

parameters, that is, the $\Phi$ and $\kappa$ angle increments, are also inputs for the simulation.

A similar approach was also used by Urban [31] and Ozturk and Budak [30]. Urban implemented a model which takes into consideration the scallops in the feed direction but does not consider the helix angle. Ozturk calculated the boundary curves without considering the scallops and considered just the area 3 in the modelling (see Figure 8), which can result in an error of up to 40% in the resulting contact angle for finishing processes, since the areas 2 and 3 are relative larger for small values of $a_{pn}$ and $a_{en}$.

Secondly, the boundary curves are calculated, defining the position of the uncut chip in the FCN coordinate system. On the basis of the chip spatial position information and on the input parameters, the detailed uncut chip geometry is determined. The geometry is used for deriving other parameters, for example, chip volume, chipping time, effective cutting speed, impact ratio, and surface generating area, which are used for evaluating the previously settled engagement conditions. Finally, the calculated values are plotted and visualized with a dedicated tool implemented in Matlab (Figure 7).

*3.1.4. Calculation of the Boundary Curves.* The typical chip form for ball-end milling, for the positive cross-axis case C+, is depicted in Figure 8. This model was obtained by using a CSG model (constructive solid geometry) in the commercial CAD software Siemens NX. This approach is
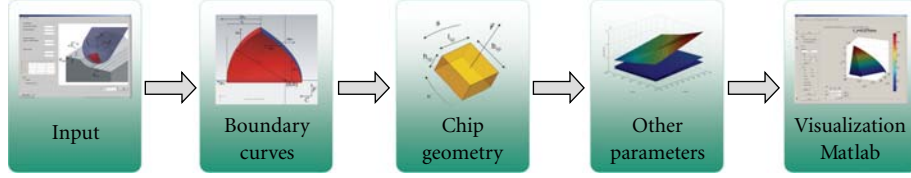
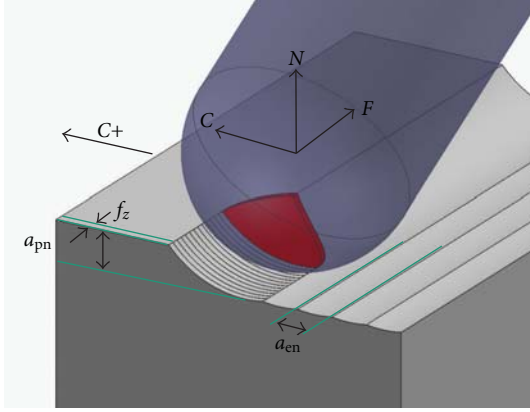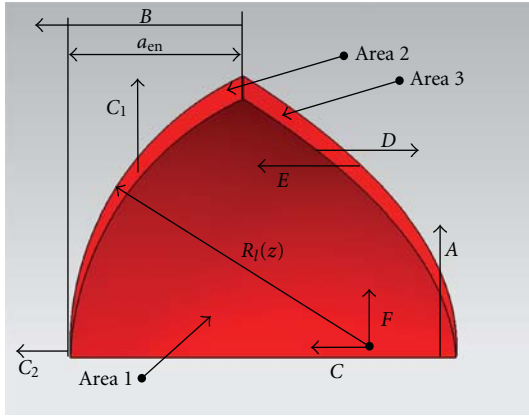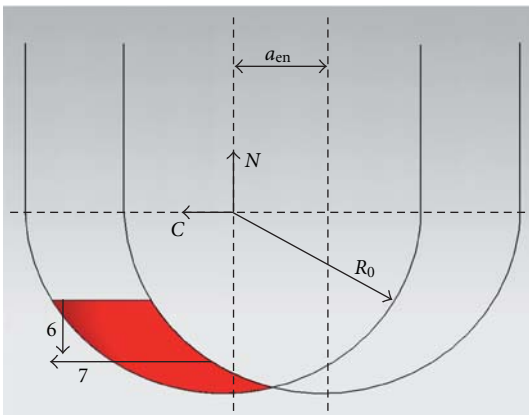Figure 5: Simulation workflow.



Figure 6: Contact conditions and reference system for ball-end milling.



(a)



(b)

Figure 7: Definition of the boundary curves for the case C+.

valid based on the assumption that the previous tool path is the intersection of a rectangular solid work piece and a cylinder along the $F$-axis, not considering the scallops in the feed direction. The scallops in the cross-feed direction are, however, considered. The chip form is, thus, the result of the consecutive subtraction of the resulting geometry and a sphere.

The tooth trajectory is considered circular, which is a very good approximation for finishing processes, since small feed-rate values in comparison to the tool radius are normally used. It is important to note, furthermore, that the error resulting from this assumption increases when the contact area gets closer to the tool tip, since the local radius decreases and the actual path of the local cutting edge differs more from a circular path.

The indicated boundary curves for the positive cross-axis case are calculated as follows:

$$A := F \geq -\frac{f_z}{2},$$

$$B := C \geq R_l - a_{en},$$

$$C_{1,2} := \begin{cases} C_1 := F \geq \sqrt{R_l^2 - C^2} - f_z, & \text{if } F \geq 0, \\ C_2 := C \geq \sqrt{R_l^2 - (F + f_z)^2}, & \text{else } (F \leq 0), \end{cases}$$

$$D := \begin{cases} F \geq -\dfrac{f_z}{2}, & C \leq R_l - a_e, \\ C \leq -\dfrac{a_{en}}{2} + \dfrac{F^2}{2a_{en}} + \dfrac{f_z}{a_{en}}F + \dfrac{f_z^2}{2a_{en}}, \end{cases}$$

$$E := \begin{cases} F \geq -\dfrac{f_z}{2}, & C \leq R_l - a_{en}, \\ C \geq \dfrac{F^2}{2a_{en}} - \dfrac{a_{en}}{2}, \end{cases}$$

$$F := C \geq \sqrt{R_0^2 - N^2} - a_{en},$$

$$G := N \leq a_{pn} - R_0.$$

(3)

The results of the calculation of the boundary curves for the cases C+ and C− are resumed in Table 3.

*3.1.5. Calculation of the Uncut Chip Geometry and Other Parameters.* The main parameters used for describing the chip geometry are the chip thickness ($h_{sp}$), chip width ($b_{sp}$), chip cross-sectional area ($A_{sp}$), and chip length ($l_{sp}$). The chip geometry parameters are described in Figure 8. The uncut chip is discretized in the $\Phi$ and $\kappa$ directions. The chip thickness is defined as the thickness of the material that is

Table 3: Boundary curves for the case C+.

| Case | Area | Condition | |
|---|---|---|---|
| | | $F$ | $C$ |
| C+ | | $F \geq 0,$ $F \geq \sqrt{R_l^2 - C^2} - f_z$ | $C \geq R_{l^-} a_{\mathrm{en}}, C \geq \sqrt{R_l^2 - (F + f_z)^2}$ |
| | | $-\dfrac{f_z}{2} \leq F \leq 0$ | $C \geq \sqrt{R_l^2 - (F + f_z)^2},$ $C \geq \sqrt{R_0^2 - N^2} - a_{\mathrm{en}}, C \geq R_l - a_{\mathrm{en}}$ |
| | | $F \geq -\dfrac{f_z}{2}$ | $C \leq R_l - a_{\mathrm{en}}, C \geq \sqrt{R_0^2 - N^2} - a_{\mathrm{en}},$ $\dfrac{F^2}{2a_{\mathrm{en}}} - \dfrac{a_{\mathrm{en}}}{2} \leq C \leq -\dfrac{a_{\mathrm{en}}}{2} + \dfrac{F^2}{2a_{\mathrm{en}}} + \dfrac{f_z}{a_{\mathrm{en}}}F + \dfrac{f_z^2}{2a_{\mathrm{en}}}$ |
| | | $F \geq -\dfrac{f_z}{2}$ $F \leq \sqrt{R_l^2 - C^2} - f_z$ $F \geq -\dfrac{f_z}{2}$ | $R_l - a_{\mathrm{en}} \leq C \leq \sqrt{R_l^2 - (F + f_z)^2},$ $C \geq \sqrt{R_0^2 - N^2} - a_{\mathrm{en}}$ $-\dfrac{a_{\mathrm{en}}}{2} + \dfrac{F^2}{2a_{\mathrm{en}}} + \dfrac{f_z}{a_{\mathrm{en}}}F + \dfrac{f_z^2}{2a_{\mathrm{en}}} \leq C \leq R_l - a_{\mathrm{en}}$ |
| C− | | $F \geq 0,$ $F \geq \sqrt{R_l^2 - C^2} - f_z$ | $C \leq a_{\mathrm{en}} - R_l, C \leq a_{\mathrm{en}} - \sqrt{R_0^2 - N^2}$ |
| | | $-\dfrac{f_z}{2} \leq F \leq 0$ | $C \leq -\sqrt{R_l^2 - (F + f_z)^2},$ $C \leq a_{\mathrm{en}} - \sqrt{R_0^2 - N^2}, C \leq a_{\mathrm{en}} - r_n$ |
| | | $F \geq -\dfrac{f_z}{2}$ | $C \geq a_{\mathrm{en}} - R_l, C \leq a_{\mathrm{en}} - \sqrt{R_0^2 - N^2},$ $\dfrac{a_{\mathrm{en}}}{2} - \dfrac{F^2}{2a_{\mathrm{en}}} - \dfrac{f_z}{a_{\mathrm{en}}}F - \dfrac{f_z^2}{2a_{\mathrm{en}}} \leq C \leq \dfrac{a_{\mathrm{en}}}{2} - \dfrac{F^2}{2a_{\mathrm{en}}}$ |
| | | $F \geq -\dfrac{f_z}{2}$ $F \leq \sqrt{R_l^2 - C^2} - f_z$ $F \geq -\dfrac{f_z}{2}$ | $-\sqrt{R_l^2 - (F + f_z)^2} \leq C \leq a_{\mathrm{en}} - R_l,$ $C \leq a_{\mathrm{en}} - \sqrt{R_0^2 - N^2}$ $a_{\mathrm{en}} - R_l \leq C \leq \dfrac{a_{\mathrm{en}}}{2} - \dfrac{F^2}{2a_{\mathrm{en}}} - \dfrac{f_z}{a_{\mathrm{en}}}F - \dfrac{f_z^2}{2a_{\mathrm{en}}}$ |
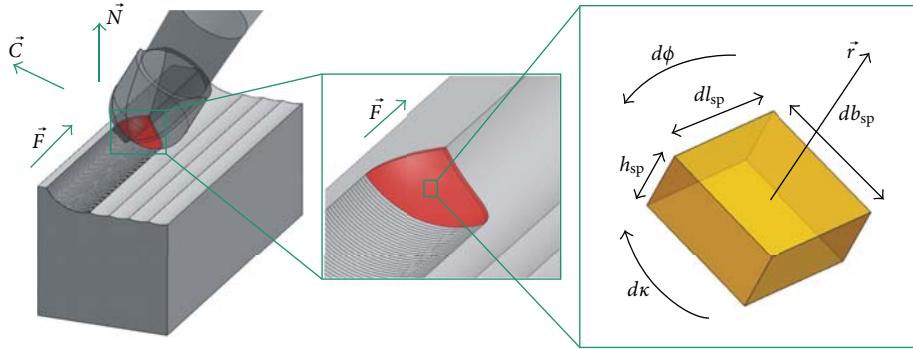


Figure 8: Uncut chip geometry.

removed in a certain cutting point $(\Phi, \kappa)$ of the tool in the normal direction of the cutting edge, that is, in the radial direction of the sphere. It can be approximated by the feed component in the radial direction, that is, the scalar product between the feed vector $\vec{F} = f_z \cdot \vec{f}$ and the sphere radial unity vector outward the surface $\vec{r}$ at a given cutting point [30]

$$h_{\mathrm{sp}}(\Phi, \kappa) = f_z \cdot \vec{f} \cdot \vec{r}(\Phi, \kappa). \qquad (4)$$

$f_z = 0.025\,\text{mm}$       $f_z = 0.050\,\text{mm}$       $f_z = 0.075\,\text{mm}$

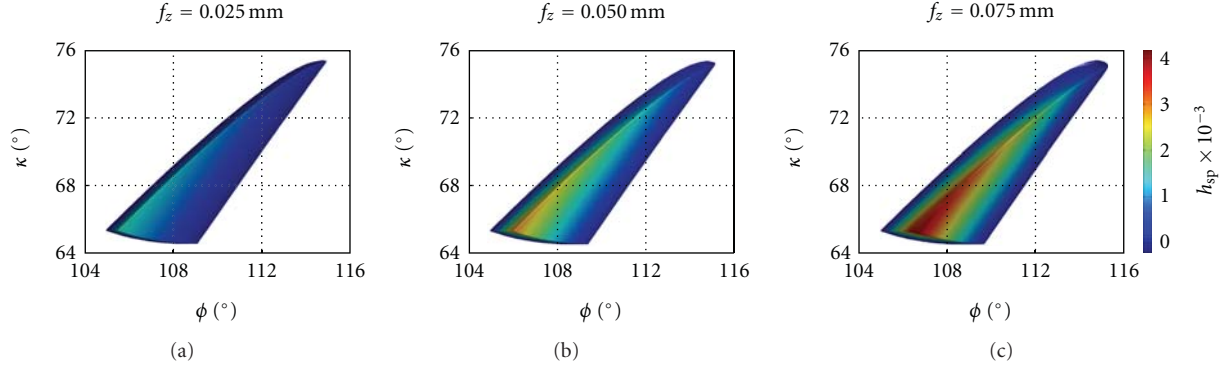(a)                                (b)                                (c)

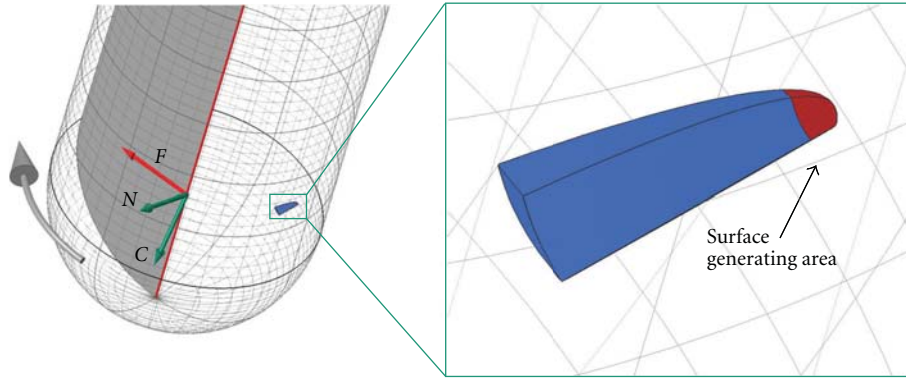Figure 9: Influence of the feed-rate on the contact diagram.



Figure 10: Chip position on ball-end mill for the simulation parameters.

The chip width is calculated along the $\kappa$ direction of the cutting tool and represents the actual contact width of the cutting edge and is given by

$$db_{\text{sp}}(\kappa) = \frac{R_0}{\cos(\lambda_l(\kappa))}d\kappa$$
$$\implies b_{\text{sp}}(\Phi) = \int_{\kappa_s(\Phi)}^{\kappa_e(\Phi)} \frac{R_0}{\cos(\lambda_l(\kappa))}d\kappa,$$

(5)

where $\kappa_s$ and $\kappa_e$ are, respectively, the starting and ending axial immersion angle $\kappa$ for a given rotation angle $\Phi$.

The chip cross-sectional represents the contact area on each cutting edge for each rotation angle and for each and can be calculated as follows:

$$dA_{\text{sp}}(\Phi,\kappa) = h_{\text{sp}}(\Phi,\kappa) \cdot db_{\text{sp}}(\Phi)$$
$$\implies A_{\text{sp}}(\Phi) = \int_{\kappa_s(\Phi)}^{\kappa_e(\Phi)} h_{\text{sp}}(\Phi,\kappa) \cdot \frac{R_0}{\cos(\lambda_l(\kappa))}d\kappa.$$

(6)

The chip length is defined as the contact length for a constant axial tool immersion, that is, the engagement length of each tool slice

$$dl_{sp}(\kappa) = R_l(\kappa) \cdot d\Phi \implies l_{\text{sp}}(\kappa) = \int_{\Phi_s(\kappa)}^{\Phi_e(\kappa)} R_l(\kappa)d\Phi, \qquad (7)$$

where the chip volume is the volume removed by one flute in one tool revolution

$$dV_{\text{sp}}(\Phi,\kappa) = h_{\text{sp}}(\Phi,\kappa) \cdot db_{\text{sp}}(\kappa) \cdot dl_{sp}$$
$$\implies V_{\text{sp}} = \int_{\kappa_{\text{sg}}}^{\kappa_{\text{eg}}} \int_{\Phi_{\text{sg}}}^{\Phi_{\text{eg}}} h_{\text{sp}}(\Phi,\kappa) \cdot \frac{R_0}{\cos(\lambda_l(\kappa))} R_l(\kappa)d\Phi\, d\kappa,$$

(8)

where $\kappa_{\text{sg}}$, $\kappa_{\text{eg}}$ are, respectively, the global starting and ending axial immersion angle and $\Phi_{\text{sg}}$, $\Phi_{\text{eg}}$ are the global starting and ending rotation angle. For the points outside the boundary conditions, $h_{\text{sp}}(\Phi,\kappa) = 0$.

*3.2. Simulation Results.* Table 4 resumes the input data for the simulation: the cutting speed varies along the tool axis, due to the variation of the local tool radius $R_l$. The closer to the tool tip the smaller the cutting speed and vice versa. The effective cutting speed was calculated on the surface generating area of the chip, which is the area where the actual cut generates a final surface which is not recut in the following tool engagement.

The chip position on the tool and the FCN coordinate system are shown in Figure 10. The position and orientation of the chip varies according to the tool orientation and cutting parameters. It should be noticed that for the simulation parameters, the surface generating area is on the top part of
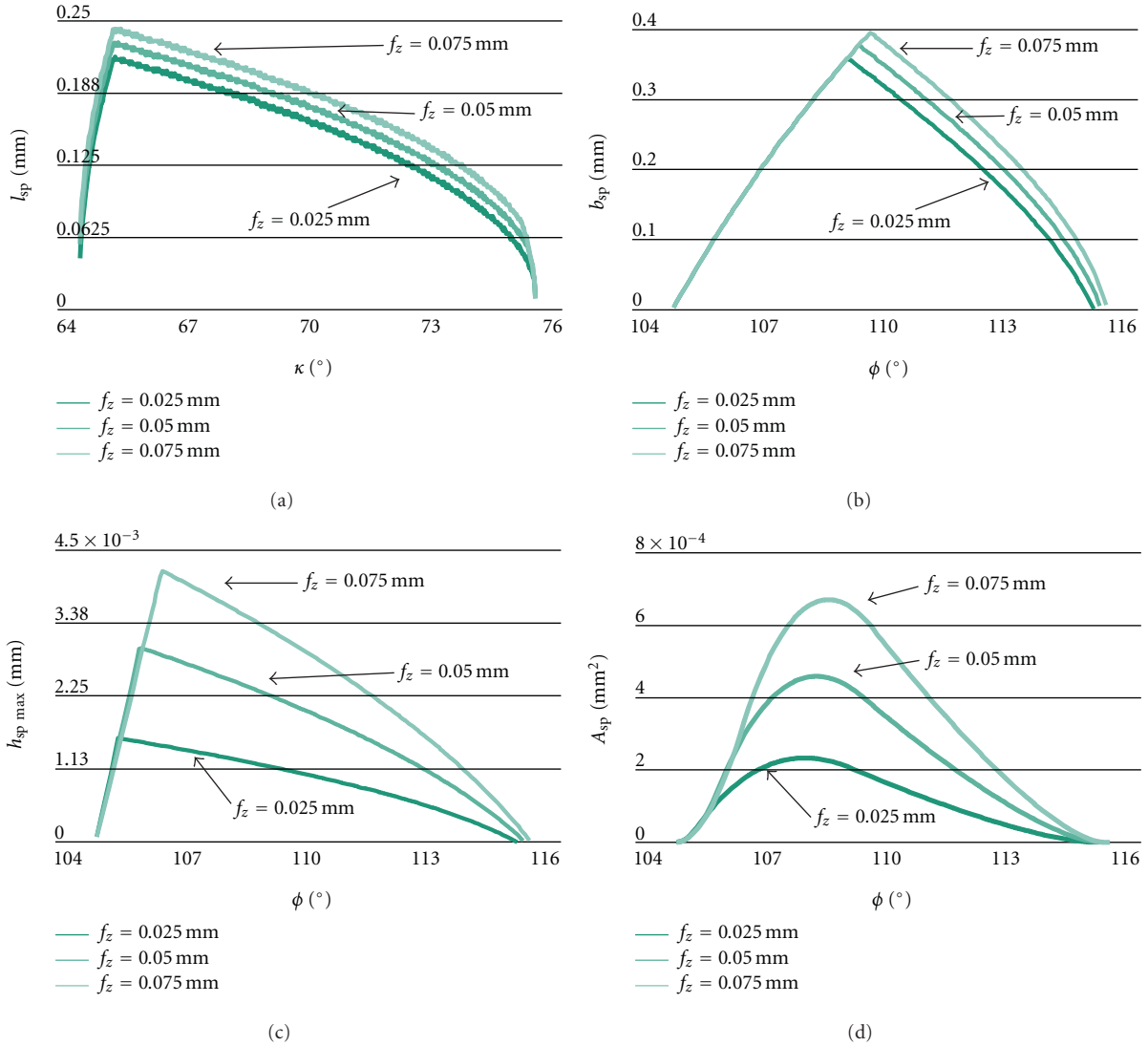
Figure 11: Influence of the feed-rate on the chip geometry.

the chip. This means that the end surface was generated by using the highest cutting speed of the entire removed volume.

Figure 9 shows the contact diagram for a feed variation. This diagram can be used for assessing the engagement condition and choose optimized parameters. It was introduced by Urban [31], however, without the colour information. The abscissa is the rotation angle $\Phi$ and the ordinate the axial immersion angle $\kappa$. The colours represent the chip thickness.

The cutting speed varies continuously along the ordinate, with a variation of $\kappa$. This means that the bottom part of the chip in this diagram is machined at a lower cutting speed than the upper part. The tool rotates in the positive direction of $\Phi$, which means that the left part of the chip in the diagram is removed earlier than the right part. The feed variation does not affect the contact region substantially, implying just in a light increase of the chip in the $\Phi$ direction what can also be observed in the Figures 11(a) and 11(b).

Nevertheless, the feed-rate has a high impact on the chip thickness and consequently on the chip cross-section area, which are shown, respectively, in Figures 11(c) and 11(d). These two parameters are very important for the prediction of the process forces and of the load collective on the cutting edge.

Higher forces are expected for higher feed-rate values. This effect can, however, be compensated by changing the tool orientation. A more longitudinal chip (see contact diagram) would result in a smaller chip cross-sectional area and consequently smaller processes forces. This would theoretically decrease the tool wear and, thus, increase the tool life.

Nevertheless, a more longitudinal chip also results in a higher chip length, which is directly related to the tool wear, since an increase of the contact length between the cutting edge and the workpiece also increases the abrasion and adhesion effects. A good balance between these two effects is a diagonal chip geometry, as used in this paper, which reduces the chip cross-sectional area and simultaneously keeps the chipping length in a moderate range.
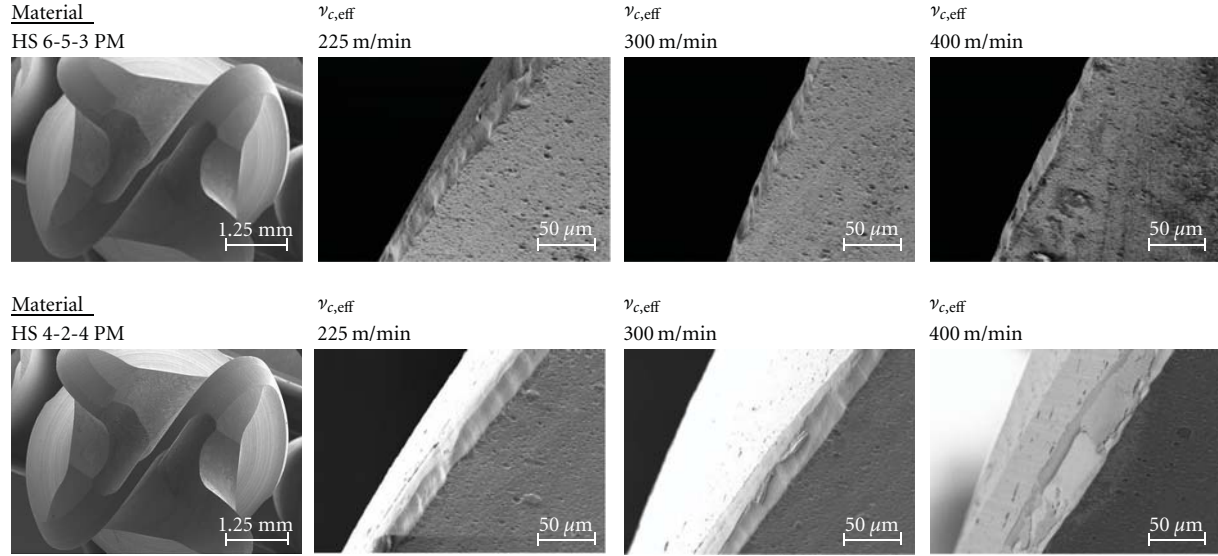
FIGURE 12: Tool wear qualification.

TABLE 4: Simulation input data.

| Cutting tool | |
|---|---|
| Tool diameter $D_0$ (mm) | 6 |
| Number of Flutes $n$ | 4 |
| Helix angle $\lambda$ (°) | 30 |
| Local helix angle $\lambda_l$ (°) | 21 |
| Cutting parameters | |
| Effective cutting speed $v_{c,\text{eff}}$ (m/min) | 225, 300, and 400 |
| Cutting speed at shaft $v_c$ (m/min) | 233, 311, and 414 |
| Feed per tooth $f_z$ (mm) | 0.025, 0.05, and 0.075 |
| Row width $a_{\text{en}}$ (mm) | 0.05 |
| Cutting depth $a_{\text{pn}}$ (mm) | 0.04 |
| Tilt angle $\beta_{\text{fn}}$ (°) | 75 |
| Workpiece position | C+ |
| Simulation parameters | |
| Discretization along the rotation angle $d\Phi$ (°) | 0.05 |
| Discretization along the axial immersion angle $d\kappa$ (°) | 0.02 |

## 4. Experimental Results and Discussion

*4.1. Qualification and Quantification of the Milling Tool Wear.*
Figure 12 exposes the qualified tool flank wear land (VB)
morphology after reaching an abort criterion of 75 $\mu$m in
terms of varying the work piece material and the effective
cutting speed $v_{c,\text{eff}}$.

While increasing $v_{c,\text{eff}}$ in machining both materials
the characteristic abrasion of the tool flank developed
progressively homogenous without any hinds of cutting-edge
fracture, cracking, and shell-shaped spalling of the TiAlN-
coating on the flank of the rake face. While increasing $v_{c,\text{eff}}$ in
machining of HS 4-2-4 PM a noticeable increase in adhesion
related tool flank wear was observed.

In the case of the high-speed steel HS 6-5-3 PM (64 HRC)
the tool flank wear land VB evolved nearly linear with a
progressing cutting length $L_c$ at each parameter setting; see
Figure 13. In the beginning of machining, a characteristic
initial abrasive wear evolved until reaching a $L_c$ of nearly
25 m, where the wear development curve slightly flattened
until $L_{c,\text{max}}$ was reached.

Conversely to Elbestawi et al. [12], the introduced,
however not proved, hypothesis of Salomon [13] is con-
firmed, stating that for an increase of $v_{c,\text{eff}}$ from 225 m/min
up to 300 m/min the maximum cutting length $L_{c,\text{max}}$ is
improved by 33%. After performing of milling tests at $v_{c,\text{eff}}$ =
400 m/min a further tool life improvement in respect to a
$v_{c,\text{eff}}$ of 300 m/min was detected.

Although the cold working steel HS 4-2-4 PM (66 HRC)
is slightly harder than HS 6-5-3 PM (64 HRC), a $L_{c,\text{max}}$ better
than 200 m was proofed.

After reaching 60 m in cutting length, the wear evolution
curve significantly flattened for each cutting speed setting
and rose linearly until $L_{c,\text{max}}$. The abort criterion of 75 $\mu$m
in VB was first detected after 220 m of cutting length at an
$v_{c,\text{eff}}$ of 225 m/min. $L_c$ increased nearly linear with increasing
$v_{c,\text{eff}}$.

Additionally, in Figure 14, for clarifying the influence of
feed per tooth $f_z$ regarding the wear evolution of the milling
tool on a random basis, $f_z$ was varied in terms of 0.025, 0.05,
and 0.075 mm/tooth at a $v_{c,\text{eff}}$ of 300 m/min for both work
piece materials.

It was found out that depending on the material charac-
teristics of HS 4-2-4 PM in a narrow cutting parameter range
a decreasing feedrate negatively influenced $L_{c,\text{max}}$. Increasing
$f_z$ from 0.05 mm/tooth ($L_c$ = 240 m) up to 0.075 mm/tooth
accompanied with an significant improvement in cutting
length up to 320 m. Hence, on the other hand, increasing
$f_z$ increases the cusp to valley which accompanies with
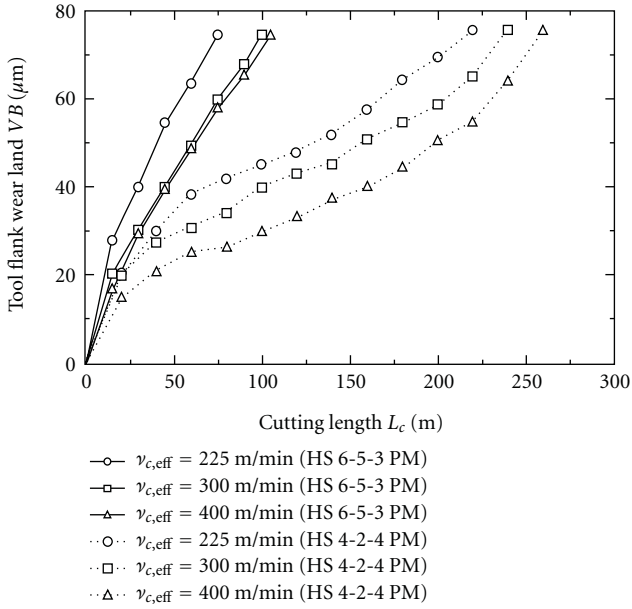an increased surface roughness. At first appearance, this

FIGURE 13: Influence of varied work piece material and varied effective cutting speed on the tool flank wear land.



FIGURE 14: Influence of varied work piece material and fead per tooth on the tool flank wear land at $v_{c,\text{eff}}$ = 300 m/min.



FIGURE 15: Influence of varied work piece material and the inclination cutting length on the tool flank wear land.

result is legitimate, because during machining with $f_z$ = 0.025 mm/tooth in regard of $f_z$ = 0.075 mm/tooth each flute of the milling tool is exposed with a tripled impact peak with the work piece surface per considered cutting length. Interestingly, in case of the HS 6-5-3 PM, in a narrow parameter range the influence of the impact peak per cutting length is nearly negligible. For further investigating the influence of $f_z$ to the tool flank wear land VB, the friction inclination length $L_{\text{In}}$ of the tool, respectively, to the work piece surface was presented in Figure 15. Interestingly, considering only VB as an function of $L_{\text{RF}}$, decreasing $f_z$ to 0.025 mm accompanies with a drastically increasing of tool life in comparison to $f_z$ = 0.05 and 0.075. This observation indicates that the impact peak alone is by far not the determining factor for tool wear.

Contrary to comparable investigations, it can be supposed that the increased inclination length in terms of lower $f_z$ and the microscopic structural integrity especially the thermal conductivity of the work piece material have a great influence to the microscopic flow behaviour and hence a significant effect on the tool life and wear characteristic of the milling tool. Considering the investigated materials, the thermal conductivity of HS 6-5-3 PM (24 W/mk) is significantly higher compared to HS 4-2-4 PM (19,6 W/mK). So, it can be suggested that the thermal conductivity $k$ has an important influence on the chipping mechanisms in high-speed dry-hard milling. With increased thermal conductivity the thermal transfer resistance decreases, and the thermal energy of the chipping process can easily penetrate into the work piece surface instead through the chip. Hence, due to an advanced thermal load in the subsurface area around the contact point between tool and work piece the plasticisation of the work piece material and the softening of the chip improves. In this case, it is expected, because of the relatively low thermal conductivity of HS 4-2-4 PM, that the amount
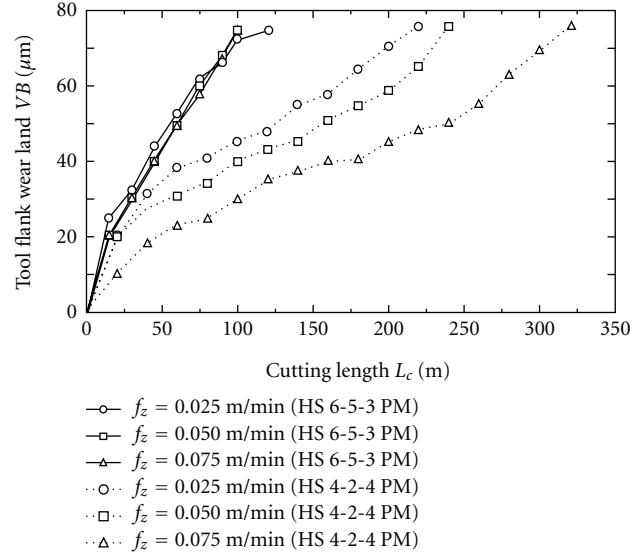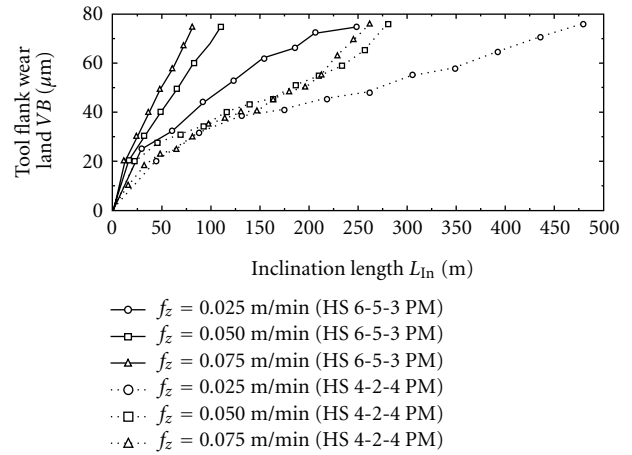
of thermal energy generated in the chipping process, which dissipated through the chips, was significantly higher than in HS 6-5-3 PM. On the other hand, in HS 4-2-4 PM the size of carbides is significantly smaller and the distribution of the carbides is more homogenous compared to HS 6-5-3 PM. Hence, friction resistance in the contact zone between work piece and milling tool will be significantly lower in HS 4-2-4 PM. Hence, the local thermal impact to the subsurface area of the work piece will be noticeable reduced and the machinability of HS 4-2-4 PM and the cutting performance of the solid carbide ball-end mills drastically enhanced due both the thermal conductivity as well as the microstructural integrity of the material.

*4.2. Quantification of Process Forces.* Increasing of the effective cutting speed $v_{c,\text{eff}}$ in machining HS 6-5-3 PM generated
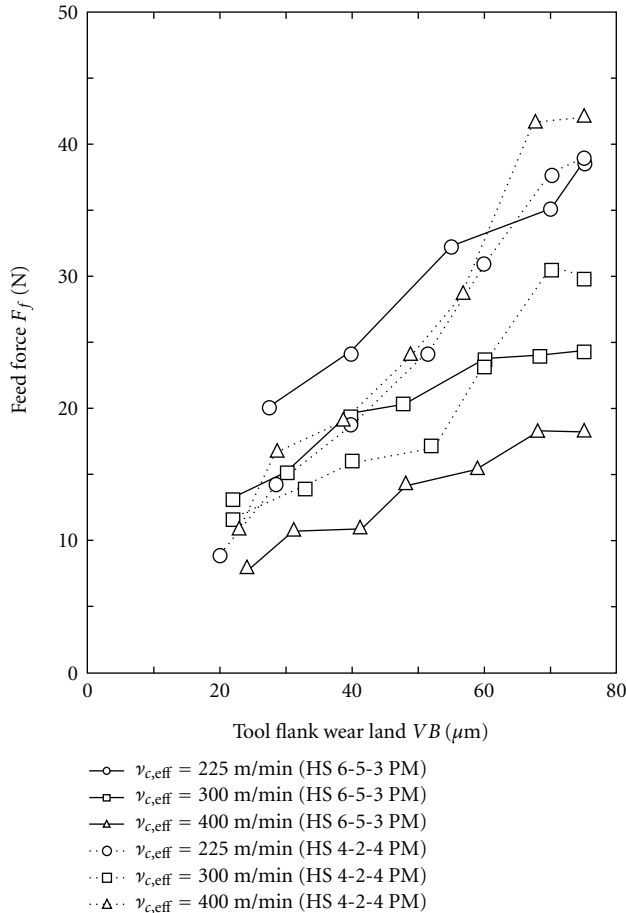
FIGURE 16: Influence of varied work piece material and progressing tool flank wear land on the resulting feed force.

elevated process temperatures, hence the plasticisation of the work piece material enhanced and process force, especially the feed force $F_f$ (Figure 16), significantly decreased.

$F_f$ increased proportionally with progressive tool flank wear land VB. With advanced $v_{c,\text{eff}}$ the curve of the $F_f$ with progressing VB significantly flattened. Machining with $v_{c,\text{eff}}$ = 400 m/min considering 225 m/min, resulted in reduction of $F_f$ by nearly 50%. In machining HS 4-2-4 PM, the $F_f$ curve increased more sharply with advanced cutting speeds. Interestingly, while machining with a fresh tool at VB $\sim$20 $\mu$m, for each $v_{c,\text{eff}}$ $F_f$ evolved from nearly a range of 9 to 14 N. After reaching the abort criterion of 75 $\mu$m in terms of VB, a maximum feed force $F_{f,\text{max}}$ of 39 N for 225 m/min, 30 N for 300 m/min, and 43 N for 400 m/min in effective cutting speed were quantified.

After performing of milling tests on both work piece materials with fresh tools at $v_{c,\text{eff}}$ of 400 m/min and $f_z$ of 0.05 mm a roughness of $R_a$ < 0.12 $\mu$m was measured.

## 5. Conclusion

In order to characterise the cutting force related wear progression and cutting performance of solid carbide ball-end mills in high-speed dry-hard milling of hardened powder metallurgical steels, the tool wear flank land, the cutting length, and the process forces were investigated.

(1) While increasing the effective cutting speed in machining of two powder metallurgical produced steels, HS 6-5-3 PM (64 HRC) and a HS 4-2-4 PM (66 HRC), a characteristic abrasion of the used solid carbide ball-end mills developed progressively homogenous.

(2) An iterative increase in effective cutting speed resulted in a significantly enhanced tool life.

(3) Depending on the material characteristics of the investigated work piece materials, in a narrow cutting parameter range an increased federate was accompanied by an enhanced tool life.

(4) Increasing of the effective cutting speed $v_{c,\text{eff}}$ in machining HS 6-5-3 PM resulted in a significantly decreased feed force and enhanced tool life.

(5) In machining HS 4-2-4 PM the feed force increased more sharply with advanced cutting speeds while tool life was tripled in regard to HS 6-5-3 PM.

(6) It was supposed that with decreased thermal conductivity of the considered work piece material the thermal transfer resistance increases, and hence, the local thermal impact to the subsurface area of the work piece will be noticeable reduced as well as the cutting performance of the solid carbide ball-end mills drastically enhanced.

## References

[1] I. Jung, "Moderne Hochleistungsstähle für den Formen- und Werkzeugbau, Tagungsunterlagen," in *Proceedings of the Seminar für Werkzeugtechnik*, 2002.

[2] D. Biermann, A. Baschin, E. Krebs, and J. Schlenker, "Manufacturing of dies from hardened tool steels by 3-axis micromilling," *Production Engineering, Research and Development*, vol. 5, no. 2, pp. 209–217, 2011.

[3] B. Denkena, D. Boehnke, and R. Meyer, "Reduction of wear induced surface zone effects during hard turning by means of new tool geometries," *Production Engineering, Research and Development*, vol. 2, no. 2, pp. 123–132, 2008.

[4] H. K. Tonshoff, C. Arendt, and R. Ben Amor, "Cutting of hardened steel," *Annals of the CIRP*, vol. 49, no. 2, pp. 547–566, 2000.

[5] F. Klocke, S. Knodt, S. Altmüller, and A. Bilsing, "Fräsverfahren stellen hohe ansprüche an werkzeug und maschine," *Werkstatttechnik Wt*, vol. 89, no. 10, pp. 451–455, 1999.

[6] F. Klocke, V. Zinkann, and K. Gerschwiler, "Hochleistungswerkstoffe erfordern angepasste Bearbeitungstechnologien," *VDI-Z*, vol. 139, no. 6, pp. 18–24, 1997.

[7] R. Piotrowiak, V. Schüler, I. Schruff, and C. Spiegelhauer, "Sprühkompaktierte Hochleistungs-Werkzeugstähle," *HTM Zeitschrift für Werkstoffe, Wärmebehandlung und Fertigung*, vol. 59, no. 6, pp. 423–431, 2004.

[8] A. Schulz, E. Matthaei-Schulz, S. Spangel, R. Tinscher, H. Vetters, and P. Mayr, "Das primärgefüge sprühkompaktierter

stähle," *HTM Zeitschrift für Werkstoffe, Wärmebehandlung und Fertigung*, vol. 56, no. 2, pp. 104–109, 2001.

[9] A. Schulz, V. Uhlenwinkel, C. Escher et al., "Sprühkompaktierte hochlegierte werkzeugstähle—herstellung und eigenschaften," *HTM Zeitschrift für Werkstoffe, Wärmebehandlung und Fertigung*, vol. 60, no. 2, pp. 87–95, 2005.

[10] Y. Matsumoto, M. M. Barash, and C. R. Liu, "Cutting mechanisms during machining of hardened steels," *Materials Science and Technology*, vol. 3, no. 4, pp. 299–305, 1987.

[11] J. Köhler, *Berechnung der zerspankräfte bei variierenden spanungsquerschnittsformen*, Doctoral thesis, Hannover, Germany, 2010.

[12] M. A. Elbestawi, L. Chen, C. E. Becze, and T. I. El-Wardany, "High-speed milling of dies and molds in their hardened state," *Annals of the CIRP*, vol. 46, no. 1, pp. 57–62, 1997.

[13] C. Salomon, "Verfahren zur bearbeitung von metallen oder bei einer bearbeitung durch schneidende werkzeuge sich ähnlich verhaltende werkstoffe," Deutsches Patent Nr. 523594, 931, 4, 1931.

[14] F. Klocke and W. König, *Fertigungsverfahren Drehen, Fräsen, Bohren*, vol. 8, Springer, Berlin, Germany, 2008.

[15] P. Koshy, R. C. Dewes, and D. K. Aspinwall, "High speed end milling of hardened AISI D2 tool steel (~58 HRC)," *Journal of Materials Processing Technology*, vol. 127, no. 2, pp. 266–273, 2002.

[16] M. Okada, A. Hosokawa, R. Tanaka, and T. Ueda, "Cutting performance of PVD-coated carbide and CBN tools in hardmilling," *International Journal of Machine Tools and Manufacture*, vol. 51, no. 2, pp. 127–132, 2011.

[17] F. Klocke and V. Zinkann, "Hochgeschwindigkeitsbearbeitung ändert die Spanbildung," *VDI-Z*, vol. 141, no. 3-4, pp. 30–34, 1999.

[18] E. El-Magd and C. Treppmann, "Mechanical behaviour of materials at high strain rates," *Scientific Fundamentals of HSC*, pp. 113–136, 2001.

[19] S. Knodt, *Hartfräsen pulvermetallurgisch erzeugter ledeburitischer Werkzeugstähle*, Doctoral thesis, Aachen, Germany, 2004.

[20] M. Soković, J. Kopač, L. A. Dobrzański, and M. Adamiak, "Wear of PVD-coated solid carbide end mills in dry high-speed cutting," *Journal of Materials Processing Technology*, vol. 157-158, pp. 422–426, 2004.

[21] Y. S. Liao and H. M. Lin, "Mechanism of minimum quantity lubrication in high-speed milling of hardened steel," *International Journal of Machine Tools and Manufacture*, vol. 47, no. 11, pp. 1660–1666, 2007.

[22] R. Ben Amor, *Thermomechanische Wirkmechanismen und Spanbildung bei der Hochgeschwindigkeitszerspanung*, Doctoral thesis, Hannover, Germany, 2003.

[23] M. Elbestawi, M. Dumitrescu, T. I. El-Wardany, and J. Böhner, "Effect of carbide tool grades and cutting edge geometry on tool life during high speed machining of hardened tool steel," in *Proceedings of the 2nd International Conference on High Speed Machining*, pp. 37–46, 1999.

[24] Y. Altintaş and P. Lee, "Mechanics and dynamics of ball end milling," *Journal of Manufacturing Science and Engineering, Transactions of the ASME*, vol. 120, no. 4, pp. 684–692, 1998.

[25] Y. Altintas, *Manufacturing Automation, Metal Cutting Mechanics, Machine Tool Vibrations, and CNC Design*, Cambridge University Press, New York, NY, USA, 2000.

[26] A. Zabel, *Prozesssimulation in der zerspanung—modellierung von dreh und fräsprozessen*, Habilitation thesis, Dortmund, Germany, 2010.

[27] C. A. van Luttervelt, T. H. C. Childs, I. S. Jawahir et al., "Present situation and future trends in modelling of machining operations progress report of the CIRP working group "modelling of machining operations," *CIRP Annals-Manufacturing Technology*, vol. 47, no. 2, pp. 587–624, 1998.

[28] I. Lazoglu and S. Y. Liang, "Modeling of ball-end milling forces with cutter axis inclination," *Journal of Manufacturing Science and Engineering*, vol. 122, no. 1, pp. 3–11, 2000.

[29] R. Zhu, S. G. Kapoor, and R. E. DeVor, "Mechanistic modeling of the ball end milling process for multi-axis machining of free-form surfaces," *Journal of Manufacturing Science and Engineering*, vol. 123, no. 3, pp. 369–379, 2001.

[30] E. Ozturk and E. Budak, "Modeling of 5-axis milling processes," *Machining Science and Technology*, vol. 11, no. 3, pp. 287–311, 2007.

[31] B. Urban, *Kinematische und mechanische wirkungen des kugelkopffräsens*, Doctoral thesis, Hannover, Germany, 2009.

*Research Article*

# Wear Behavior and Its Correlation with Mechanical Properties of TiB$_2$ Reinforced Aluminium-Based Composites

## N. B. Dhokey and K. K. Rane

*Department of Metallurgy and Material Science, Government College of Engineering, Pune 411005, India*

Correspondence should be addressed to N. B. Dhokey, nbdhokey@yahoo.co.in

Aluminium-based TiB$_2$ reinforced composite is a promising material to be used as brake drum material, and it may emerge as substitute for conventional gray cast iron. Aluminium-based composites containing 2% by wt copper reinforced with 2.5 and 5 wt% TiB$_2$ composites were made in induction furnace by in situ synthesis process using simultaneous addition of halide fluxes (K$_2$TiF$_6$ and KBF$_4$). These cast composites were evaluated for microstructures, hardness, flow curve properties, and tensile properties. It was observed that overall wear behavior gave reasonably good correlation with mechanical properties of composites as compared to gray cast iron.

## 1. Introduction

Metal matrix composite containing ceramic particulates tends to improve mechanical properties as well as wear properties by way of creating restriction to deformation of material during mechanical working. Metal matrix composites (especially aluminium and titanium based) are used in aerospace and automobile industries due to their enhanced properties such as modulus, hardness, tensile strength, and wear resistance combined with significant weight saving [1, 2]. Aluminium with ceramic reinforcements such as Al$_2$O$_3$, SiC, TiC, and TiB$_2$ are used for structural applications, for their good toughness and wear resistance [3]. Modulus of composite increases with TiC- and TiB$_2$-particle additions and it is greater than that for composite with Al$_2$O$_3$ and SiC. Also, interfacial bonding is enhanced in the TiC- and TiB$_2$-added composites [4]. There are different techniques of forming TiB$_2$ in the matrix such as powder metallurgy method, spray, deposition and several casting methods such as rheocasting, squeeze casting, stir-casting and compo casting [5, 6]. Different systems are used for synthesis of this composite such as TiO$_2$-Al-B, TiO$_2$-Al-B-CuO, TiO$_2$-Al-B$_2$O$_3$, NaBH$_4$, and TiCl$_4$ and Ti-containing and B-containing salts are added to the melt resulting in a series of chemical reactions which produce submicron TiB$_2$ particles within the melt [3, 7, 8]. The addition of reinforcement produces increase in strength and stiffness over the base alloy at the expense of ductility as compared to cast aluminium [4, 9]. The wear rate of the composites improves significantly with the TiB$_2$ content. The friction coefficient also decreased with increasing TiB$_2$ content, which indicates decrease in wear rate and hence the improvement in the wear resistance of the composite [10, 11]. Wear and mechanical properties of commercially used grades of cast irons (GI250, GIHC, GI 250Ti, and CGI) suggest that compact graphite cast iron exhibits higher mechanical strength among all grades, but it has less wear resistance than other grades of cast irons [12].

It is well known that application of Al-MMC in automotive components can reduce the weight of the vehicle by one third over gray cast iron. The aim of the present work is to establish a correlation of wear behavior with mechanical properties of the Al-TiB$_2$ composites as compared to gray cast iron.

## 2. Materials and Experimental Methods

*2.1. Materials and Processing.* Commercially pure (CP) aluminium was taken as matrix material. In situ flux assessed
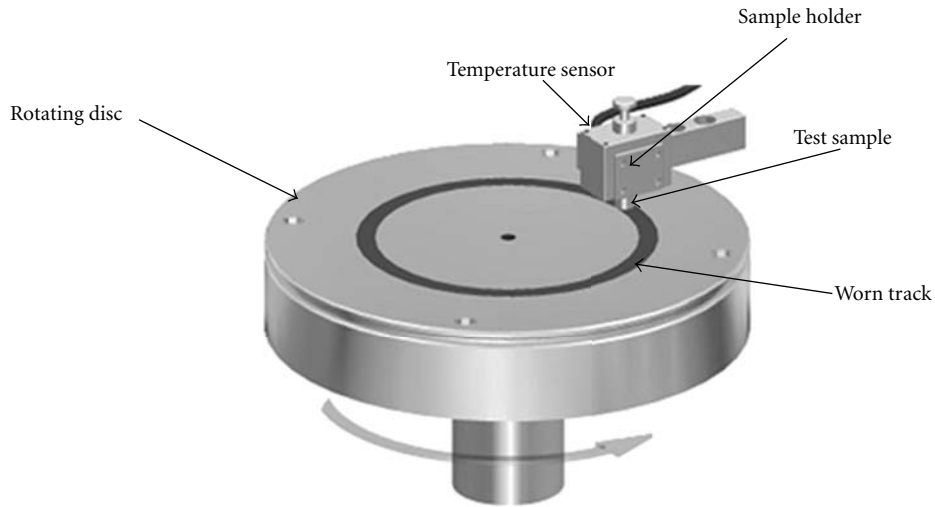
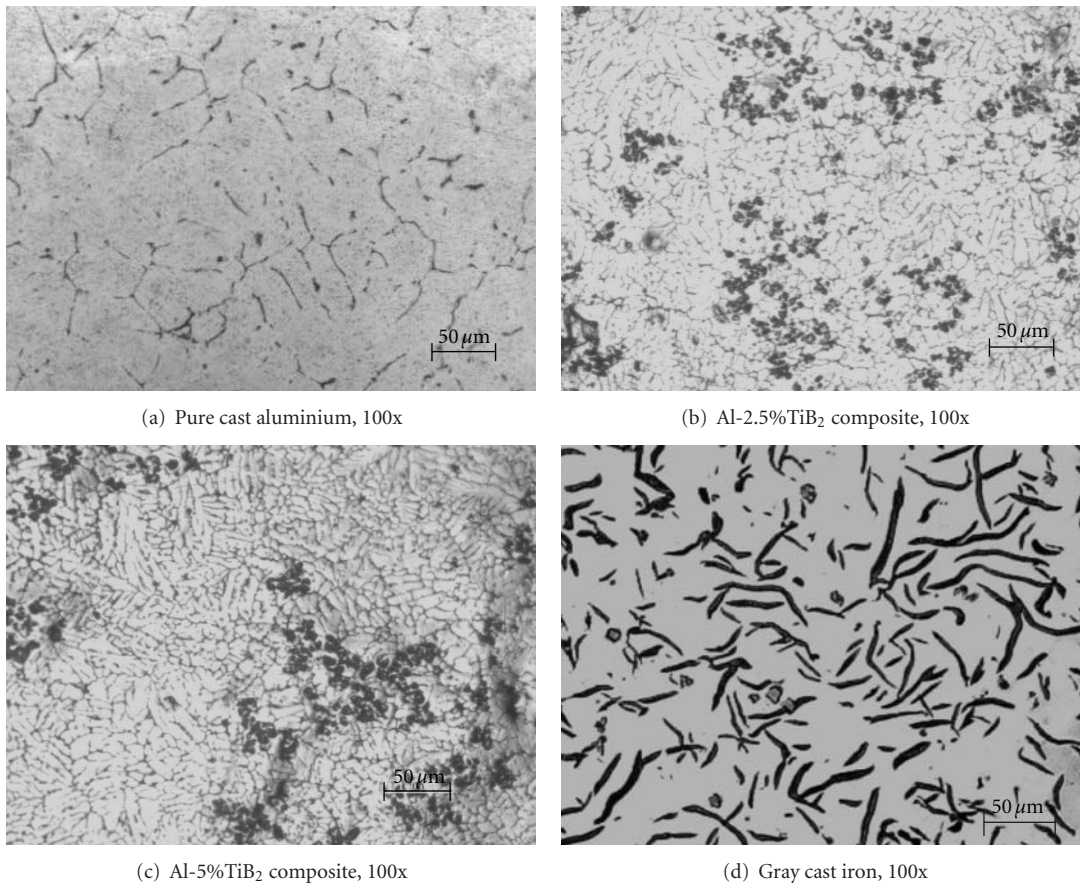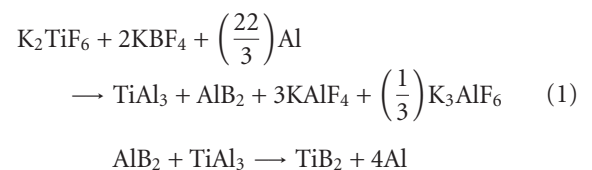Figure 1: Schematic configuration of Pin-on-Disc machine employed for wear test.



(a) Pure cast aluminium, 100x

(b) Al-2.5%$TiB_2$ composite, 100x

(c) Al-5%$TiB_2$ composite, 100x

(d) Gray cast iron, 100x

Figure 2: Optical micrographs of cast aluminium, Al-2.5%$TiB_2$ Al-5%$TiB_2$ composite and gray cast iron.

synthesis technique was used to form $TiB_2$-reinforced composite by using commercially available fluoride based fluxes that is, potassium hexafluorotitanate ($K_2TiF_6$) and potassium tetrafluororate ($KBF_4$). In situ synthesis process was adopted for the fabrication of the composite. Individual fluxes that is, potassium hexafluorotitanate ($K_2TiF_6$) and potassium tetrafluororate ($KBF_4$), were added together in molten aluminium and reacted as given by (1)

$$K_2TiF_6 + 2KBF_4 + \left(\frac{22}{3}\right)Al$$
$$\longrightarrow TiAl_3 + AlB_2 + 3KAlF_4 + \left(\frac{1}{3}\right)K_3AlF_6 \quad (1)$$
$$AlB_2 + TiAl_3 \longrightarrow TiB_2 + 4Al$$

Formation of $TiB_2$ is greatly influenced by the presence of $AlB_2$ and $Al_3Ti$ in molten aluminium. But due to the fact that
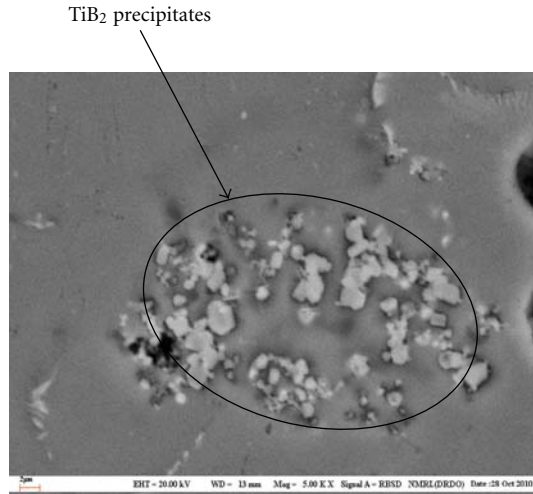
TiB$_2$ precipitates



FIGURE 3: SEM micrograph shows magnified image of segregated pockets of TiB$_2$ in aluminium matrix at 5000x.

Gibbs free energy for formation of Al$_3$Ti is higher than AlB$_2$, the recovery of boron is lower [13]. Hence 20% extra KBF$_4$ addition compared to stoichiometric amount was made to reduce the presence of allied products and complete the reaction to produce TiB$_2$ reinforcement [14]. The properties of synthesized composites were compared with gray cast iron used for brake drum of automotive applications and it consists of 3.54% C, 2.15% Si and 0.51% Mn (by wt).

Induction furnace (25 KW, Make Autocontrol, Mumbai) was used for making the composites with controlled argon shrouding and as well as for gray cast iron as the reference material. After sufficient holding time and degasing of melt, the molten composite was poured into preheated mould (200°C) to get cast specimens of dimensions 150 mm length and 20 mm diameter for material charaterisation.

*2.2. Material Characterization.* Reinforcement phases were observed in scanning electron microscope (make-JOEL, Japan). Samples for SEM analysis were polished by using electrolytic polishing machine (Eletropol Metatech) with a flow of electrolyte solution (Methanol-730 mL, Butyl Cellosolve-98 mL, Perchloric acid-78 mL and Distilled water-100 mL). Additionally, for revealing grain boundaries of matrix and reinforcement distribution, the etching was carried out using Villella reagent (20 mL Hydrofluoric acid, 10 mL Nitric acid, 30 mL Glycerin).

The hardness of composite was measured by using micro hardness machine (FM-700, Future-tech). The load applied was 100 gram with dwell time of 15 seconds. An average of six readings was reported.

Tensile test specimens were made as per ASTM A 370 standard and tested in a Universal Testing Machine (Capacity 10 Tons). The average data values of three samples obtained from tensile test were used. In the same machine, compression testing was carried on specimen having $L/D = 1$ ($D = 20$ mm). The specimen was gradually pressed in compression in steps of 1000 Kg, and its instantaneous height

and diameter were recorded to get true stress verses true strain plot, using an average of three test specimens. The corresponding flow curve equation was derived for each composite studied

$$\sigma = k \times \epsilon^n, \qquad (2)$$

where $\sigma$ = true stress in MPa, $\epsilon$ = true strain, and $n$ = strain hardening exponent.

Pin-on-Disc wear test machine (M/s Magnum Engineers, Bangalore) was used for wear analysis. Pin specimen (Ø 10 mm) was kept stationary perpendicular to disc, while the circular disc (SAE 52100 steel, 61 HRC, 0.3 $\mu$RA, and disc diameter 165 mm) was rotated as shown in Figure 1. A load of 60 N and sliding velocity 1.8 m/s was employed for wear rate evaluation. An average wear rate was reported based on three samples of same composition. In order to find out the rise in temperature during wear test, temperature sensor was positioned in 1 mm diameter drilled hole at 15 mm distance from sliding end of the specimen.

## 3. Results and Discussion

*3.1. Microstructural Analysis.* Optical microstructure of Al-TiB$_2$ composites with different reinforcement content are shown in Figure 2. As compared to pure aluminium, average grain size of phase in composite is relatively small.

*3.2. SEM Microstructure.* Figure 3 shows microstructure of Al-5% TiB$_2$ composite segregated spot of TiB$_2$ (Figure 3) in the aluminium matrix. Typically, TiB$_2$ particles are present in the segregated manner due to high interfacial energy.

*3.3. SEM-EDS Analysis with Elemental Distribution.* SEM-EDS analysis was used to ascertain approximate chemical composition of reinforcement and also that of matrix. Figure 4 indicate spectrum of Al-5% TiB$_2$ composite with peaks of aluminium and titanium. EDS elemental analysis indicated in Figure 5 confirms the presence of TiB$_2$ precipitates. Figure 6 shows elemental distribution that confirms the presence of boron, aluminium, and titanium.

*3.4. Microhardness Analysis.* The hardness of composite with different reinforcement content was compared with gray cast iron as reference material. Figure 7 shows variation of Al-MMC for varying reinforcement content of TiB$_2$. Al-based composite containing 2.5 wt% TiB$_2$ indicate 47% improvement in hardness and this goes up with increasing TiB$_2$ content. It is noticed that hardness of 5% TiB$_2$ is increased by almost twice than that of pure aluminium but much less than that of gray cast iron.

*3.5. Mechanical Properties*

*3.5.1. Tensile Properties.* It is evident from Table 1 that the composite exhibited higher UTS and higher fracture strength than aluminium with reduced ductility. The significant improvement in the mechanical properties of the composite
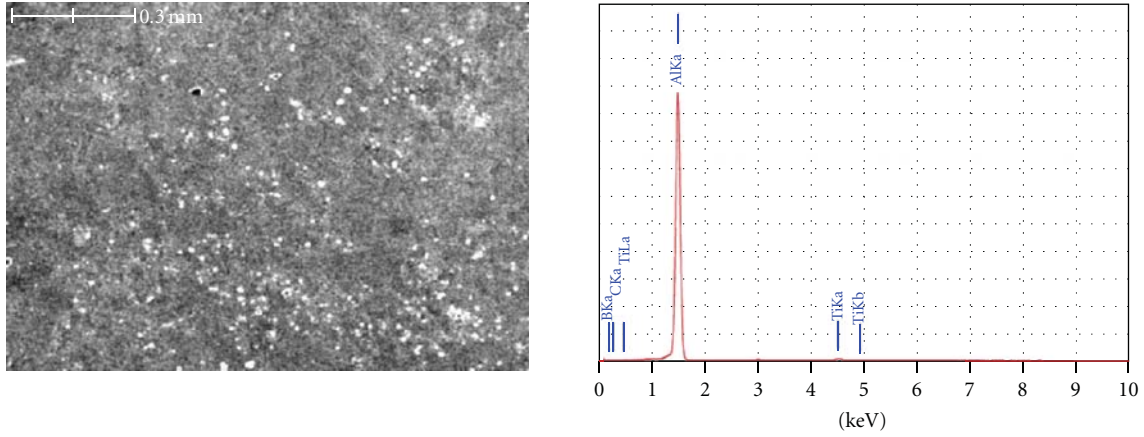
| Element | (keV) | Mass (%) | At (%) |
|---------|-------|----------|--------|
| B | — | — | — |
| Al | 1.486 | 97.67 | 98.67 |
| Ti | 4.508 | 2.33 | 1.33 |
| Total | | 100 | 100 |

FIGURE 4: EDX spectrum and elemental mapping of Al-5%TiB$_2$ composite.
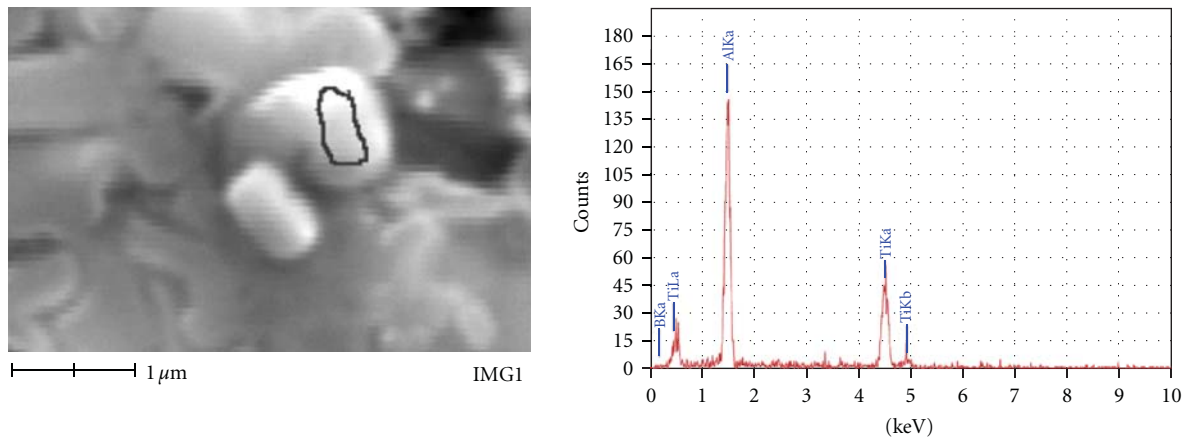


| Element | (keV) | Mass (%) | At (%) |
|---------|-------|----------|--------|
| B | 0.183 | 42.45 | 70.26 |
| Al | 1.486 | 28.47 | 18.88 |
| Ti | 4.508 | 29.08 | 10.86 |
| Total | | 100 | 100 |

FIGURE 5: EDX spectrum and elemental mapping on TiB$_2$ particle.

TABLE 1: Data of tensile test conducted on cast Al, Al-MMCs and gray cast iron.

| Sr. no. | Properties | Pure aluminium | Al-2.5%TiB$_2$ | Al-5%TiB$_2$ | Gray cast iron |
|---------|------------|----------------|----------------|--------------|----------------|
| 1 | Y.S (MPa) | 74 | 93 | 96 | — |
| 2 | UTS (MPa) | 121 | 157 | 180 | 284 |
| 3 | Fracture strength (MPa) | 70 | 78 | 150 | 284 |
| 5 | %Reduction in area | 22.53 | 16.84 | 9.38 | 3.19 |
| 6 | %Elongation | 8 | 6.5 | 6 | 3 |
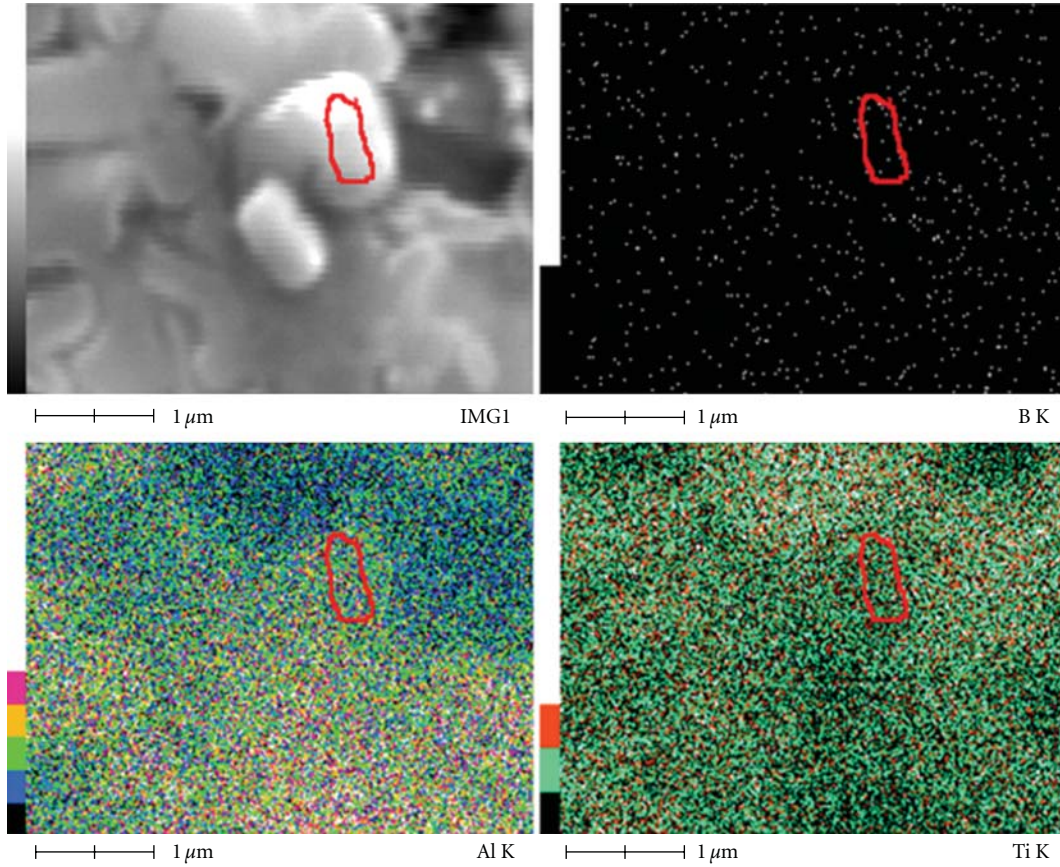
FIGURE 6: Elemental distribution of boron, aluminium, titanium nearby TiB$_2$ clusters.

TABLE 2: Flow curve properties of composite materials.

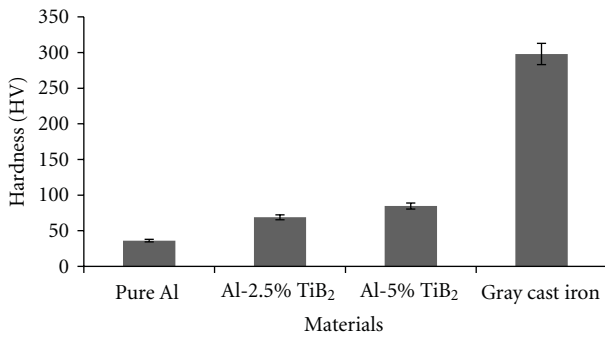| Sr. no. | Properties | Pure aluminium | Al-2.5%TiB$_2$ | Al-5%TiB$_2$ |
|---|---|---|---|---|
| 1 | $K$ (MPa) | 137 | 138 | 141 |
| 2 | $n$ | 0.412 | 0.375 | 0.324 |
| 3 | Gross increase in area (along radial direction) | 56.25% | 45.56% | 42.12% |
| 4 | Gross reduction in height (along longitudinal direction) | 34.5% | 31.5% | 28.5% |



FIGURE 7: Hardness variation of cast aluminium, Al-TiB$_2$ composites, and gray cast iron.

as compared with the aluminium can be attributed to TiB$_2$ particles in the matrix. Similar trend of increasing tensile properties is reported by previous researchers in case of Al-12% by wt. TiB$_2$ and Al-4.5% Cu-3% C-15%TiB$_2$ composites [15, 16]. The fractured surfaces as depicted in Figure 8 shows a shift in fracture behavior from ductile to brittle; for example, pure aluminium indicates cup and cone type ductile fracture, Al-5% TiB$_2$ reveals mixed mode ductile-brittle transition, and gray cast iron shows brittle fracture.

*3.5.2. Flow Curve Properties.* Compression test results are plotted in the form of flow curve, and the corresponding properties derived from flow curve equation are given in Table 2. It can be observed that strength coefficient ($K$) increases with increase in reinforcements, whereas strain hardening decreases with increased TiB$_2$ content. Overall, higher TiB$_2$ content shows higher strain hardening rate ($n$). It means that composite exhibits appreciable deformation behavior which can be seen from gross deformation both in transverse as well as in longitudinal direction.
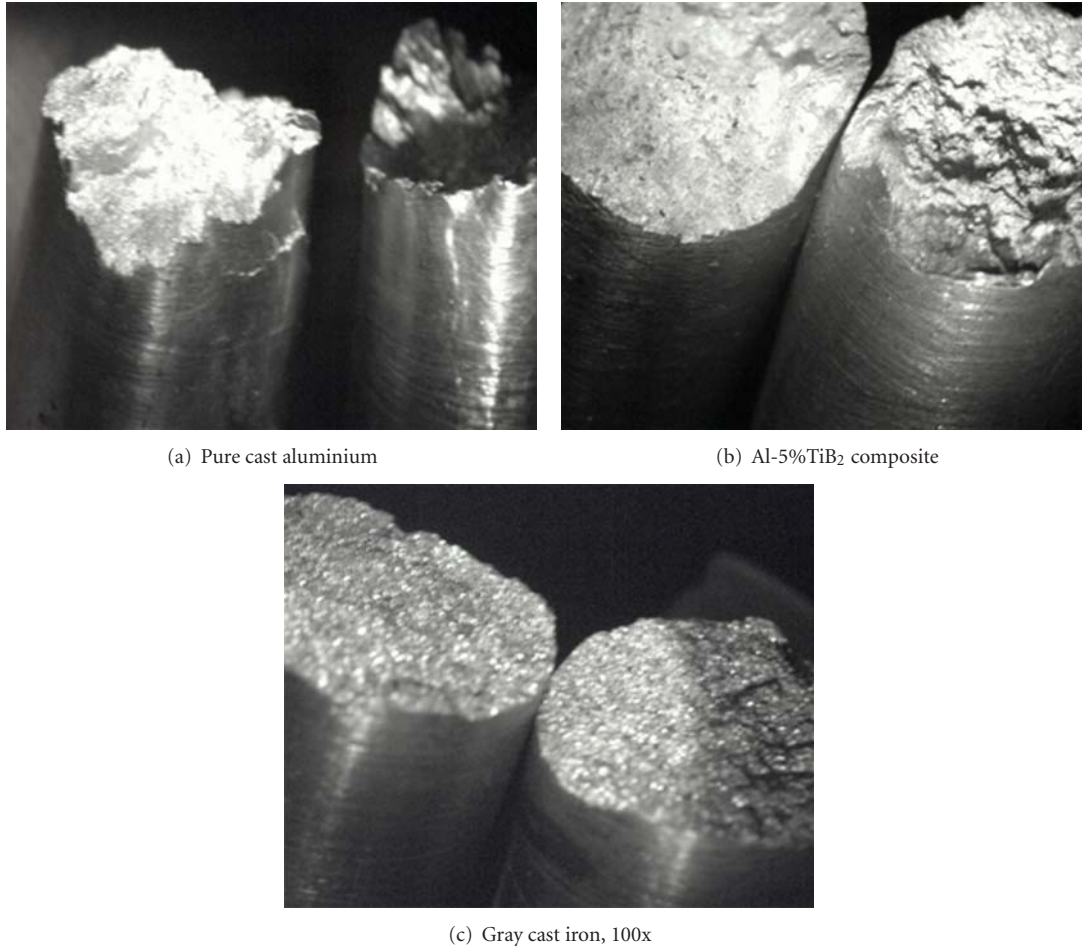
(a) Pure cast aluminium



(b) Al-5%TiB$_2$ composite



(c) Gray cast iron, 100x

FIGURE 8: Stereomicrographs of tensile fractured surfaces of (a) Cast aluminium, (b) Al-5%TiB$_2$ composite and (c) Gray cast iron.



FIGURE 9: Wear rate variation of sliding pins made out of different materials.
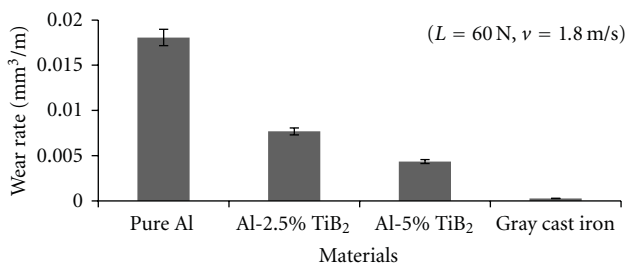


FIGURE 10: Temperature rise variation of sliding pins made out of different materials.

### 3.6. Sliding Wear Analysis.

**Figure 9** shows the variation of wear rate with composition for MMCs. Apparently, pure aluminium exhibits the highest wear loss whereas gray cast iron shows the lowest wear loss, for the given set of applied load and sliding speed employed. Al-based composite shows a decrease in wear rate with increasing content of TiB$_2$ reinforcement which acts as obstacle to shear deformation, while material is getting slid on the counterface. However, wear rate is much higher than gray cast iron. Also, TiB$_2$ acts as load-bearing e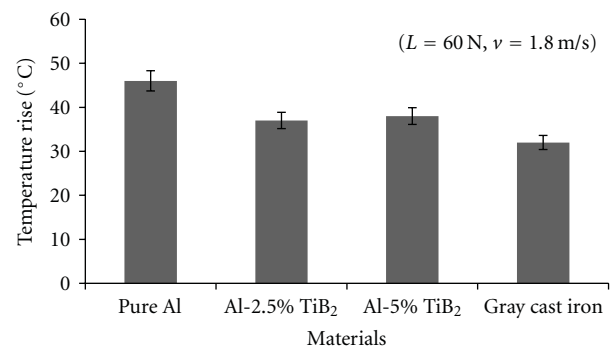lement in the matrix. This supports the work reported elsewhere in TiB$_2$-reinforced Al-7%Si alloy [17]. **Figure 10** shows that temperature rise during sliding is more for pure aluminium and its composites than that of gray cast iron. It is well known that aluminum exhibits high thermal conductivity (237 W/m·K), and it reduces with increasing addition of TiB, while gray cast iron has relatively low thermal conductivity (70 W/m·K). It can be noted that
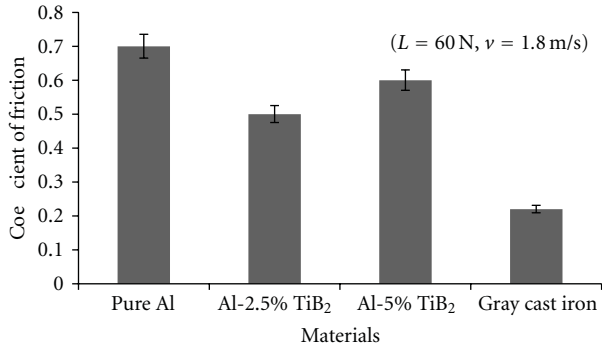
FIGURE 11: Coefficient of friction variation of sliding pins made out of different materials.
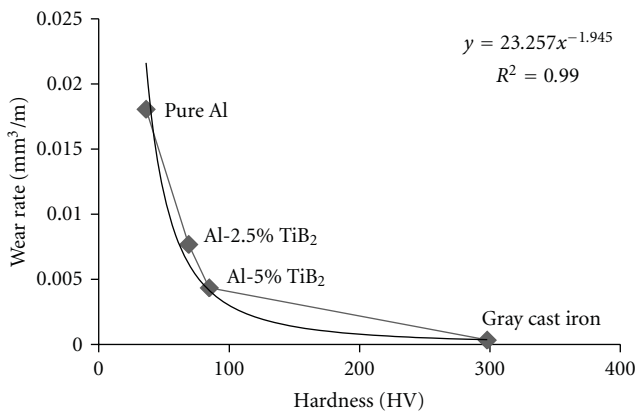


FIGURE 13: Effect of ultimate tensile strength on wear rate of composites.



FIGURE 12: Effect of hardness on wear rates of composites.
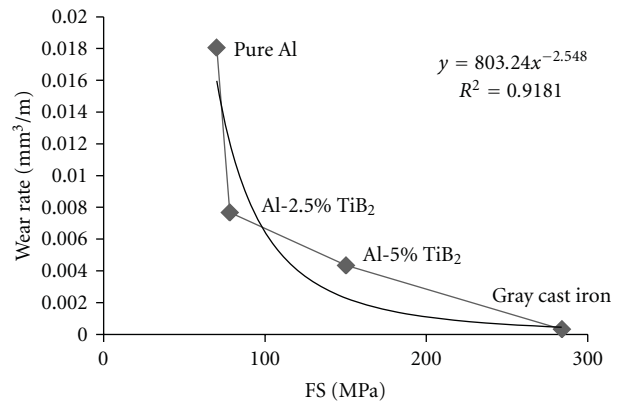


FIGURE 14: Effect of fracture strength on wear rates of composites.

the addition of $TiB_2$ particle to the aluminium matrix gives some effect on reducing the coefficient of friction as evident in Figure 11. The variation in the average coefficient of friction for the pure aluminium and composites varies in the range of 0.5–0.7 which is much larger than that of gray cast iron (0.21).

## 4. Correlation of Mechanical Properties with Wear Behavior

Wear is a complex phenomenon and governed not only by hardness, but also by other influencing parameters like microstructure, method of processing, thermal properties of the sliding material, and mechanical properties [18]. A correlative wear model based on mechanical, thermal, physical properties and process parameters has been attempted to understand wear complexity [19].

Various plots of mechanical properties as derived from tensile test and compressive test are plotted to establish correlation with wear properties. It is noted that wear rate shows approximate power law relationship with hardness (Figure 12), UTS (Figure 13), fracture stress (Figure 14), strength coefficient (Figure 15), and strain hardening exponent (Figure 16). All these relationship, give $R^2$ value that is much higher than 0.9, indicting strong effect of mechanical
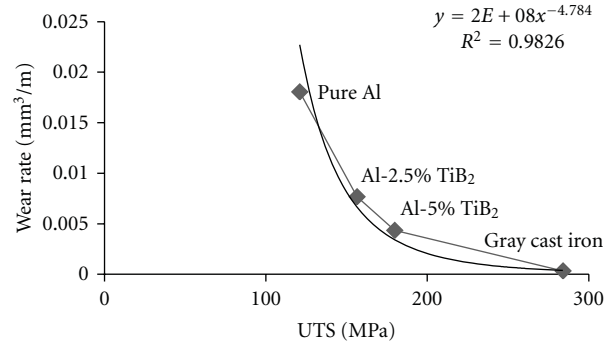
properties on wear rates. It may be noted that mechanical properties are strongly affected by reinforcement in microstructures. Thus, volumetric wear rate follows certain trend with hardness of the material validating Archard's equation [20]. Similar effort of finding out correlation of Young's modulus and hardness on wear resistance was made for alloys with different elemental addition of La, Mg, Pd, and Zr. It was found out that hardness and Young's modulus both correlate well with wear resistance for Al-Ni group of alloys [21].

## 5. Conclusions

Based on the forgoing discussion of Al-MMCs and its relative comparison with gray cast iron, the following conclusions can be drawn.

(1) Mechanical properties are strongly affected by the content of $TiB_2$ in Al-MMCs.

(2) Wear behavior gives a reasonable correlation with hardness, ultimate tensile strength, fracture strength, and strain hardening exponent of Al-MMCs. The relationship between wear rate and mechanical properties validates Archard's equation.

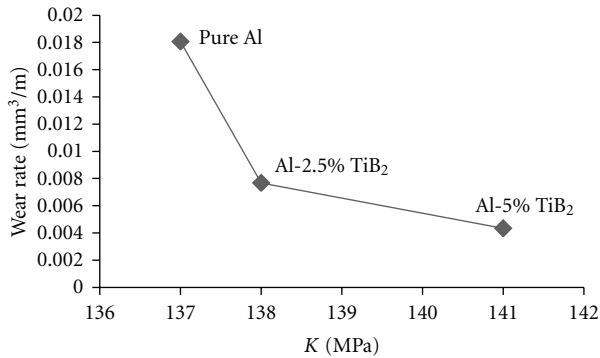(3) Wear rate decreases with increasing $TiB_2$ content.

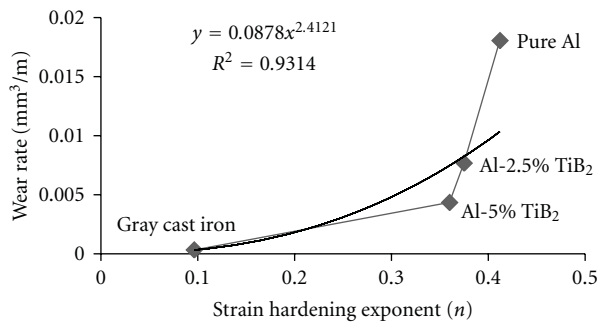FIGURE 15: Effect of strengthening coefficient on wear rate of composites.



FIGURE 16: Effect of strain hardening exponent on wear rate of composites.

## Acknowledgments

## References

[1] T. Zeuner, P. Stojanov, P. R. Sahm, H. Ruppert, and A. Engels, "Developing trends in disc brake technology for rail application," *Materials Science and Technology*, vol. 14, no. 9-10, pp. 857–863, 1998.

[2] R. Dwivedi, "Development of advanced reinforced aluminum brake rotors," *SAE Technical Paper Series*, vol. 104, no. 5, pp. 159–166, 1995.

[3] S. C. Tjong, S. Q. Wu, and H. G. Zhu, "Wear behavior of in situ $TiB_2 \cdot Al_2O_3$/Al and $TiB_2 \cdot Al_2O_3$/Al-Cu composites," *Composites Science and Technology*, vol. 59, no. 9, pp. 1341–1347, 1999.

[4] A. R. Kennedy, A. E. Karantzalis, and S. M. Wyatt, "The microstructure and mechanical properties of TiC and $TiB_2$-reinforced cast metal matrix composites," *Journal of Materials Science*, vol. 34, no. 5, pp. 933–940, 1999.

[5] Y. Han, X. Liu, and X. Bian, "In situ TiB2 particulate reinforced near eutectic Al-Si alloy composites," *Composites—Part A*, vol. 33, no. 3, pp. 439–444, 2002.

[6] M. J. Koczak and M. K. Premkumar, "Emerging technologies for the in-situ production of MMCs," *JOM*, vol. 45, no. 1, pp. 44–48, 1993.

[7] L. Shi, Y. Gu, L. Chen, Z. Yang, J. Ma, and Y. Qian, "A convenient solid-state reaction route to nanocrystalline $TiB_2$," *Composites*, vol. 36, no. 2, pp. 1177–1187, 2005.

[8] F. C. Wang, Z. H. Zhang, J. Luo, C. C. Huang, and S. K. Lee, "A novel rapid route for in situ synthesizing TiB-$TiB_2$ composites," *Composites Science and Technology*, vol. 69, no. 15-16, pp. 2682–2687, 2009.

[9] D. G. Zhao, X. F. Liu, Y. C. Pan, X. F. Bian, and X. J. Liu, "Microstructure and mechanical properties of in situ synthesized ($TiB_2 + Al_2O_3$)/Al-Cu composites," *Journal of Materials Processing Technology*, vol. 189, no. 1–3, pp. 237–241, 2007.

[10] A. Mandal, B. S. Murty, and M. Chakraborty, "Sliding wear behaviour of T6 treated A356-$TiB_2$ in-situ composites," *Wear*, vol. 266, no. 7-8, pp. 865–872, 2009.

[11] S. Natarajan, R. Narayanasamy, S. P. Kumaresh Babu, G. Dinesh, B. Anil Kumar, and K. Sivaprasad, "Sliding wear behaviour of Al 6063/$TiB_2$ in situ composites at elevated temperatures," *Materials and Design*, vol. 30, no. 7, pp. 2521–2531, 2009.

[12] G. Cueva, A. Sinatora, W. L. Guesser, and A. P. Tschiptschin, "Wear resistance of cast irons used in brake disc rotors," *Wear*, vol. 255, no. 7–12, pp. 1256–1260, 2003.

[13] L. Lü, M. O. Lai, Y. Su, H. L. Teo, and C. F. Feng, "In situ $TiB_2$ reinforced Al alloy composites," *Scripta Materialia*, vol. 45, no. 9, pp. 1017–1023, 2001.

[14] N. B. Dhokey, S. Ghule, K. Rane, and R.S. Ranade, "Effect of $KBF_4$ and $K_2TiF_6$ on precipitation kinetics of $TiB_2$ in aluminium matrix composite," *Journal of Advance Material Letters*, vol. 2, no. 3, pp. 210–216, 2011.

[15] K. L. Tee, L. Lü, and M. O. Lai, "Improvement in mechanical properties of in-situ Al-$TiB_2$ composite by incorporation of carbon," *Materials Science and Engineering A*, vol. 339, no. 1-2, pp. 227–231, 2003.

[16] T. V. Christy, N. Murugan, and S. Kumar, "A comparative study on the microstructures and mechanical properties of Al 6061 Alloy and the MMC Al 6061/$TiB_2$," *Journal of Minerals & Materials Characterization & Engineering*, vol. 9, no. 1, pp. 57–65, 2010.

[17] S. Kumar, M. Chakraborty, V. Subramanya Sarma, and B. S. Murty, "Tensile and wear behaviour of in situ Al-7Si/$TiB_2$ particulate composites," *Wear*, vol. 265, no. 1-2, pp. 134–142, 2008.

[18] S. C. Lim and M. F. Ashby, "Overview no. 55 Wear-Mechanism maps," *Acta Metallurgica*, vol. 35, no. 1, pp. 1–24, 1987.

[19] N. B. Dhokey and R. K. Paretkar, "Study of wear mechanisms in copper-based $SiC_p$ (20% by volume) reinforced composite," *Wear*, vol. 265, no. 1-2, pp. 117–133, 2008.

[20] J. F. Archard, "Contact and rubbing of flat surfaces," *Journal of Applied Physics*, vol. 24, no. 8, pp. 981–988, 1953.

[21] A. L. Greer, K. L. Rutherford, and I. M. Hutchings, "Wear resistance of amorphous alloys and related materials," *International Materials Reviews*, vol. 47, no. 2, pp. 87–112, 2002.

*Review Article*

# Friction Induced Wear of Rapid Prototyping Generated Materials: A Review

## A. Tsouknidas

*Laboratory for Machine Tools and Manufacturing Engineering, Mechanical Engineering Department,*
*Aristoteles University of Thessaloniki, 54124 Thessaloniki, Greece*

Correspondence should be addressed to A. Tsouknidas, alextso@auth.gr

Additive manufacturing has been introduced in the early 80s and has gained importance as a manufacturing process ever since. Even though the inception of the implicated processes predominantly focused on prototyping purposes, during the last years rapid prototyping (RP) has emerged as a key enabling technology for the fabrication of highly customized, functionally gradient materials. This paper reviews friction-related wear phenomena and the corresponding deterioration mechanisms of RP-generated components as well as the potential of improving the implicated materials' wear resistance without significantly altering the process itself. The paper briefly introduces the concept of RP technologies and the implicated materials, as a premises to the process-dependent wear progression of the generated components for various degeneration scenarios (dry sliding, fretting, etc.).

## 1. Introduction

Rapid prototyping (RP) poses a promising alternative to conventional manufacturing techniques during concept evaluation, design optimization, rapid tooling, and lately for direct production of customer driven products. The comparative advantages of additive manufacturing are both cost and time related while RP facilitates the direct incorporation of functional characteristics into the final product.

The basic concept of RP techniques relays on the conversion of 3D geometries, generated or processed by computer-aided design (CAD), into an STL file format. This is followed by the segmentation of the object in a series of overlaying layers, an essential step in the bottom-up approach of any additive manufacturing process. RP processes initiate with the construction of the objects' base layer and progress upwards, with each layer being deposited/formed on top of the proceeding one, finally resulting in the desired 3D geometry.

This approach circumvents limitations associated with conventional manufacturing methods, provides products with competitive strength characteristics, allows the fabrication of geometries of unequal complexity, while simplifying the incorporation of application specific features into the produced object [1].

Several industrial sectors (automotive, aerospace, and medical) have embraced, supported, and in some cases even dictated recent advances in RP, leading to customized, high added value products, whereas the implicated technologies can be easily extended to numerous other applications.

Rapid prototyping technologies can be categorized into three main categories: solid based like fused deposition modeling (FDM), powder based as selective laser sintering (SLS), and liquid based methods, for example, stereolithography. Further classifications can refer to the processed material (metallic, ceramic, polymer, or composite) as well as the employed bonding/fusing technique.

Several material properties of RP-generated products have to be considered during the proper technique selection [2]. Among these prevails friction-dependent wear, which may be considered a pivotal property of mechanical components utilized in a series of applications where mating surfaces are subjected to sliding.

Friction-based surface degeneration is a major determinant of a mechanical components' longevity, that is, artificial joints [3], implants [4, 5], gears [6], bearings [7], seals [8],

and so forth, are primarily wear dependent, while their wear resistance is also strongly associated with the parts' periodical service requirements.

Hitherto substantial contributions have been made on the current state-of-the art rapid prototyping, manufacturing, and tooling techniques [9–12]. The tribological aspects; however, of RP-produced components have, to the best of the author's knowledge, never been extensively documented.

## 2. Methods and Materials

*2.1. RP Technologies.* Friction-induced failure is considered an important aspect during the material/process selection of a suiting RP methodology. Furthermore, RP techniques are extensively employed in clean room environments and the medical sector where the release of wear particles and ions is considered a significant sterility problem [13]. Recent advances in RP technologies not only allow the fabrication of components able to withstand conventional sterilization processes but also incorporate gamma-ray sterilization and similar techniques into their systems, allowing the direct commercial production of FDA-approved implants. The release of particles due to friction, during the components function, may arise this issues nonetheless, thus the wear resistance of these techniques has to be thoroughly considered.

There exist a variety of more than 40 different RP technologies, which do, however, bare similar characteristics and are alike in concept. Selective laser sintering (SLS) is an RP technique utilizing a laser beam to fuse small material particles into a 3-dimensional shape. The laser scans a predefined contour on the surface of a powder bed, which is consecutively lowered by a one-layer thickness, only to be covered by the powdered material, which is reapplied on top of the sintered cross-section, as schematically presented in Figure 1. This process is repeated until the complete fabrication of the desired 3D geometry. Virtually any material that can be powdered, plastic, polymer, ceramic, metals or even composites can be fused, employing SLS technologies [14, 15]. The limitations of the method are associated with the thermal properties of the commissioned powder, which must maintain its integrity and not completely decompose once the laser is applied. Selective laser melting (SLM) is a recent alterative to the SLS process, which relies on the complete melting of the powdered materials.

Fused deposition modeling (FDM) is another widely applied RP process [10, 16] based on materials exhibiting a low melting point even though harder materials can also be employed [17]. In this context polymers or plastics are utilized as the main material matrix, which can be reinforced, by metallic fibers or ceramic fillers. The final thermosoftening powder is guided through a heated nozzle and deposited through the extrusion head as a partially liquefied (semisolid) wire, as demonstrated in Figure 2. The CNC-controlled nozzle follows the desired tool-path, defined by a specific slice of the CAD file, gradually structuring the desired object.
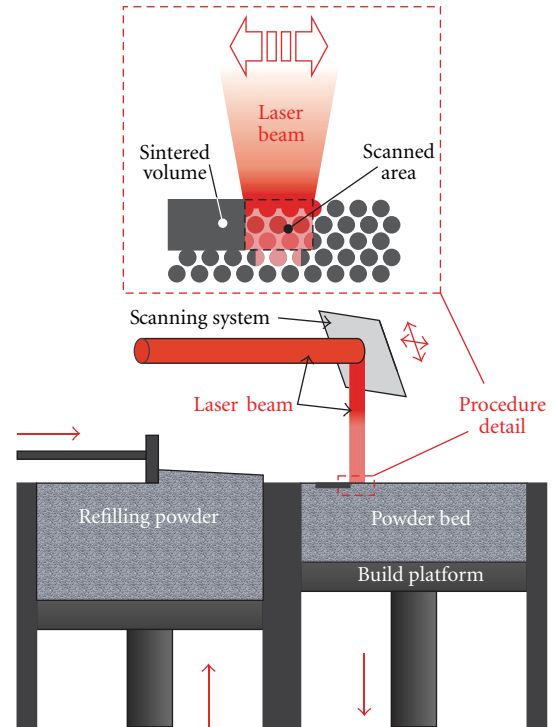


FIGURE 1: Selective laser sintering process.

This review will focus on the wear development and the related wear mechanisms of FDM-produced polymeric and binary polymer-ceramic composites [18, 19] as well as SLS- and SLM-fabricated metallic parts ranging from stainless and tool steels to Ti and Co alloys [15, 20].

*2.2. Fretting Wear Test.* Fretting wear, refers to the friction-based interfacial damage of a component pressed against a repetitive tangential vibrating countersurface. This oscillatory motion is usually defined by small displacement amplitudes [21, 22], during which the specimen is fixed and the counter-surface is subjected to a linearly vibrating motion (see Figure 3), or vice versa.

The concept of fretting replicates the friction-based wear of a series of RP applications, accurately mimicking their mechanical behavior. Artificial joints, hip implants, and several other RP-fabricated components are especially prone to friction fatigue, drastically reducing their life expectancy [23, 24].

Even though fretting results in complex wear mechanisms, there is a consensus throughout literature concerning the existence of three major fretting modes: fretting wear [25, 26], fretting fatigue, and fretting corrosion [27].

A dominating phenomenon in fretting is the so-called "third body effect" exerted by the entrapment of material debris within the sliding interface due to the minute relative displacements of the two counterbodies [28]. This material response, provides composites with their exceptional wear properties, as their coefficient of friction drastically alters due to this in situ lubricant effect, exerted by the formation
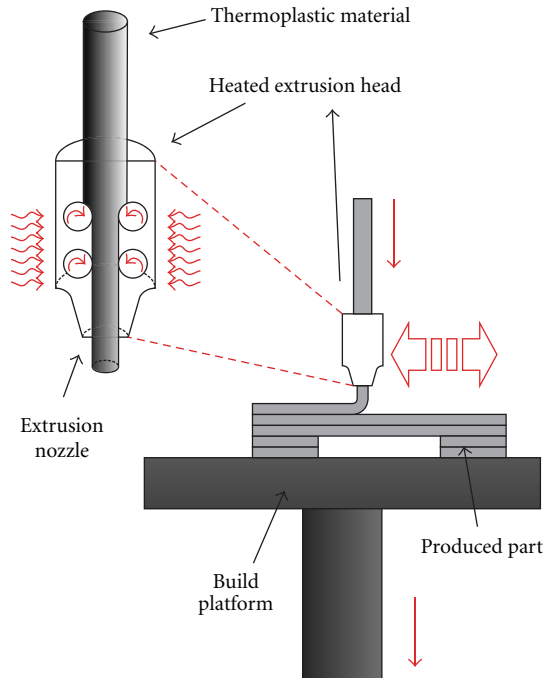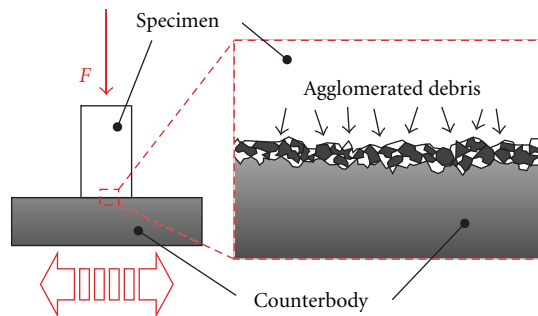
FIGURE 2: Fused deposition modeling process.



FIGURE 3: Fretting concept—third body effect.



FIGURE 4: Pin-on-disc concept—break in phase.

of an inhomogeneous transfer layer mainly consisting of particles with higher wear resistance [29, 30].

*2.3. Tribometer Friction Tests.* The determination of a materials dry sliding wear characteristics is conventionally conducted by means of pin-on-disc (POD) arrangements, as illustrated in Figure 4, and in correspondence to the ASTM G99-04 [31] standard. POD tests are based on a simplified sliding concept, were the accumulation of wear debris is rather insignificant and thermal degeneration less likely to affect the wear progression when compared to fretting.

During POD experiments, a pin-like specimen is pressed against a sliding counter-surface by the application of a dead weight. The counter-surface is usually composed of a metallic disc rotating at a constant velocity and possessing a specific roughness value (Ra), which is considered a critical factor [32, 33]. The examined specimens must be polished thoroughly (by grit emery paper) to ensure the uniform and axial contact of their surface to the disc and reduce
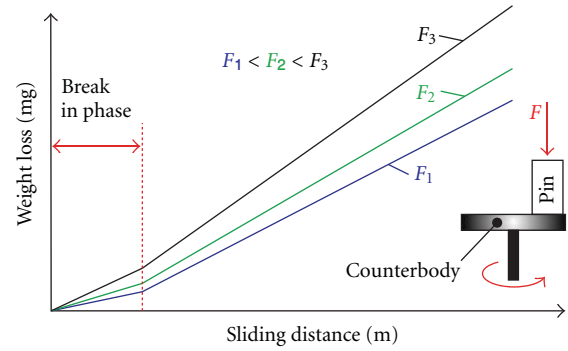
the so called "break in phase," encountered during the initial sliding period, were foreign materials are removed from the contacting surfaces and a complete contact of the counterbodies is established [18].

## 3. Friction and Wear Behavior

*3.1. Effect of the Materials' Strength Properties.* Although it would be anticipated that the material strength properties exert a vital role on the wear behavior of the RP-fabricated materials, existing research states otherwise, as presented in Figure 5. It has been documented that Ti and Co-alloys exhibit increased (by more than two magnitudes) wear rates during fretting when compared to stainless steels, which are far more ductile [15]. The same tendency is observed when comparing SLS/SLM iron-based materials with milled tool steels, which possess higher strength properties, paradoxically the SLS/SLM materials demonstrate superior wear characteristics [15]. Laser sintered Mo-WC MMC's have also been reported to exhibited better abrasive wear resistance when compared to the base metal [34]. Even when compared to conventional sintering, SLS is capable of producing iron-graphite components with substantially different wear properties [35].

A similar material response has been observed in FDM-produced materials, where hardness cannot be considered as an indicator of wear resistance [18].

*3.2. Effect of Reinforcement.* Even though the material strength properties cannot be directly correlated to the wear resistance of RP-produced components, the enslavement of the materials' wear progression to the presence of a reinforcement phase has been well documented (see Figure 5).

The dispersion of hard particles like silicon carbide within a laser sintered iron matrix has a clear effect on the resulting composite's wear rates during dry sliding, as this results in an increased coefficient of friction. Wear volumes, however, tend to decrease drastically with an augmentation of the w/w% silicon carbide content [36]. This behavior can be attributed to onset adhesive processes such as scuffing [37] while improving the components wear and seizure resistance.
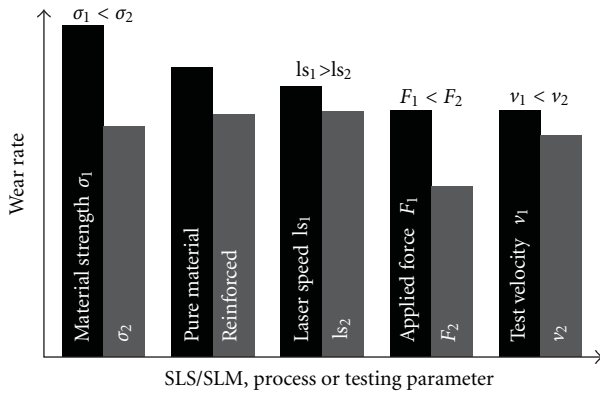
Figure 5: Qualitative impact of several SLS/SLM process and testing parameters on the resulting wear rate.
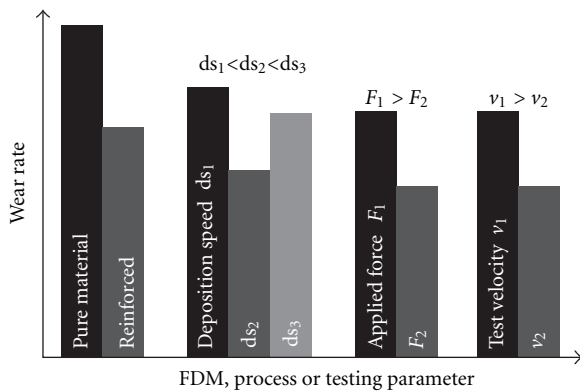


Figure 6: Qualitative impact of several FDM process and testing parameters on the resulting wear rate.

It has been implied that the incorporation of ductile materials like copper, which may be considered a low-friction element, can also increase the wear resistance of iron-based SLS materials [15] while the additions providing insignificant interfacial bonding or poor miscibility of the blended materials may deteriorate the wear-resistance of the composites [38].

When examining the effect of filler materials on a polymeric matrix produced via FDM, it is important to consider that polymers are wear sensitive materials and thus a ceramic reinforcement or metallic fibers may significantly enhance the composite's wear resistance. This has been observed among others, when reinforcing a polycaprolactone (PCL) matrix with hydroxyapatite (HAP). The effect of the ceramic filler material (HAP) exerted a significant effect on the wear progression of the examined biocomposites during dry sliding [19]. Even though the impact of the composition was not linear to the resulting wear progression it was able to enhance the wear resistance of the polymeric matrix by more than 60%. The qualitative effect of the reinforcement on the wear rate of FDM-produced materials is given in Figure 6.

*3.3. Effect of SLS/SLM Parameters.* SLS and SLM procedures can only be influenced to a certain extent. The laser

speed has been documented to hold a noteworthy effect on both coefficient of friction and wear resistance of the produced parts [36]. An increase in fusion speed of the employed powders, consequences in a decrease of coefficient of friction for both, the metallic material and its silicon carbide reinforced matrix. This can be accredited to the reduced densification of the material, as higher laser speed decreases the amount of energy absorbed by the powder, hence resulting in inferior local melting/sintering of the materials [39, 40]. Reduced density fosters decreased asperity interaction, hence reducing the coefficient of friction during dry sliding, as depicted in Figure 5.

A similar effect is observed when reducing the laser power, as this falls within the prior described concept of reduced densification. An increase of laser power simply marks the transition of SLS to SLM while a further rise would diminish process accuracy due to uncontrolled powder liquefaction.

*3.4. Effect of FDM Parameters.* It is widely accepted that the alteration of FDM process parameters can significantly affect the mesostructure of the manufactured parts as both, inter- and intralayer bonding is strongly process dependent [18]. In these terms, it may be stated that there exists a complex correlation of FDM process parameters on the wear degeneration of the produced parts (as demonstrated in Figure 6). Several studies have focused on the optimization of RP parameters during FDM [41] but very few have given emphasis on the resulting wear properties of the produced parts. The layer thickness of FDM products, in terms of the employed nozzle diameter, exerts a nonlinear effect on the wear rate of the manufactured parts. This can be attributed to the heat transfer from one layer to another [42]. As the temperature of a newly deposited layer is higher (close to the materials melting point) than the one of the proceeding layer (having already reached its glassy state), heat is transferred from the deposited layer to the substrate one. Depending on the layer thickness, this may act in favor of the products wear resistance as local remelting and thermal diffusion between adjunct filaments results in strengthening of the bonds between the layers [43]. This behavior is observed for large nozzle diameters and becomes even more intense as the diameter increases. An adverse effect can, however, be observed in small layer thicknesses, as the repeated heating and cooling of the polymer or plastic ultimately results in heterogenic temperature gradients within the processed material which lead to residual stresses [44]. These distortions are a dominating phenomenon that worsens the wear development of FDM processed parts up to a certain layer thickness.

The foregoing discussion stretches the importance of the proper heating of the processed material during FDM procedures, an augmentation of which up to a certain temperature will result in better bonding and thus higher wear resistance, while from this point on further increase will inevitably lead to material distortion and inferior wear rates. The geometry of FDM-produced parts, in terms of porosity and scaffold architecture may also affect the components

wear characteristics as these parameters strongly affect the heat dissipation within the parts structure. This involves a variety of conflicting factors as the complexity of built geometries may differ intensively. It is, however, accepted that high porosity and larger pore size may decrease friction dependent wear, although not notably [18].

*3.5. Effect of Testing Conditions.* Fretting tests conducted on a series metallic SLS components (Ti6Al4V, CoCrMo, stainless and tool steel, etc.) indicated that an increase of applied load is followed by a decreasing coefficient of friction while promoting higher wear volumes [15]. This behavior can be attributed to shearing of the surface's protuberances due to intensified plastic deformations, thus leading to increased wear rates [36]. It is noteworthy that a comparison between milled and RP tool steel, in terms of wear response, was in favor of latter in all examined load cases.

A similar correlation of applied load and coefficient of friction is encountered during dry sliding [36] although this alteration proved to be comparatively higher al low forces. In contrast to fretting, an increase of load leads to a reduction of wear rates during dry sliding (see Figure 4). This adverse effect tends to fade beyond a certain point, past which the load exhibits only a marginal effect on the coefficient of friction. It is stipulated that this wear response is due to the material composition, as an increase of load rises the temperature in the sliding interface, resulting in the formation of a hard oxide film, acting as a protective layer to the worn material. This may also justify the adverse effect of sliding velocity on the materials wear response in the case of pure Fe [36]. The initial presence of harder Si particles within an iron matrix results in increased wear volumes at higher sliding velocities, as anticipated.

Sliding velocity, however, is considered an important factor during dry sliding especially in the case of polymer-based materials [45], especially in the case of FDM-produced components, which are known to exhibit an intense correlation to applied the testing conditions. This is mainly due to the fact that polymers are far more prone to thermal effects observed during dry sliding/fretting, and it is well known that friction mechanisms are significantly affected by the developing thermal field in the material contact area [46, 47]. Hence an increase of sliding velocity during friction tests will elevate the temperature of the counter-bodies interface and thus is expected to reveal intense wear progression [48].

The variation of the wear rate of FDM-produced components with the contact load, is virtually linear to the increase of the applied dead weight, a behavior that can be attributed to the activation of the specimen roughness, leading to an increased coefficient of friction, gradually elevating the temperature of the contact interface.

## 4. Conclusions

It is important to presume that wear mechanisms of SLS/SLM-produced parts, subjected to fretting, are mainly composition depended as the examined materials exhibit controversial wear development. Although entrapment of material debris within the sliding interface is observed in all material cases, this can either deteriorate its wear resistance or exert a beneficial effect.

In stainless steels, this "third body effect" unveils an in situ lubricant effect, improving its wear resistance while in harder materials, as tool steels, this inhomogeneous transfer layer is composed of agglomerated debris depreciating their wear endurance.

Dry sliding of metallic SLS materials is less abrasive in terms of wear development. This can be explained by the reduced thermal interaction of the contacting materials as well as the absence of the "third body effect" exhibited by the accumulation of wear debris within the sliding interface.

The foregoing discussion revealed that processing parameters hold indeed a vital role on the produced materials wear resistance, although its composition exerts without a doubt the dominating impact.

The FDM process-dependent wear mechanisms compose a complex phenomenon and even though the effects of various process parameters on the resulting wear mechanisms can be identified, it is nearly impossible to interpret their interactions.

The incurred wear mechanisms during dry sliding (POD tests) are threefold.

 (i) Gauging of the polymers surface, which in the case of composite materials may evolve to excavation of the polymeric matrix by the harder reinforcement material.

 (ii) Delamination of the polymer or polymeric matrix, especially at high sliding distances where mica-like structures are observed on separate polymeric layers.

 (iii) Thermal degeneration of the contact interface, gradually deteriorating the mechanical strength of the sliding surface, thus leading to increased wear progression.

It can be stipulated that decent wear characteristics require the absence of imperfections and distortions, which are associated with the manufacturing temperature. In conclusion, an optimization of the wear resistance of FDM-fabricated parts can be achieved with a factor variation analysis of the process temperature while significant enhancements can be attained solely through proper material reinforcement.

## References

[1] J. P. Kruth, G. Levy, F. Klocke, and T. H. C. Childs, "Consolidation phenomena in laser and powder-bed based layered manufacturing," *CIRP Annals—Manufacturing Technology*, vol. 56, no. 2, pp. 730–759, 2007.

[2] A. Tsouknidas, S. Maropoulos, S. Savvakis, and N. Michailidis, "FEM assisted evaluation of PMMA and Ti6Al4V as materials for cranioplasty resulting mechanical behaviour and the neurocranial protection," *Bio-Medical Materials and Engineering*. In press.

[3] M. C. Galetz, T. Uth, M. A. Wimmer, P. Adam, and U. Glatzel, "Determination of the temperature rise within UHMWPE

tibial components during tribological loading," *Acta Biomaterialia*, vol. 6, no. 2, pp. 552–562, 2010.

[4] G. Bergmann, F. Graichen, A. Rohlmann, N. Verdonschot, and G. H. van Lenthe, "Frictional heating of total hip implants, part 1: measurements in patients," *Journal of Biomechanics*, vol. 34, no. 4, pp. 421–428, 2001.

[5] G. Bergmann, F. Graichen, A. Rohlmann, N. Verdonschot, and G. H. van Lenthe, "Frictional heating of total hip implants. Part 2: finite element study," *Journal of Biomechanics*, vol. 34, no. 4, pp. 429–435, 2001.

[6] S. He, S. Cho, and R. Singh, "Prediction of dynamic friction forces in spur gears using alternate sliding friction formulations," *Journal of Sound and Vibration*, vol. 309, no. 3–5, pp. 843–851, 2008.

[7] T. Cousseau, B. Graça, A. Campos, and J. Seabra, "Friction torque in grease lubricated thrust ball bearings," *Tribology International*, vol. 44, no. 5, pp. 523–531, 2011.

[8] X. Q. Yu, S. He, and R. L. Cai, "Frictional characteristics of mechanical seals with a laser-textured seal face," *Journal of Materials Processing Technology*, vol. 129, no. 1–3, pp. 463–466, 2002.

[9] C. M. Cheah, C. K. Chua, C. W. Lee, C. Feng, and K. Totong, "Rapid prototyping and tooling techniques: a review of applications for rapid investment casting," *International Journal of Advanced Manufacturing Technology*, vol. 25, no. 3-4, pp. 308–320, 2005.

[10] G. N. Levy, R. Schindel, and J. P. Kruth, "Rapid manufacturing and rapid tooling with layer manufacturing (LM) technologies, state of the art and future perspectives," *CIRP Annals—Manufacturing Technology*, vol. 52, no. 2, pp. 589–609, 2003.

[11] S. M. Peltola, F. P. W. Melchels, D. W. Grijpma, and M. Kellomäki, "A review of rapid prototyping techniques for tissue engineering purposes," *Annals of Medicine*, vol. 40, no. 4, pp. 268–280, 2008.

[12] J. Winder and R. Bibb, "Medical rapid prototyping technologies: state of the art and current limitations for application in oral and maxillofacial surgery," *Journal of Oral and Maxillofacial Surgery*, vol. 63, no. 7, pp. 1006–1015, 2005.

[13] E. Sachlos and J. T. Czernuszka, "Making tissue engineering scaffolds work. Review on the application ofsolid freeform fabrication technology to the production of tissue engineering scaffolds," *European Cells and Materials*, vol. 5, pp. 29–40, 2003.

[14] J. M. Williams, A. Adewunmi, R. M. Schek et al., "Bone tissue engineering using polycaprolactone scaffolds fabricated via selective laser sintering," *Biomaterials*, vol. 26, no. 23, pp. 4817–4827, 2005.

[15] S. Kumar and J. P. Kruth, "Wear performance of SLS/SLM materials," *Advanced Engineering Materials*, vol. 10, no. 8, pp. 1–4, 2008.

[16] A. Rosochowski and A. Matuszak, "Rapid tooling: the state of the art," *Journal of Materials Processing Technology*, vol. 106, no. 1–3, pp. 191–198, 2000.

[17] J. P. Li, J. R. de Wijn, C. A. van Blitterswijk, and K. de Groot, "The effect of scaffold architecture on properties of direct 3D fiber deposition of porous Ti6Al4V for orthopedic implants," *Journal of Biomedical Materials Research—Part A*, vol. 92, no. 1, pp. 33–42, 2010.

[18] A. Equbal, A. K. Sood, V. Toppo, R. K. Ohdar, and S. S. Mahapatra, "Prediction and analysis of sliding wear performance of fused deposition modelling-processed ABS plastic parts," *Proceedings of the Institution of Mechanical Engineers Part J*, vol. 224, no. 12, pp. 1261–1271, 2010.

[19] A. Tsouknidas, D. Kountouras, S. Maropoulos, N. Kiratzis, and N. Michalilidis, "Tribological, mechanical and physical characterization of hydroxyapatite/polycarpolactone biocomposites," *Journal of the Balkan Tribological Association*. In press.

[20] S. Kumar, J. P. Kurth, J. van Humbeeck, and A. Voet, "A study of degeneration of laser sintered moulds using wear tests," *Rapid Prototyping Journal*, vol. 15, no. 2, pp. 104–110, 2009.

[21] R. C. Bill, "Review of factors that influence fretting wear," in *Materials Evaluation Under Fretting Conditions, ASTM STP 780*, S. R. Brown, Ed., pp. 165–181, ASTM, Philadelphia, Pa, USA, 1982.

[22] R. B. Waterhouse, "Fretting fatigue," *International Journal of Fatigue*, vol. 37, no. 2, pp. 77–97, 1992.

[23] M. Niinomi, "Mechanical biocompatibilities of titanium alloys for biomedical applications," *Journal of the Mechanical Behavior of Biomedical Materials*, vol. 1, no. 1, pp. 30–42, 2008.

[24] P. Schaaff, "The role of fretting damage in total hip arthroplasty with modular design hip joints -evaluation of retrieval studies and experimental simulation methods," *Journal of Applied Biomaterials & Biomechanics*, vol. 2, no. 3, pp. 121–135, 2004.

[25] Y. Berthier, L. Vincent, and M. Godet, "Fretting fatigue and fretting wear," *Tribology International*, vol. 22, no. 4, pp. 235–242, 1989.

[26] S. Fouvry, P. Kapsa, and L. Vincent, "Fretting-wear and fretting-fatigue: relation through a mapping concept," in *Fretting Fatigue: Current Technology and Practices, ASTM STP 1367*, D. W. Hoeppner, V. Chandrasekaran, and C. B. Elliott, Eds., pp. 49–64, ASTM, West Conshohocken, Pa, USA, 2000.

[27] V. Chandrasekaran, W. L. Sauer, A. M. Taylor, and D. W. Hoeppner, "Evaluation of the fretting corrosion behavior of the proximal pad taper of a modular hip design," *Wear*, vol. 231, no. 1, pp. 54–64, 1999.

[28] M. Varenberg, G. Halperin, and I. Etsion, "Different aspects of the role of wear debris in fretting wear," *Wear*, vol. 252, no. 11-12, pp. 902–910, 2002.

[29] E. Rabinowicz, *Compatibility Criteria for Sliding Metals in Friction and Lubrication in Metal Processing*, ASME, New York, NY, USA, 1996.

[30] F. P. Bowden and D. Tabor, "The influence of surface finish on the friction and deformation of surfaces in properties of metallic surfaces," *Journal Institute of Metals*, pp. 197–212, 1953.

[31] ASTM G99-04: Standard Test Method for Wear Testing with a Pin-on-Disk Apparatus, ASTM International.

[32] T. C. Ovaert and H. S. Cheng, "Counterface topographical effects on the wear of polyetheretherketone and a polyetheretherketone-carbon fiber composite," *Wear*, vol. 150, no. 1-2, pp. 275–287, 1991.

[33] D. Dowson, S. Taheri, and N. C. Wallbridge, "The role of counterface imperfections in the wear of polyethylene," *Wear*, vol. 119, no. 3, pp. 277–293, 1987.

[34] P. H. Chong, H. C. Man, and T. M. Yue, "Microstructure and wear properties of laser surface-cladded Mo-WC MMC on AA6061 aluminum alloy," *Surface and Coatings Technology*, vol. 145, no. 1–3, pp. 51–59, 2001.

[35] K. Murali, A. N. Chatterjee, P. Saha et al., "Direct selective laser sintering of iron-graphite powder mixture," *Journal of Materials Processing Technology*, vol. 136, no. 1–3, pp. 179–185, 2003.

[36] C. S. Ramesh and C. K. Srinivas, "Friction and wear behavior of laser-sintered iron-silicon carbide composites," *Journal of*

*Materials Processing Technology*, vol. 209, no. 14, pp. 5429–5436, 2009.

[37] C. S. Ramesh, S. K. Seshadri, and K. J. L. Iyer, "A survey of aspects of wear of metals," *Indian Journal of Technology*, vol. 29, no. 4, pp. 179–185, 1991.

[38] N. Saka and D. P. Karalekas, "Friction and wear of particle reinforced metal ceramic composites," in *Proceedings of the Conference on Wear of Materials*, pp. 784–793, ASME, New York, NY, USA, 1985.

[39] A. Simchi, F. Petzoldt, and H. Pohl, "Direct metal laser sintering: material considerations and mechanisms of particle bonding," *International Journal of Powder Metallurgy*, vol. 37, no. 2, pp. 49–61, 2001.

[40] A. Simchi and H. Pohl, "Effects of laser sintering processing parameters on the microstructure and densification of iron powder," *Materials Science and Engineering A*, vol. 359, no. 1-2, pp. 119–128, 2003.

[41] B. H. Lee, J. Abdullah, and Z. A. Khan, "Optimization of rapid prototyping parameters for production of flexible ABS object," *Journal of Materials Processing Technology*, vol. 169, no. 1, pp. 54–61, 2005.

[42] A. K. Sood, R. K. Ohdar, and S. S. Mahapatra, "Parametric appraisal of fused deposition modelling process using the grey Taguchi method," *Proceedings of the Institution of Mechanical Engineers Part J*, vol. 224, no. B1, pp. 135–145, 2010.

[43] Q. Sun, G. M. Rizvi, C. T. Bellehumeur, and P. Gu, "Effect of processing conditions on the bonding quality of FDM polymer filaments," *Rapid Prototyping Journal*, vol. 14, no. 2, pp. 72–80, 2008.

[44] A. K. Sood, R. K. Ohdar, and S. S. Mahapatra, "Parametric appraisal of mechanical property of fused deposition modelling processed parts," *Materials and Design*, vol. 31, no. 1, pp. 287–295, 2010.

[45] K. Friedrich, Z. Zhang, and P. Klein, "Wear of polymer composites," *Wear Material Mechanisms and Practice*, pp. 269–287, 2005.

[46] G. Wróbel and M. Szymiczek, "Influence of temperature on friction coefficient of low density polyethylene," *Journal of Achievements in Materials and Manufacturing Engineering*, vol. 28, no. 1, pp. 31–34, 2008.

[47] D. Shakhvorostov, K. Pöhlmann, and M. Scherge, "An energetic approach to friction, wear and temperature," *Wear*, vol. 257, no. 1-2, pp. 124–130, 2004.

[48] T. Nakahara, S. Momozono, and A. O. Rui, "Effect of surface temperature rise on friction characteristics for sliding speed under unlubricated condition," *Proceedings of the Institution of Mechanical Engineers Part J*, vol. 224, no. 3, pp. 271–278, 2010.

*Research Article*

# Integrated Approach for a Knowledge-Based Process Layout for Simultaneous 5-Axis Milling of Advanced Materials

## F. Klocke, T. Bergs, M. Busch, L. Rohde, M. Witty, and G. F. Cabral

*High-Performance Cutting, Fraunhofer Institute for Production Technology (IPT), Steinbachstraße 17, 52074 Aachen, Germany*

Correspondence should be addressed to M. Busch, marc.busch@ipt.fraunhofer.de

Advanced materials, like nickel-based alloys, gain importance in turbomachinery manufacturing, where creating complex surfaces constitute a major challenge. However, milling strategies that provide high material removal rates at acceptable tooling costs demand optimized tool geometry and process parameter selection. In this paper, a description of circular milling is given, focusing on resulting engagement conditions. Regarding this, a test bench was designed to investigate the chip formation process in an analogy milling process. Furthermore, the methodology for the approach in the analogy process was developed. Results of a first test run in Inconel 718 verify the presented approach.

## 1. Introduction and Motivation

*1.1. Applications.* Increasing demands in the turbomachinery sector lead to further use of advanced materials with distinguished physical properties, resulting in high thermal and mechanical loads during machining [1–3]. A common task is the manufacture of complex geometrical features, that can be abstracted to notches or slots described by two or three boundaries, as they occur, for example, in the geometries of Blisks (blade integrated discs), single blades, and landing gears; see Figure 1.

Due to the complexity of such geometries and the limited machinability of the applied materials, milling in five axis simultaneously becomes essential. For instance, nickel-based alloys possess a low thermal conductivity, high rigidity, low elastic modulus, and high chemical reactivity at elevated temperatures. Furthermore, they are characterized by a lamellar chip formation process leading to dynamic fatigue stress at the tool and hence to an increased tool wear [4–8]. All these characteristics restrain the feasible range of cutting parameters. Furthermore, the high aspect ratios of the complex geometries require the usage of tools with long shafts and small diameters, which restrains the process velocities even more. For milling such components, several different strategies have been used in the past [9, 10]. However, to provide an economic process, the realization of high material

removal rates at acceptable tooling costs is necessary. Hence, the manufacturing process has to be designed in a way that geometrical, qualitative, and economical requirements can be fulfilled efficiently. Herefrom, the demand for an integrated approach for a knowledge-based process layout originates which links a comprehensive understanding of the chip formation process to the resulting loads at the tool.

*1.2. Roughing Strategies.* The major characteristics while machining advanced materials like nickel-based alloys are high temperatures within the cutting zone, high mechanical loads at the tool, and high dynamic loads resulting from the lamellar chip formation process [4–6, 11]. However, machining such alloys is possible even under efficient conditions but it requires innovative milling strategies based on an optimized knowledge-based process layout. For instance, the roughing process has to show high material removal rates. To realize this, usually a large portion of the tool is in contact with the material. An important variable for characterizing this contact is the (radial) tool engagement described by the engagement angle $\Phi_c$. Large tool engagement angles cause long contact times between the tool and the workpiece. Combined with the low thermal conductivity of the given material, this leads to high temperatures and short tool life. A milling process with large engagement angles is, for
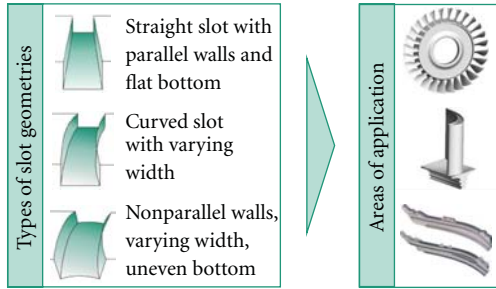
FIGURE 1: Areas of application.

example, the conventional slot milling. Here, engagement angles can reach up to 180°; see Figure 2(a). Besides the high engagement angle, this milling technique leaves only limited potential for process optimizations. So, the target for a high-performing milling strategy is a high material removal rate at moderate engagement angles. Processes with small(er) contact angles are, for example, flank milling operations. The engagement angle is directly affected by the radial cutting width $a_e$. Hence, flank milling assures more freedom to vary the technological cutting parameters in a wide range. The velocity may be increased up to four times compared to conventional slot milling, and cutting depths of twice the tool diameter become possible [11]. However, a pre-machined/opened slot is required for such process conditions. Circular milling (also: trochoidal milling) is a machining strategy that takes advantage of the beneficial aspects of flank milling even for closed slots. This strategy also provides the milling of complex geometries as presented in Figure 1 and has shown to be favourable for milling advanced materials [10, 12, 13]. The most simple case of trochoidal milling is described in Figure 2(b), a straight slot with a constant width and parallel walls. Machining such a slot can be conducted by defining a circle and shifting this circle by a concrete cutting width. Finally, a transition condition between the circles has to be defined to ensure a harmonic tool path. However, the portion of unproductive tool motion is relatively high which indicates a high optimization potential for the process layout.

*1.3. Objectives and Challenges for the Process Layout.* Altintas and Lazoglu already analyzed, described, and modelled trochoidal processes [10, 14]. Klocke et al. presented a model-based optimization of trochoidal roughing and focused on the beneficial aspect of applying large cutting depths [11]. However, a further crucial aspect in order to assure a knowledge-driven process layout is a detailed understanding of the chip formation process while machining, which has to be linked to the resulting loads at the tool. Solely, the feed rate $f_z$ and the cutting speed $v_c$ are insufficient for designing complex milling tasks, as presented in [15, 16]. Consequently, based on a description of circular milling, this paper is focussing on the resulting engagement conditions and links them to the occurring loads at the tool. Regarding this, an innovative test bench will be presented which allows a detailed investigation of the chip formation process in an

analogy milling process. Furthermore, the methodology for the approach in the analogy process will be presented.

## 2. Theoretical Process Analysis

*2.1. Circular Milling.* In circular milling operations, the diameter of the tool is smaller than the slot width and the tool follows a circular path from one slot flank to the other. Thereby, the geometry of the tool path is constrained to only two defined positions per path segment; see Figure 2(b). These points are preset by the desired slot geometry, whereas all other points of the tool path can be chosen freely by the process designer according to favourable cutting conditions. Varying the diameter of the circles allows to vary the slot width and by tilting the tool axis, nonparallel slot walls can be created; see Figure 1. In principle, the process consists of two major sections—a material removal process and a retral movement without any contact between tool and workpiece; see Figure 3(a). The local thickness of the chip to be removed (highlighted in Figure 3(b)) is changing essential during the circular movement of the tool. This results in heavy alternating thermal and mechanical loads at the tool [10].

*2.2. Macroscopic Contact Analysis.* The contact conditions on macroscopic scale focus on the tool's outer contour penetration of the workpiece described by the engagement angle. Thereby, workpiece and tool can be modeled with different approaches of computer-based geometric simulations. The system used here is based on the so-called dexel model, where the workpiece is represented as a set of closely aligned nails or dexels; the tool is represented by a cylinder [17, 18]. The engagement angle analysis of a circular tool path shows a distribution as displayed in Figure 4 for various cutting widths.

As the maximum of removed material correlates with the maximum tool engagement, demand for further path optimization to keep the engagement angle constant on high levels becomes obvious; see Figure 5(a). Referring to this, another analysis exhibits that variations of the tool path geometry are leading to different maximum effective tool engagements; see Figure 5(b). This can remarkably reduce the processing time of trochoidal milling [11].

This shows on the one hand that the macroscopic contact conditions for linear flank milling are not valid for circular tool paths and on the other hand the importance of optimizing the engagement conditions.

*2.3. Microscopic Contact Analysis.* The contact conditions on microscopic scale are obtained by using the actual tool geometry and considering the translational and rotatory tool movement. The contact condition describes the contact between the chip face and the uncut chip. It can be explained by mainly two parameters, the local thickness of the chip to be removed $h_{sp}$ and the related cross-section of the chip $A_{sp}$. The cross-section represents the amount of material in front of the cutting edge; see highlighted area in Figure 3(b).
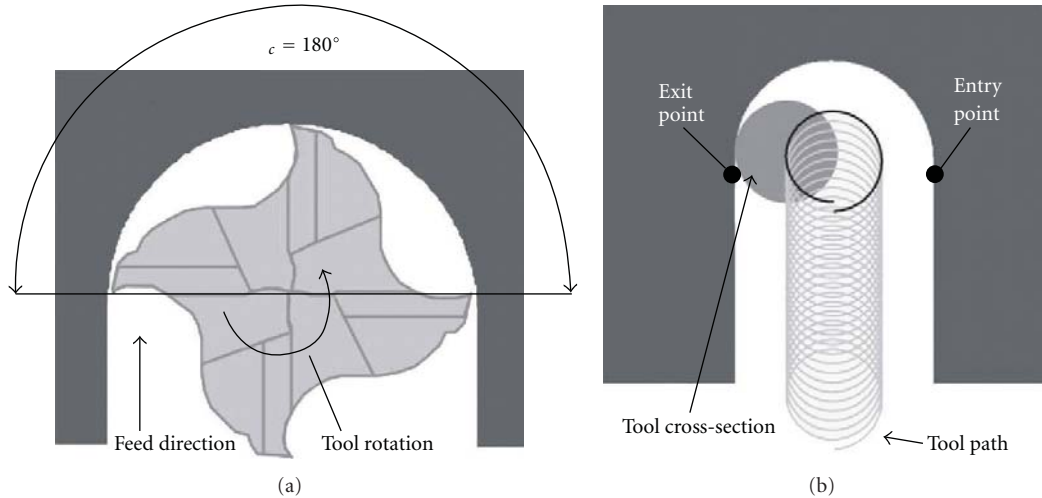
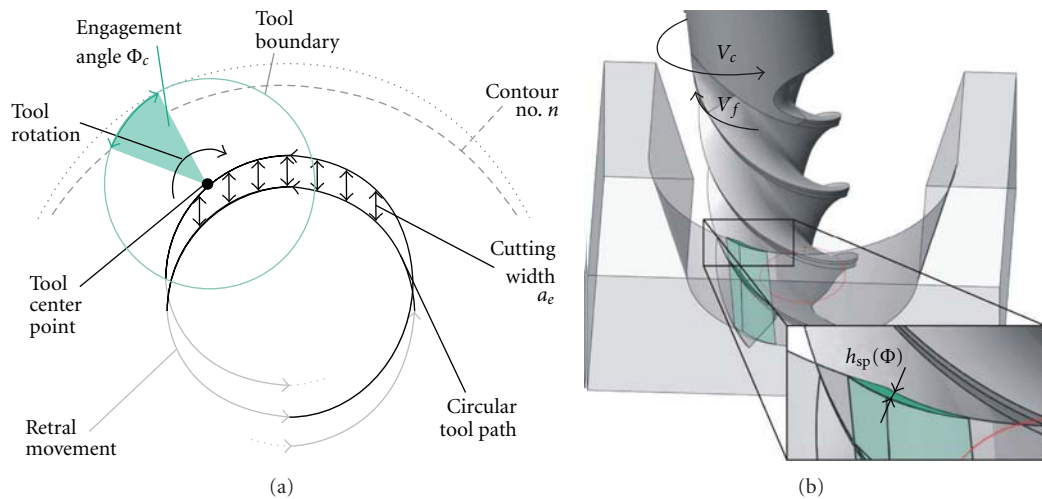FIGURE 2: (a) Conventional slot milling; (b) Circular milling.



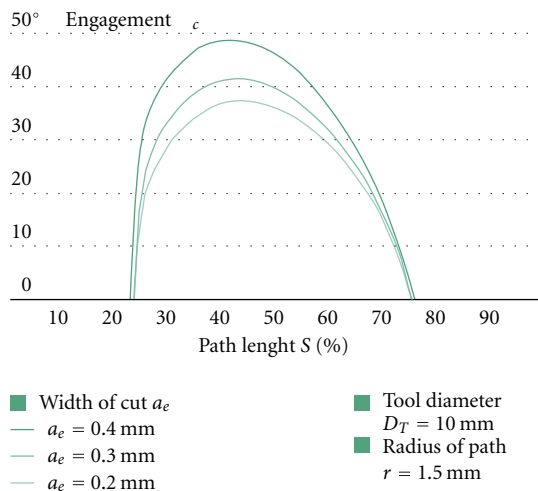FIGURE 3: Macroscopic (a) and microscopic (b) contact conditions of circular milling.



FIGURE 4: Influence of the cutting width $a_e$.

Exemplary, Figure 6(a) shows the influence of the tool path radius on the uncut chip thickness. With regards to the maximum values of $h_{sp}$, the influence is negligible. In contrast to the macroscopic contact conditions, it is thus legitimate to apply the known formulas for calculation of the microscopic contact conditions for linear tool paths to circular and trochoidal tool path as well. The influence of the feed per tooth $f_z$ and the cutting width $a_e$ on the uncut chip thickness is significantly higher, as it is exemplary shown in Figure 6(b). Similar tendencies can be found for the dependencies of the chip cross-section [11, 19]. This shows the high potential of optimizing the technological cutting conditions along the whole tool path. The optimization is mainly triggered by two aspects, the identification of a compromise between the engagement angle $\Phi_c$, the cutting velocity $v_c$, and the maximum uncut chip thickness $h_{sp, max}$ and the investigation of an optimized tool geometry. Therefore, a novel test bench is applied.
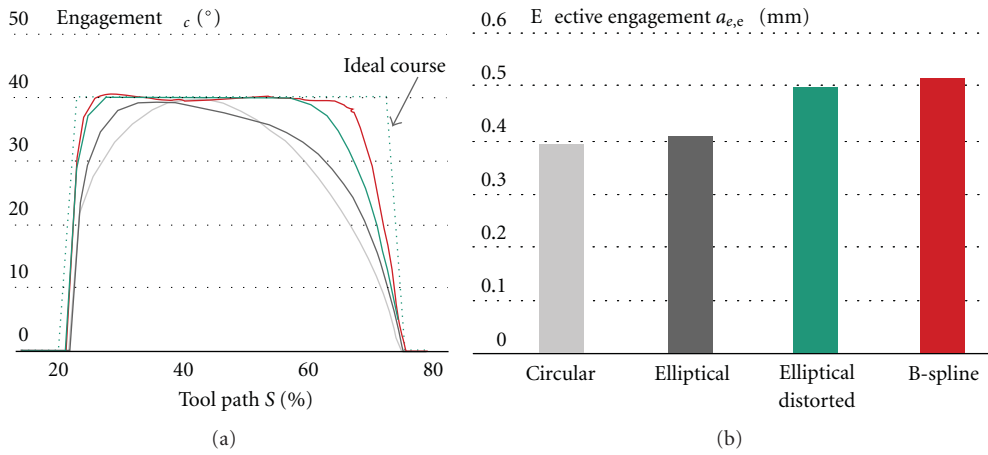
FIGURE 5: Optimized tool path geometries (a) and their influence on the effective tool engagements (b).
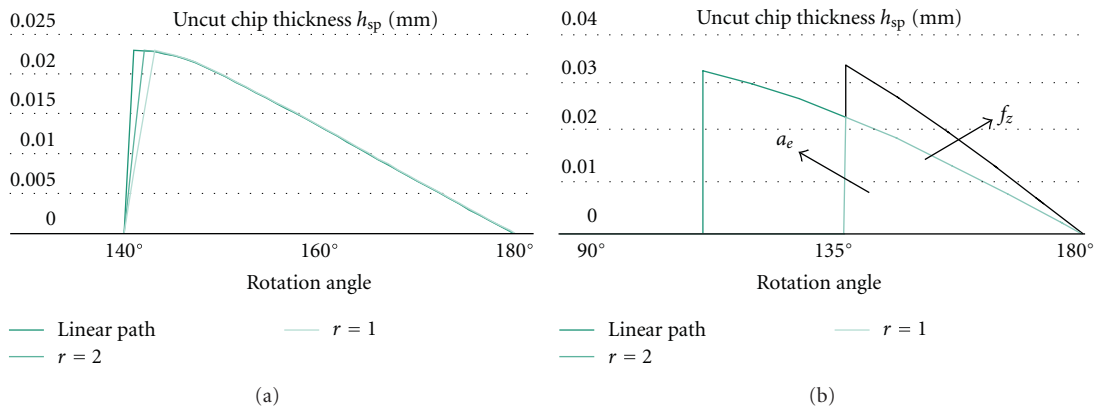


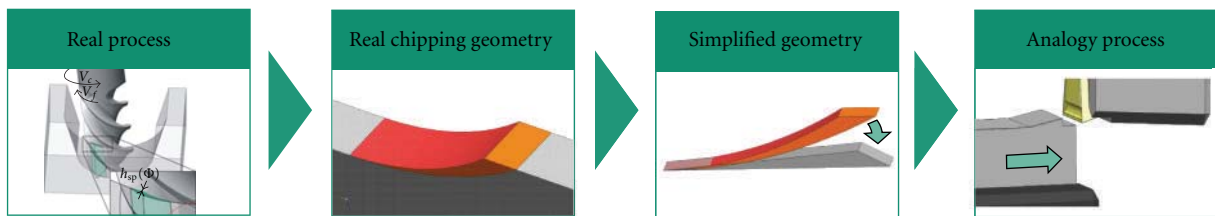FIGURE 6: Sensitivity of the uncut chip thickness.



FIGURE 7: Transformation from the real to the analogy milling process.
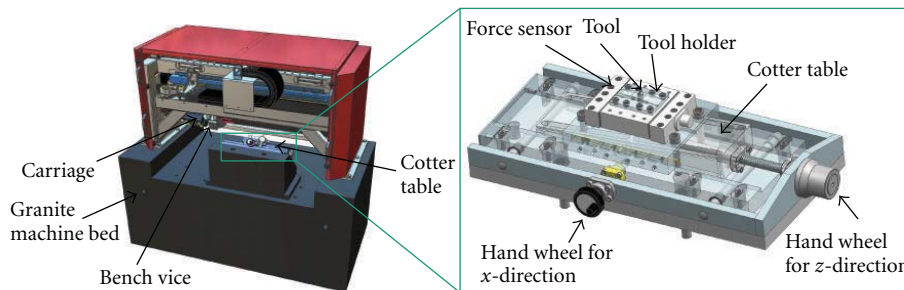


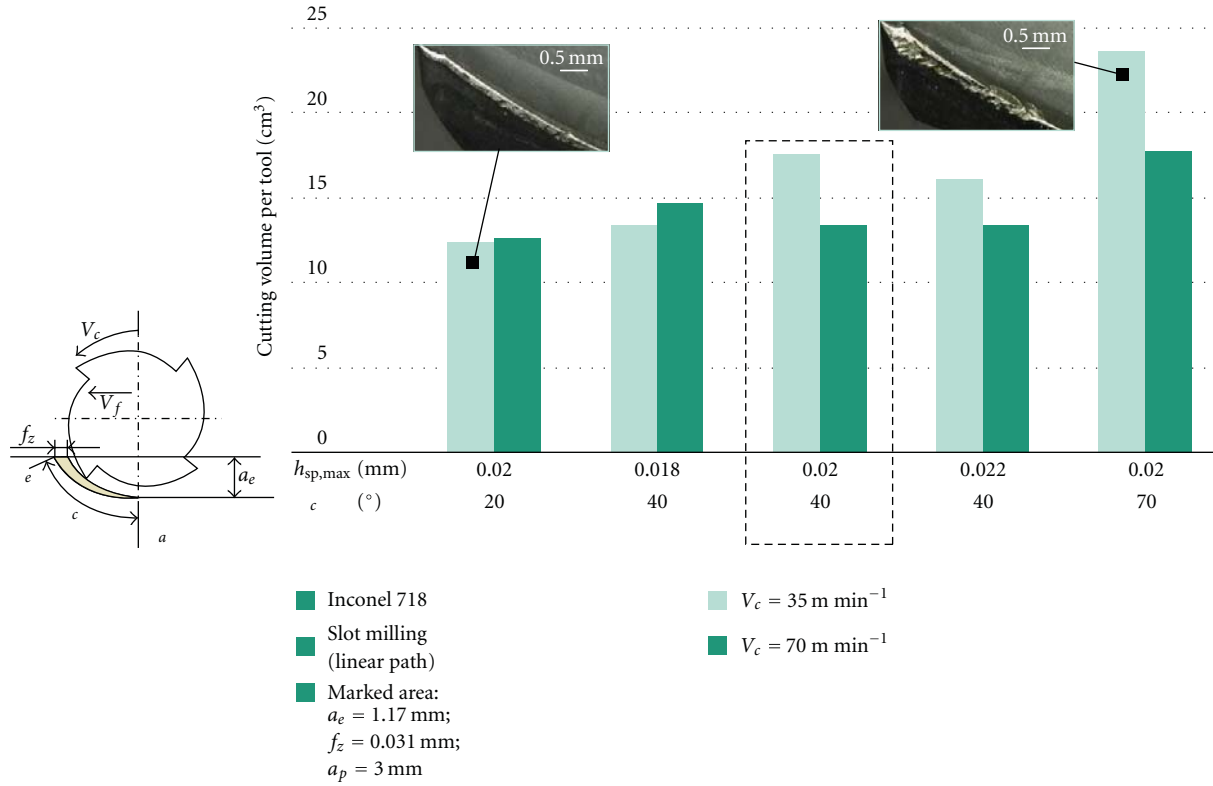FIGURE 8: Setup of the novel analogy test bench for milling processes.

FIGURE 9: Influence of the tool engagement and the cutting velocity on the tools' cutting volume.
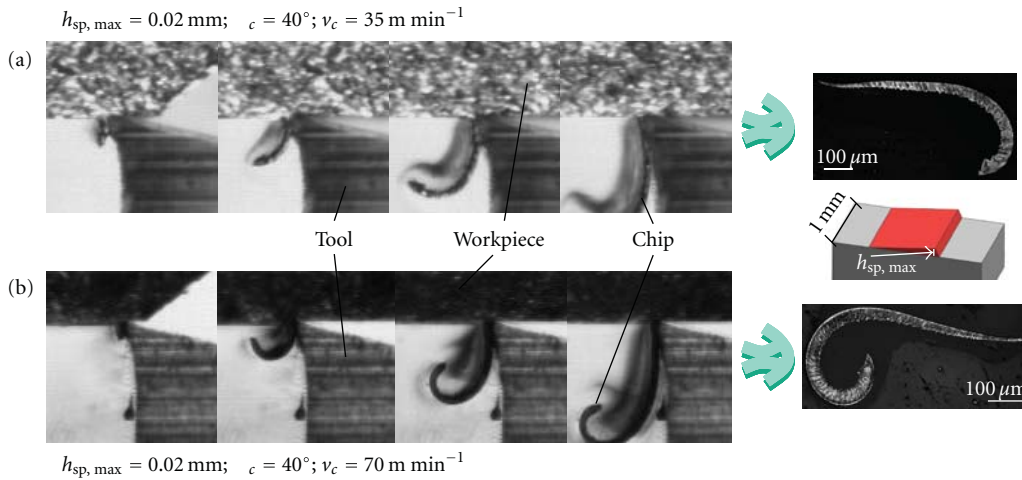


FIGURE 10: Investigation of chip curve and serration; (a) low and (b) high chip curve and serration.

## 3. Process Layout Optimization

### 3.1. Description of Novel Test Bench.

The novel test bench combines following two beneficial advantages that classifies it from other orthogonal cutting devices—a good accessibility and realization of a variable chipping geometry. The test-bench-related methodology is based on a transformation of the uncut chip geometry from the rotatory real process to a translative analogy process; see Figure 7. The evaluated uncut chip geometry can be displayed and manufactured in form of specimens.

To realize the translative movement of the analogy process, a hydrostatic mounted carriage conducts an one-dimensional movement. The carriage guides the manufactured specimen, which is clamped in a high-precision bench vice, against the stationary tool where the chip formation process occurs; see Figure 8. The test bench includes measurement devices for forces as well as capacitive sensors.

TABLE 1: Summary of cutting parameters.

| | |
|---|---|
| Cutting velocity (m min$^{-1}$) | 35–70 |
| Max. uncut chip thickness (mm) | 0,018–0,02–0,022 |
| Engagement angle (°) | 20–40–70 |
| Material | Inconel 718 |
| Process | Real analogy |

The force measurement is provided by a three-component dynamometer Kistler9129AA and occurs tool sided. Furthermore, the good accessibility allows the implementation of a high-velocity camera as well as a thermography camera.

*3.2. Experimental Setup.* Based on real milling processes, which were conducted in form of slot cutting operations on the machine tool Heller MC25, analogy milling operations via the novel test bench were performed. To investigate the influence of the tool engagement angle on the cutting performance, this parameter was varied according to Table 1. Moreover, the maximum uncut chip thickness $h_{\text{sp, max}}$ was varied by keeping the engagement angle constant. The last parameter to be varied was the cutting velocity, between 35 m min$^{-1}$ and 70 m min$^{-1}$. All processes were performed in the nickel-based alloy Inconel 718 at forged state, indicating no significance in regard to the orientation of the grain structure. The applied carbide milling tools from Seco Jabro Tools were coated with a TiAlN layer and provided a diameter of 10 mm, a cutting edge radius of 12 $\mu$m and four teeth. To investigate and compare the real and analogy milling process sufficiently, multiple data was acquired, such as force and metallographic chip analysis as well as pictures using a high-velocity camera.

*3.3. Results.* To investigate the overall process performance of the applied milling tools within the shown parameter field, slot cutting operations were performed. The experimentations exhibit that the tool engagement angle $\Phi_c$ and the cutting velocity $v_c$ influence the achieved cutting volume significantly. Over the complete parameter set, a rapid wear progression could be found which, for higher cutting velocities and tool engagements, resulted in cutting edge chipping; see Figure 9. In this connection, it has to be pointed out that a land wear of 0,2 mm or cutting edge chipping constituted the abort criterion of the tests. Moreover, the chip serration significantly increased with the cutting velocity, whereas an enlargement of the engagement angle led to a degradation of the surface quality as well as to a burr formation at the machined workpieces resulting in a stronger abrasive tool wear. In order to relate these findings to proper actions for a systematic and efficient optimization of the milling process, fundamental and detailed knowledge regarding the chip formation process displays an indispensible must.

For this aim, analogy milling tests using the novel test bench were performed for the benefit of a fast, effective, and reproducible investigation of potential parameters for process optimization. The measured forces in the analogy tests conformed to the forces detected in the real milling tests. Thus, an assessment of the occurring forces during machining becomes possible by using the novel test bench. Similar to the slot milling tests, the analogy tests showed that the cutting force $F_c$ increased with the cutting velocity and the tool engagement, while the passive force $F_p$ decreased with the cutting velocity. This could be seen as an evidence for a decrease of deformation labour to be expended for the cutting process at elevated cutting velocities leading to a lower tool displacement and hence to consistent surface properties. This characteristic is confirmed by the analysis of the chip compression $\lambda_{\text{sp}}$ which is defined as the relation of the covered cutting distance and the length of the chip. Here, a decrease of chip compression could be revealed for a raise of cutting velocity. Furthermore, the analysis of the chip serration, mainly depending on the grain structure of the machined workpiece material [8], showed a progression with the cutting velocity leading to higher fatigue stresses at the tools and hence to shorter tool life. In the frame of the analysis, it also was detected and visualized that higher chip curves lead to shorter contact length between the forming chip and the tool. This obviously results in higher surface pressures on the tools' rake face induced by the chip and hence to further wear progression. As it can be seen in Figure 10 for $h_{\text{sp, max}} = 0,02$ mm and $\Phi_c = 40°$, the chip curve varies with the cutting speed, (a) $v_c = 35$ m min$^{-1}$ and (b) $v_c = 70$ m min$^{-1}$, which can be visualized and analyzed via high-velocity camera and light microscope pictures.

The multiple data gained by using the novel analogy milling test bench illustrates the chip formation process in detail and therefore gives unprecedented hints for further optimizing the process parameter frame as well as the tool design for ambitious milling tasks.

## 4. Conclusions

In this paper, an integrated approach for a knowledge-based process layout for simultaneous 5-axis milling of advanced materials was introduced. Besides the optimization of the tool path itself, the high potential of optimizing the cutting parameters as well as the tool geometry was presented. Referring to this, an innovative test bench for a detailed analysis of the chip formation process was established.

## Acknowledgments

## References

[1] R. Schafrik and R. Sprague, "Superalloy technology—a perspective on critical innovations for turbine engines," *Key Engineering Materials*, vol. 380, pp. 113–134, 2008.

[2] M. Balazinski, V. Songmene, and L. Kops, "Improvement of tool life through variable feed milling of inconel 600," *CIRP Annals*, vol. 44, no. 1, pp. 55–58, 1995.

 [3] K. Weinert, D. Biermann, and S. Bergmann, "Machining of high strength light weight alloys for engine applications," *CIRP Annals*, vol. 56, no. 1, pp. 105–108, 2007.

 [4] N. Narutaki, Y. Yamane, K. Hayashi, T. Kitagawa, and K. Uehara, "High-speed Machining of Inconel 718 with Ceramic Tools," *CIRP Annals*, vol. 42, no. 1, pp. 103–106, 1993.

 [5] M. Alauddin, M. A. El Baradie, and M. S. J. Hashmi, "End-milling machinability of inconel 718," *Journal of Engineering Manufacture*, vol. 210, no. 1, pp. 11–23, 1996.

 [6] E. O. Ezugwu, Z. M. Wang, and A. R. Machado, "The machinability of nickel-based alloys: a review," *Journal of Materials Processing Technology*, vol. 86, no. 1–3, pp. 1–16, 1998.

 [7] G. Byrne, D. Dornfeld, and B. Denkena, "Advancing cutting technology," *CIRP Annals—Manufacturing Technology*, vol. 52, no. 2, pp. 483–507, 2003.

 [8] L. Markworth, *Fünfachsige schlichtfräsbearbeitung von strömungsflächen aus nickelbasislegierungen*, Doctoral thesis, Aachen, Germany, 2005.

 [9] G. Lebküchner, "Innovative frässtrategien für die bliskbearbeitung," in *Proceedings of the Neue Technologien für die Luft- und Raumfahrt*, Hannover, Germany, 2004.

[10] M. Otkur and I. Lazoglu, "Trochoidal milling," *International Journal of Machine Tools & Manufacture*, vol. 47, no. 9, pp. 1324–1332, 2007.

[11] F. Klocke, T. Bergs, M. Meinecke et al., "Model based optimization of trochoidal roughing of titanium," in *Proceedings of the 12th CIRP Conference on Modeling of Machining Operations*, Gaithersburg, Md, USA, 2008.

[12] S. Altmüller, *Simultanes Fünfachsiges Fräsen von Freiformflächen aus Titan*, Berichte aus der Produktionstechnik, 2001.

[13] F. Klocke and W. König, *Fertigungsverfahren Drehen, Fräsen, Bohren*, Springer, New York, NY, USA, 2008.

[14] N. Kardes and Y. Altintas, "Prediction of cutting forces in circular milling," in *Proceedings of the 3rd International Conference and Exhibition on Design and Production of Dies and Molds*, pp. 1–5, Bursa, Turkey, 2004.

[15] M. Meinecke, *Prozessauslegung zum fünfachsigen zirkularen schruppfräsen von titanlegierungen*, Doctoral thesis, Aachen, Germany, 2009.

[16] J. Köhler, *Berechnung der zerspankräfte bei variierenden spanungsquerschnittsformen*, Doctoral thesis, Hannover, Germany, 2010.

[17] K. C. Hui, "Solid sweeping in image space-application in NC simulation," *The Visual Computer*, vol. 10, no. 6, pp. 306–316, 1994.

[18] M. Stautner, *Simulation und optimierung der mehrachsigen fräsbearbeitung*, Doctoral thesis, Essen, Germany, 2005.

[19] E. Kose, A. Kurt, and U. Seker, "The effects of the feed rate on the cutting tool stresses in machining of Inconel 718," *Journal of Materials Processing Technology*, vol. 196, no. 1–3, pp. 165–173, 2008.